UNIVERSIDADE DE SÃO PAULO
ESCOLA POLITÉCNICA
PROGRAMA DE PÓS-GRADUAÇÃO EM ENGENHARIA QUÍMICA

BEATRIZ MARIA BAFFA LIMA

Carbon Dioxide Conversion to Carbon Monoxide by Reverse Water Gas Shift Chemical Looping

SÃO PAULO
2023

BEATRIZ MARIA BAFFA LIMA

Carbon Dioxide Conversion to Carbon Monoxide by Reverse Water Gas Shift Chemical Looping

Revised Version

Master Dissertation submitted to the Graduate Program in Chemical Engineering at the Escola Politécnica da Universidade de São Paulo, to obtain the degree of Master of Science

Concentration Area: Chemical Engineering

Advisor: Profª. Drª. Rita Maria de Brito Alves
Co-Advisor: Dr. Newton Libanio Ferreira

SÃO PAULO
2023

Este exemplar foi revisado e corrigido em relação à versão original, sob responsabilidade única do autor e com a anuência de seu orientador.

São Paulo, 08 de fevereiro de 2024

Assinatura do autor: Beatriz Maria Baffa Lima

Assinatura do orientador: Rita Maria de Brito Alves

Catalogação-na-publicação

Lima, Beatriz Maria Baffa
Carbon Dioxide Conversion to Carbon Monoxide by Reverse Water Gas Shift Chemical Looping / B. M. B. Lima -- versão corr. -- São Paulo, 2023.
99 p.

Dissertação (Mestrado) - Escola Politécnica da Universidade de São Paulo. Departamento de Engenharia Química.

1.Dióxido de Carbono 2.Processo (Modelagem) 3.Processo (Simulação) 4.Looping Químico I.Universidade de São Paulo. Escola Politécnica. Departamento de Engenharia Química II.t.

LIMA, B. M. B. **Carbon Dioxide Conversion to Carbon Monoxide by Reverse Water Gas Shift Chemical Looping**. 2023. Dissertation (Master of Science – Escola Politécnica, Universidade de São Paulo, São Paulo, 2023).

Approved on:	December 19th, 2023.
	Examining Commission
Profa. Dra.	Rita Maria de Brito Alves
Institution:	PQI-EPUSP
Evalution:	Approved
Profa. Dra.	Cristiane de Souza Siqueira Pereira
Institution:	Universidade de Vassouras
Evalution:	Approved
Prof. Dr.	Alexandre Mendonça Teixeira
Institution:	REPSOL SINOPEC BRASIL
Evalution:	Approved

ACKNOWLEDGEMENTS

I would like to express my sincere gratitude, starting with my incredible and beloved husband, Wesley. He has not only been by my side as a pillar of support throughout my journey over these years, but he has also played the role of an exceptional doctor, taking care of my health during the most challenging moments. Maintaining good health was essential for me to reach this point.

I want to extend my gratitude to all my friends and colleagues in the laboratory, who shared unity, assistance, friendship, and camaraderie. Over these years, we have built a happy family and a strong support network. I am fortunate to have encountered such remarkable individuals during my master's journey.

A special thank you is directed to my psychologists (Eliane and Jéssica) and my coach (Lara). These three extraordinary women played a crucial role in tending to my mental health and also acted as vital support for my development.

I express my gratitude to all the teachers who have crossed my path, as they are part of my history, shaping who I am and contributing to my professional growth. Without their guidance, I would not have acquired the knowledge that has brought me to this point.

I thank all those who truly love me and root for my success, whether they are long-time friends or family members. Love remains my constant strength.

I cannot fail to acknowledge my co-adviser, Dr. Newton, for his valuable teachings over these years. His contribution was fundamental in shaping the engineer I have become.

I also express my gratitude to God or the greater force of the universe that helped me overcome challenges and allowed me to be the first in my family to enter a university and defend a master's thesis. I feel blessed to have gained knowledge and to have completed my master's at a renowned institution like the University of São Paulo.

A special thank you goes to my advisor, Professor Dra. Rita, for placing her trust in me, welcoming me into her research group, and sharing invaluable teachings.

Last but not least, I extend gratitude to myself. Often, we forget to be grateful for our own accomplishments. I am deeply thankful for my resilience, determination, and willpower. While many individuals were instrumental in my journey, as mentioned earlier, all the support and love wouldn't have been sufficient if I hadn't had the determination to pursue my goals. I am content with my choices and believe that I have honored all the support and love I've received.

We may have countless reasons to abandon our dreams, but the final decision always rests with us. I have chosen to live my dreams every day.

“What matters is not what happens, but how you react.”

Epictetus

RESUMO

LIMA, B. M. B. **Carbon Dioxide Conversion to Carbon Monoxide by Reverse Water Gas Shift Chemical Looping**. 2023. Dissertation (Master of Science – Escola Politécnica, Universidade de São Paulo, São Paulo, 2023).

A captura, utilização e armazenamento de carbono (CCUS, do inglês *Carbon, Capture, Utilization and Storage*) é uma das principais estratégias para reduzir as emissões de dióxido de carbono na atmosfera. Recentemente, a utilização de dióxido de carbono (CO_2) tem atraído a atenção de pesquisadores e empresas, uma vez que pode contribuir para melhorar a economia do processo de captura de CO_2 através da produção de combustíveis e produtos químicos de alto valor agregado e tem sido considerada uma alternativa viável ao armazenamento geológico de CO_2. Dentre as tecnologias para utilização de CO_2, destaca-se a reação reversa de deslocamento gás-água (RWGS, do inglês *reverse water gas shift*) como uma rota promissora. A RWGS é uma reação que produz monóxido de carbono a partir de CO_2 e hidrogênio. O monóxido de carbono é um constituinte do gás de síntese. O principal desafio dessa reação é a busca por catalisadores que permitam que a reação ocorra em baixas temperaturas e atinja altas conversões. Além disso, no processo, ocorrem reações paralelas que geram produtos indesejados, como o metano (CH_4). Uma rota alternativa é o processo RWGS intensificado com recirculação química (*chemical looping*), RWGS-CL, utilizando óxidos metálicos como transportadores de oxigênio. O processo RWGS-CL é um processo cíclico de duas etapas para ativação do CO_2, onde ocorrem duas reações: oxidação e redução. Nesse contexto, este trabalho avaliou os potenciais óxidos metálicos para a aplicação da RWGS-CL, tendo a magnetita sido escolhida como o óxido carregador de oxigênio mais eficaz entre os avaliados. Foram conduzidas modelagem e simulação do processo, considerando um reator de leito fixo multitubular. Durante a análise, foram observadas conversões de reagentes em produtos atingindo 100% para o monóxido de carbono (CO) ao longo de 11 horas de reação contínua. Além disso, foram analisados o perfil de temperatura e a perda de carga ao longo do comprimento do reator, visando avaliar o potencial uso dessa tecnologia em escala industrial. Os resultados indicam que não há variações significativas de temperatura no reator quando aquecido a 1073K e que a perda de carga ao longo do comprimento do reator é desprezível.

Palavras-chave: reação reversa de deslocamento gás-água; loop químico; dióxido de carbono; gás de síntese; modelagem de processos, simulação de processos.

ABSTRACT

LIMA, B. M. B. **Carbon Dioxide Conversion to Carbon Monoxide by Reverse Water Gas Shift Chemical Looping**. 2023. Dissertation (Master of Science – Escola Politécnica, Universidade de São Paulo, São Paulo, 2023).

Carbon capture, utilization, and storage (CCUS) is one of the main strategies to reduce carbon dioxide emissions into the atmosphere. Recently, the use of carbon dioxide (CO_2) has attracted the attention of researchers and companies since it can contribute to improve the economy of the CO_2 capture process through the production of high value-added fuels and chemicals and has been considered a viable alternative to the geological storage of CO_2. Among the technologies for using CO_2, the reverse water gas shift reaction (RWGS) stands out as a promising route. RWGS is a reaction that produces carbon monoxide from CO_2 and hydrogen. Carbon monoxide is a constituent of the synthesis gas. The main challenge of this reaction is the search for catalysts that allow the reaction to occur at low temperatures and achieve high conversions. In addition, in the process, parallel reactions occur that generate unwanted products, such as methane (CH_4). An alternative route is the intensified RWGS process with chemical looping, RWGS-CL, using metal oxides as oxygen carriers. The RWGS-CL process is a two-step cyclic process for CO_2 activation, where two reactions occur: oxidation and reduction. In this context, this study aims to assess potential metal oxides for RWGS-CL and to perform the modeling and simulation of the process, considering a multitubular fixed-bed. During the analysis, conversions of reactants into products reaching 100% for carbon monoxide (CO) were observed over 11 hours of continuous reaction. Additionally, the temperature profile and pressure drop along the reactor length were analyzed to assess the potential use of this technology on an industrial scale. The results indicate that there are no significant temperature variations in the reactor when heated to 1073K, and the pressure drop along the reactor length is negligible.

KEYWORDS: reverse water-gas shift; chemical looping; carbon dioxide; synthesis gas; process modeling, process simulation.

LIST OF FIGURES

LIST OF TABLES

LIST OF ABBREVIATIONS AND ACRONYMS

APEA	Aspen Process Economic Analyzer
CCU	Carbon Capture and Utilization
CCUS	Carbon Capture, Utilization and Storage
CDCL	Coal Direct Chemical Looping
CISR	Combustor Integrated Steam Reforming
CLC	Chemical Looping Combustion
CLC-SECLR$_{HC}$	Chemical Looping Combustion and Sorption-Enhanced Reforming
CLG	Chemical Looping Gasification
CLP	Chemical-Looping Process
CLR	Chemical-Looping Reform Processes
COM	Cost of Manufacturing
E-RWGS	Reverse Water-Gas Shift Conducted by An Electric Field
FCI	Fixed Capital Investment
FT	Fischer-Tropsch
GWP	Global Warming Potential
IGCC	Integrated Gasification Combined Cycle
LBF	Support of $La_{0.5}Ba_{0.5}FeO_3$
LSF	Support of $La_{0.75}Sr_{0.25}FeO_3$
MSR	Methanol Steam Reforming
NPV	Net Present Value
OCM	Oxygen Carrier Materials
OTM	Oxygen Transfer Material
ROI	Return on Investment
RWGS	Reverse Water-Gas Shift
RWGS-CL	Reverse Water-Gas Shift Chemical Looping
SE-CLR$_{HC}$	Sorption-Enhanced Reforming in Two Separate Streams
SE-CLSR	Sorption-Enhanced Chemical Looping Steam Reforming
SG	Syngas
TPR	Temperature-programmed Reduction
TPO	Temperature-programmed Oxidation
XRD	X-ray Diffraction
XRF	X-ray Fluorescence

LIST OF SYMBOLS

Roman Symbols

A	Flow area
C_p	Heat capacity
c_t	Molar concentration in the gas phase
$C_{BM,i}$	The base module cost for equipment i
$C^0_{BM,i}$	The base price of equipment i
C_{OL}	The cost of operating labor
C_{UT}	The cost of utilities
C_{WT}	The cost of waste treatment
C_{RM}	The cost of raw materials
D_P	Particle diameter
E_A	Activation energy
$\dot{F}$	Mass flow rate
F_{in}	Molar inflow
F_{out}	Molar outflow
G	Gas flow rate
$\dot{h}$	Specific enthalpy
H_i	Enthalpy flows entering and leaving the system
j	Diffusive flux
$\not{k}^0$	Arrhenius pre-exponential factor
L	Length of the bed
M	Molar mass
m	Order of the gas phase reaction
m_s	Mass
N	Total number of components in the system
n_i	Number of moles of component i
n	Order of the solid phase reaction
$\dot{n}$	Mole flow rate
n	Number of moles
P	Operating pressure
P_0	Standard pressure

$\dot{Q}$	Heat
Re	Reynolds number
$r_{j,eff.}$	Corresponding effective reaction rate
$r_{j,eff.}^{M}$	Reaction rate in terms of moles
r_j^M	Reaction rate
R	Universal gas constant
SG	The synthesis gas produced (kg)
t	Time
T	Temperature
U	The total energy of the system
V_t	Volume of the part
v	Velocity
v_0	Surface velocity of the fluid
$\dot{W}_e$	Work
X_i	Molar conversion of species i
x	Mole fraction
z	Axial spatial coordinate

Greek Symbols

$\Delta\dot{E}_c$	Kinetic energy change
$\Delta\dot{E}_p$	Potential energy change
$\Delta {G_{fi}}^0$	Standard Gibbs energy of formation of species i
$\Delta\dot{H}$	Enthalpy change
ΔP	Pressure drop in the bed
ε	Fixed bed void fraction
η_{eff}	Effectiveness factor of the reaction rate
μ	Chemical potential
$\nu_{\alpha,j}$	Stoichiometric coefficient
ρ	Density
σ^M	Specific source term
ξ	Reaction extent
φ_i	Fugacity coefficient (calculated using the equation of state chosen for the system

Superscripts

(g)	Gas component
(s)	Solid component

Subscripts

α	Gas component index
β	Solid component index
eff	Effectiveness
in	Inlet conditions
out	Outlet conditions
Ox	Oxidation reaction
Red	Reduction reaction

SUMMARY

1 INTRODUCTION

The use of renewable energy sources to meet the world's energy demand has been a viable alternative to replace fossil fuels, contributing to the environmental development, thus reducing the rates of carbon dioxide (CO_2) emissions into the environment. Carbon dioxide is a gas that, under normal conditions, has no smell or taste, and is one of the main compounds in the photosynthesis process. However, its high concentration in the atmosphere causes several harmful environmental impacts, which contribute to the increase in the earth temperature, causing environmental degradation of ecosystems and landscapes (MEIRELLES, 2003).

Among the ways of reducing carbon dioxide in the atmosphere are the use of renewable fuel sources, and carbon, capture, utilization and storage (CCUS) strategy can contribute to achieve the carbon balance present in the atmosphere and neutralize its emission (SILVA, 2015).

An important technological route for using CO_2 as a carbon source for the generation of high valuable chemicals is the reverse water-gas shift (RWGS), which consists in a reaction that uses carbon dioxide and hydrogen to produce carbon monoxide (CO), a constituent of the synthesis gas (syngas). The RWGS reaction is given in equation 1:

$$H_2 + CO_2 \leftrightarrow H_2O + CO \qquad \Delta H_{R\,(298K)} = 41.3 \text{ kJ/mol} \qquad (1)$$

Due to the chemical stability of CO_2, which is a relatively non-reactive molecule, its conversion is highly energy demanding. Since RWGS is an endothermic reaction, it is thermodynamically favored at high temperatures (PASTOR-PÉREZ et al., 2017). Moreover, side reactions take place, which generate unwanted products, such as methane (CH_4), according to equation 2.

$$CO_2 + 4H_2 \leftrightarrow CH_4 + 2H_2O \qquad \Delta H_{R\,(298K)} = -165.0 \text{ kJ/mol} \qquad (2)$$

Thus, the main challenge of the RWGS process is the search for catalysts that allow the reaction to occur at low temperatures and achieve high conversions (SILVA, 2015). Special catalysts based on Ruthenium (Ru), Iron (Fe) and Nickel (Ni) are used to allow operation at lower temperatures (between 298–1073 K) and reduced CH_4 generation. Alternatively, the chemical looping technology has attracted attention as a promising approach to improve the

RWGS performance. The RWGS chemical looping (RWGS-CL) consists of dividing the reaction into reduction and oxidation steps, by using a metal oxide as an oxygen storage material. This process converts CO_2 to CO using a metal oxidation and reduction cycle as shown in equations 3 and 4:

Oxidation: $Me + CO_2 \leftrightarrow MeO + CO$ (3)

Reduction: $MeO + H_2 \leftrightarrow Me + H_2O$ (4)

In these equations, Me represents the metal used in the process. The chemical looping cycle enables the regeneration of the metal oxide, allowing for the repeated reduction and oxidation process for the continuous conversion of CO_2 to CO. This method can contribute to higher efficiency and selectivity in the production of CO from CO_2.

The transport of chemical species is carried out by two mechanisms: diffusion and/or convection. The mass convection mechanism is the one present in the studied process, and it is characterized by the transfer of species from a liquid or solid surface to a fluid that flows over this surface and the concentration gradient between the flowing fluid and the surface.

The comparison of general process schemes for the production of synthesis gas by the conventional RWGS reaction and by the RWGS-CL is presented in figure 1:

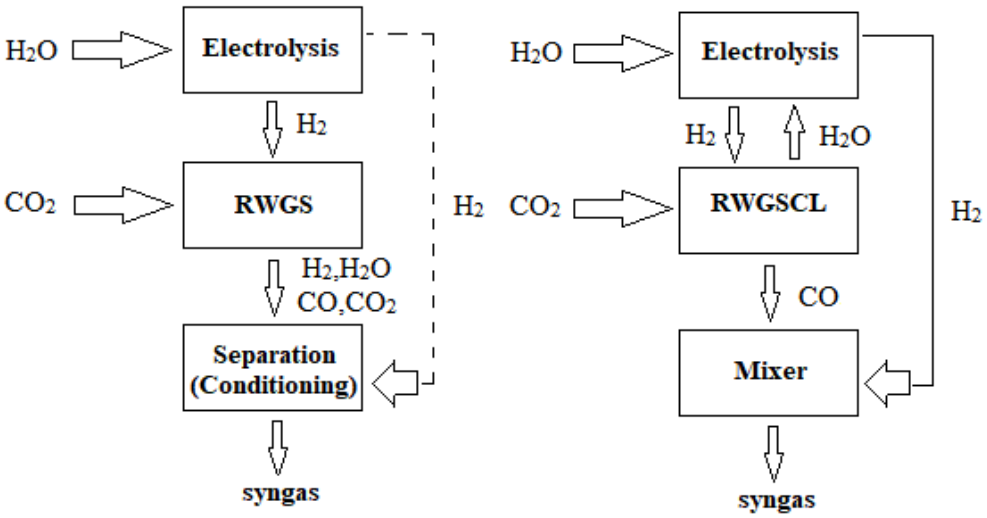

Figure 1- Comparison between RWGS and RWGS-CL

Source: adapted from WENZEL (2018).

When analyzing the schematics, it is theoretically easier to produce a CO-rich syngas in the RWGS-CL process. The literature reports cases where both the CO and the H_2O leaving their respective units achieve 100% conversion. Furthermore, due to the oxidation and reduction reactions occur in separate reactors, H_2 and CO_2 do not come into direct contact, preventing the unwanted formation of methane through the parallel methanation reaction. This eliminates the need for a subsequent separation step. Consequently, the CO exiting the unit can be easily mixed with H_2 to achieve the desired syngas composition, while water is recycled back to the electrolysis unit.

However, it is still necessary to reduce the reaction temperature of the chemical loop, because for the synthesis gas conversion into fuels it is necessary to integrate the RWGS-CL with the Fischer-Tropsch (FT) synthesis, which operates in lower temperature conditions (200-375ºC). Furthermore, when the process operates at lower temperatures, less energy is spent in the process, which is positive from an environmental and economic point of view.

In this context, it is worth noting that the integration of the RWGS-CL and FT reactions poses a thermodynamically less challenging scenario compared to the direct CO_2 hydrogenation reactions, which exhibit positive values of Gibbs free energy (ΔG) (PASTOR-PERÉZ et al., 2017). These positive findings reported in the literature regarding the RWGS route motivate the present study to investigate and evaluate the process of carbon dioxide conversion to carbon monoxide using the RWGS approach with chemical looping.

1.1 OBJECTIVES

Main objective

The main objective of this study is to propose a suitable model of the reactor for the Reverse Water-Gas Shift Chemical Looping (RWGS-CL) reaction to produce carbon monoxide from carbon dioxide.

Specific objectives

a) Evaluate different metal oxides for the oxidation and reduction reactions in the RWGS-CL process from a thermodynamic point of view;

b) Select a feasible metal oxide for the RWGS-CL based on a literature review and the results obtained in the thermodynamic analysis;

c) Search for the kinetics of the reaction with the chosen metal oxide;

d) Determine the mass and energy balances for the oxidation and reduction reactions;
e) Model and simulate a suitable fixed bed reactor;

1.2 STRUCTURE

Finally, this study is structured as follow:

- Chapter 1 introduces this work, as well as its justification, objective and structure.
- Chapter 2 presents background information, i.e., it expands the introduction by including more details about the carbon utilization and capture processes, the relevance and advantages of RWGS-CL.
- Chapter 3 describes the literature review of studies already conducted on chemical looping and RWGS-CL processes and the gap in the literature on the studied process.
- Chapter 4 outlines the method that elucidates the steps for formulating the studied model and discusses the parameters used for techno-economic and environmental assessments.
- Chapter 5 shows and discusses the results of this work.
- Chapter 6 closes this work with its conclusions and suggestions for future works.

2 BACKGROUND

Global warming is one of the major challenges faced by humanity today. The increase in greenhouse gas emissions, particularly carbon dioxide (CO_2), is contributing to significant climate change and negative environmental impacts. To mitigate these effects, it is crucial to adopt new routes for the production of green fuels and implement carbon capture and utilization processes.

The transition to a more sustainable energy matrix is essential for reducing CO_2 emissions and limiting global warming. In this regard, the production of green fuels is a promising approach. These fuels are derived from renewable sources such as biomass, solar, and wind energy, and have a carbon-neutral cycle. This means that during their production and use, they do not release additional CO_2 into the atmosphere as the emitted carbon is offset by the CO_2 uptake from renewable sources (PANWAR et al., 2011).

However, to achieve a complete transition to green fuels, it is necessary to develop efficient and economically viable production routes (UNITED NATIONS, 2021). This is the importance of CO_2 capture and utilization processes. These processes involve capturing CO_2 emitted from various sources such as power plants and industrial processes and converting it into useful products such as fuels, materials, or chemicals.

CO_2 capture and utilization technologies offer several advantages. They contribute to the reduction of net CO_2 emissions, helping to mitigate global warming. Additionally, these processes can harness CO_2 as a valuable feedstock, reducing dependence on fossil resources and promoting a circular economy (RAHMAN et al., 2017). For instance, captured CO_2 can be converted into synthetic fuels through chemical reactions such as reverse water-gas shift (RWGS) and Fischer-Tropsch (FT) synthesis, enabling the substitution of fossil fuels with more sustainable alternatives (KIRSCH et al., 2020).

However, it is important to highlight that CO_2 capture and utilization are not singular solutions to global warming. They must be implemented in conjunction with other measures such as energy efficiency, increasing the share of renewable sources, and adopting sustainable consumption practices, as well as removing CO_2 from the atmosphere (negative emissions technologies). Furthermore, ensuring the economic viability of these processes and continuing investment in research and development to enhance efficiency and reduce associated costs of CO_2 capture and utilization are crucial (MCLAUGHLIN et al., 2023).

In summary, global warming demands urgent and comprehensive actions. The transition to green fuels and the implementation of CO_2 capture and utilization processes play a crucial role in reducing greenhouse gas emissions and promoting a more sustainable economy. Combined with other measures, these efforts can significantly contribute to mitigate the impacts of climate change and creating a sustainable future for the next generations.

2.1 OVERVIEW OF MAIN CARBON CAPTURE AND UTILIZATION TECHNOLOGIES

As global efforts to mitigate climate change, the intensification of carbon capture and utilization (CCU) technologies emerge as promising strategies to reduce carbon dioxide emissions and promote a sustainable carbon economy (AL-MAMOORI et al., 2017). This section provides an overview of the main technologies used for carbon capture and utilization, highlighting their potential benefits and challenges.

2.1.1 Carbon Capture Technologies

2.1.1.1 Post-Combustion Capture

Post-combustion capture involves removing CO_2 from the exhaust gases emitted by fossil fuel power plants or industrial facilities. Techniques such as chemical absorption, adsorption, and membrane separation are commonly used to capture CO_2 for subsequent utilization or storage (CHAO et al., 2021).

2.1.1.2 Pre-Combustion Capture

Pre-combustion capture is employed in integrated gasification combined cycle (IGCC) power plants and gasification processes. It involves converting fossil fuels into syngas, which is further processed to separate CO_2 for utilization or storage (BABU et al., 2015).

2.1.1.3 Oxyfuel Combustion

Oxyfuel combustion involves burning fossil fuels with pure oxygen, resulting in an exhaust gas primarily composed of CO_2 and water vapor. The CO_2 can then be captured and utilized or stored (STANGER et al., 2015).

2.1.2 Carbon Utilization Technologies

2.1.2.1 Mineralization

Mineralization refers to the conversion of captured CO_2 into stable mineral forms. This process involves reacting CO_2 with alkaline materials to produce carbonates or bicarbonates, which can be used in various applications such as construction materials or industrial processes (OUYANG et al., 2022).

2.1.2.2 Chemical Conversion

Chemical conversion technologies convert CO_2 into valuable chemicals and fuels. Examples include the production of methanol, formic acid, or methane through catalytic processes such as the reverse water-gas shift (RWGS) reaction (FURTER, 2020).

2.1.2.3 Biological Conversion

Biological conversion methods utilize microorganisms or algae to convert CO_2 into bio-based products, including biofuels, bioplastics, and biochemicals. These approaches offer potential for sustainable carbon utilization and resource diversification (SAM AND BARIK, 2019).

2.1.2.4 Eletrochemical Conversion

Electrochemical conversion refers to a process in which electrical energy is used to drive a chemical reaction, typically involving the conversion of one chemical species into another. This conversion is facilitated by the use of electrodes and an electrolyte solution. In electrochemical conversion, electrical energy is harnessed to initiate and control chemical transformations, making it a valuable technique in various fields, including energy storage,

electrocatalysis, and electrochemical sensors. It plays a crucial role in technologies such as batteries, fuel cells, and electrolysis, where electrical energy is converted into chemical energy or vice versa (OVERA et al., 2022).

2.1.2.5 Photochemical Conversion

Photochemical conversion is a process in which the energy of light is used to trigger chemical reactions in chemical substances or materials. This occurs when photons of light strike a substance, providing the necessary energy to break or form chemical bonds, resulting in chemical transformations. A common example of photochemical conversion is photosynthesis, where sunlight is used by plants to convert carbon dioxide and water into glucose and oxygen. Additionally, photocatalysis is another important application of photochemical conversion, where light is used to accelerate chemical reactions on the surfaces of photosensitive catalysts. Photochemical conversion plays a fundamental role in various areas, including environmental chemistry, solar energy, and advanced materials technologies (ANDREONI et al., 2021).

2.1.3 Challenges and Opportunities

While carbon capture and utilization technologies hold significant potential, there are several challenges to be addressed. These include high energy requirements, scalability, economic viability, and the need for supportive policy frameworks. Collaboration between academia, industry, and policymakers is crucial to overcoming these barriers and promoting widespread adoption of CCU technologies. Continuous research, development, and collaboration will be key to realizing the full potential of these technologies and accelerating global decarbonization efforts.

2.2 RELEVANCE AND ADVANTAGES OF RWGS-CL: A PROMISING APPROACH FOR CO_2 CAPTURE AND UTILIZATION

The RWGS reaction has emerged as a relevant alternative for CO_2 utilization. In this reaction, CO_2 is converted into carbon monoxide (CO) in the presence of hydrogen (H_2). RWGS enables the conversion of CO_2 into valuable synthesis gas (syngas), which can be utilized in the production of fuels and chemicals.

The traditional RWGS faces the challenge of undesired parallel reactions, such as methanation, which reduce the selectivity of the reaction and decrease the desired CO production. Additionally, methane formation complicates the separation of CO from other gases and generates unwanted by products (LE SACHÉ et al., 2020).

To overcome these challenges, the approach of RWGS with Chemical Looping (RWGS-CL) has been studied as a promising alternative. In this method, RWGS is divided into two steps, reduction and oxidation, using an oxygen carrier material, typically a metal oxide, to regenerate the oxide used in the reaction. This strategy prevents the undesired formation of methane, as there is no direct contact between H_2 and CO_2.

RWGS-CL offers advantages over traditional RWGS, as the methanation reaction is avoided. This facilitates the production of a CO-enriched syngas, which is essential to produce fuels and chemicals, eliminating the need for a separate CO separation step. This simplification results in energy savings and reduced operational costs (DAZA et al., 2014).

The proper selection of the oxygen carrier material plays a crucial role in the performance of RWGS-CL. Several oxygen carrier materials have been studied in the scientific literature, including transition metal oxides, perovskites, and lanthanide oxides. These materials exhibit efficient oxygen storage and release capabilities under different operating conditions, contributing to improved efficiency and selectivity of the RWGS-CL reaction.

The selection of Oxygen Carrier Materials (OCM) for a chemical looping process involves an initial thermodynamic screening, followed by kinetic investigations and evaluation of the physicochemical properties, such as thermal stability, of the selected OCMs. This approach aims to ensure thermodynamic feasibility and efficiency of the chemical looping process. It is important to note that further kinetic investigations are justified only if the process is considered thermodynamically viable and efficient within the given constraints (WENZEL, 2018).

In summary, RWGS with Chemical Looping (RWGS-CL) stands out as a relevant alternative for CO_2 conversion. By overcoming the limitations of traditional RWGS, RWGS-CL enables selective CO production from CO_2. Therefore, for optimal efficiency and performance of RWGS-CL, the proper selection of the oxygen carrier material becomes a crucial point of investigation.

2.3 ROLE OF CHEMICAL PROCESS SIMULATORS IN CARBON CONVERSION: ADVANCES, CHALLENGES AND FUTURE DIRECTIONS

Chemical process simulators play a crucial role in advancing research and modeling of chemical engineering projects for carbon dioxide conversion. These tools are essential for understanding, analyzing, and optimizing processes related to carbon conversion, contributing to the reduction of greenhouse gas emissions and the transition to a low-carbon economy.

Chemical process simulation plays a vital role in understanding and optimizing complex systems. The software developed by AspenTech, for example, offers a powerful platform for modeling and simulating these processes, providing ease in solving the equations that describe the physical, chemical, and thermodynamic interactions involved (ALMEIDA et al., 2020).

One of the main advantages of chemical process simulators is the ability to model and simulate different scenarios and operating conditions. With the use of these tools, researchers can create virtual models of CO_2 conversion processes, allowing the analysis of key variables such as temperature, pressure, gas composition, and mass flows. This computational approach offers the possibility of conducting virtual experiments and exploring different carbon conversion strategies, saving time and resources.

Furthermore, chemical process simulators enable the modeling and simulation of complex CO_2 conversion systems. These tools allow a deep understanding of the physical and chemical phenomena involved in conversion processes, enabling the identification of bottlenecks, parameter optimization, and overall system performance improvement (CHEMENGGUY, 2023).

Moreover, chemical process simulators facilitate feasibility studies by evaluating technical and economic aspects, assessing the performance of different conversion systems, energy efficiency, operational costs, and environmental impacts. These detailed analyses help researchers identify the best solutions and make informed decisions during the development of carbon conversion projects (HUNPINYO et al., 2013).

However, while chemical process simulation is widely used in various areas of chemical engineering, the literature still lacks studies that explore the use of this approach to evaluate and simulate RWGS-CL. Few studies have been dedicated in applying process simulation in the specific context of RWGS-CL, which represents a research gap.

Furthermore, the scarcity of studies conducting techno-economic and environmental assessments of RWGS-CL is an additional limitation. A comprehensive evaluation of these aspects is essential to determine the technical, economic, and environmental feasibility of this CO_2 conversion approach. Therefore, it is crucial to encourage future research that explores the potential of chemical process simulation and includes a comprehensive assessment of the

techno-economic and environmental aspects of RWGS-CL, contributing to the sustainable development of more efficient and economically viable carbon conversion solutions.

2.4 THE IMPORTANCE OF TECHNO-ECONOMIC AND ENVIRONMENTAL ANALYSIS FOR RWGS-CL: A GAP IN THE LITERATURE AND FUTURE RESEARCH OPPORTUNITIES

Techno-economic and environmental analysis play a crucial role in the study and development of chemical processes, such as the RWGS-CL. This analysis involves the systematic evaluation of the technical, economic, and environmental aspects of a specific process, enabling a comprehensive understanding of its feasibility and impacts. It encompasses the estimation of capital and operational costs, evaluation of energy performance, investment analysis, profitability calculations, and determination of the project's economic viability. This analysis is essential for identifying efficiency, financial feasibility, and return on investment, assisting in strategic decision-making (KOBOS et al., 2020).

On the other hand, environmental analysis focuses on evaluating the environmental impacts of a chemical process. This involves the identification, quantification, and assessment of the process's effects on the environment, including aspects such as greenhouse gas emissions, resource consumption and waste generation. Environmental analysis aims to identify mitigation measures and develop sustainable strategies to reduce environmental impacts (MU et al., 2020).

In the specific context of RWGS-CL, techno-economic and environmental analysis is of utmost importance. This approach to CO_2 utilization has the potential to mitigate greenhouse gas emissions and promote a low-carbon economy. However, a comprehensive assessment of the techno-economic and environmental aspects of RWGS-CL is a gap in the scientific literature.

In the next chapter, a detailed literature review will be presented regarding the RWGS-CL. The review will address the key studies and scientific works that explore this carbon capture approach. This review will provide a broader understanding of the current state of knowledge in this field.

3 LITERATURE REVIEW

3.1 Chemical Looping Process

Chemical looping processes have shown a promising potential for the production of clean fuels and for capturing CO_2. This topic will present what is available in the literature on chemical loop processes in the last years.

Adanez et al. (2012) carried out a literature review on Chemical-Looping Combustion (CLC) and Chemical-Looping Reforming (CLR) processes, presenting the main advances of these technologies until 2010. In these processes, oxygen is transferred from the air to the fuel through a solid oxygen carrier. The review showed that by 2010 more than 700 different materials based on Ni, Cu, Fe, Mn, Co, as well as other mixed oxides and low-cost materials, were used in these processes.

Kuo et al. (2013) evaluated the use of nickel ferrite oxygen carriers ($NiFe_2O_4$) for a chemical looping process from experimental data and indicated that the spinel structure phase showed greater redox cycling behavior and better stability than the standard NiO and Fe_2O_3. Thus, the results demonstrate the feasibility of using the $NiFe_2O_4$ preparation as an oxygen carrier in the reversible chemical looping process (CLP).

Udomsirichakorn and Salam (2014) presented a literature review on CaO-based chemical loop gasification (CLG) in order to solve the problem of undesirable CO_2 and tar formation in the biomass gasification for hydrogen production. The work demonstrated that CaO-based CLG using biomass as feedstock has gained more attention in recent years as it presents itself as a promising process for the production of renewable, sustainable and ecologically correct hydrogen.

Meng et al. (2016) performed a multi-stage chemical looping combustion process simulation using Aspen Plus and a plug-flow reactor model for the gasification step incorporating kinetic data in the simulation. The reactor size was varied and the char conversion and power output network were examined, and the optimal reactor size for each multistage configuration was determined. The effect of the multi-stages over the exhaust composition was investigated, and the simulation results showed that multi-staging allows using several smaller reactors with the same total volume without significant effects on the net energy production.

Evdou et al. (2016) studied the use of ferrites of general formula $MeFe_2O_4$ (Me = Mn, Ni, Zn, Co, Cu) in Chemical Looping Combustion in a fixed bed laboratory scale pulse reaction

unit. As a result, Cu ferrites showed to be very active in the CH_4 oxidation, while although Zn and Ni ferrites also gave high methane conversions, they deactivated very quickly after the redox cycles. Mn ferrites showed relatively low activity, while Co ferrites showed moderate methane conversion, but remarkable stability during subsequent redox cycles.

Mehrpooya et al. (2017) proposed an integrated process for the co-production of hydrogen and electricity by the integration of biomass gasification, chemical looping combustion, and CO_2-captured electricity generation cycle. Their work showed high energy efficiency and zero CO_2 emissions.

Wei et al. (2018) evaluated the production of hydrogen from vegetable oil by chemical looping, using hematite as oxygen carrier, and aeration took place in a fixed bed reactor at temperatures of 1023.15-1173.15 K. The analyzes demonstrated that the maximum H_2 composition was 91.72% when hematite oxygen carriers consisting of Fe_2O_3, Al_2O_3 and SiO_2 were used, showing that hematite is a promising oxygen carrier candidate for hydrogen generation from vegetable oil by chemical looping process.

Sandvik (2019) quantified the impact of chemical looping reformer operating conditions on overall system yields (methane to syngas). His work was performed on ASPEN PLUS process simulator, considering a concurrent moving bed fuel/reducer reactor and a fluidized bed air/combustor reactor. As a result, the author concluded that the looping process allows equivalent synthesis gas yield compared to the autothermal reformer, with a 7-13% reduction in natural gas feedstock.

Lyngfelt et al. (2019) evaluated scale up strategies of biomass chemical looping combustion processes, studying their effects on process performance. Pilot operation experiences demonstrated the process feasibility and the potential to work at large scale.

Hu and Wang (2020) studied the use of Fe_2O_3, CaO, CaO and Fe_2O_3 mechanically and chemically mixed with $Ca_2Fe_2O_5$, in the RWGS-CL. The results showed that the reduction of Fe_2O_3 to Fe_3O_4 produced CO_2, while the transition from Fe_3O_4 to Fe occurred beyond 650 °C released CO.

Zhang et al. (2021) studied the coal direct chemical looping (CDCL) process in a 250 kW integrated pilot unit using iron-based oxygen carriers over 1000 h tests. The results from the pilot unit tests confirmed the CDCL concept as a promising coal combustion technology for heat and power generation with CO_2 capture in a 288 hours continuous operation test, achieving >96% coal conversion with a purity of CO_2 >97%.

Ahmed et al. (2023) conducted a techno-economic comparison between combustor integrated steam reforming (CISR) and sorption-enhanced chemical looping steam reforming (SE-CLSR) for in-situ hydrogen (H_2) production from methanol steam reforming (MSR). Using Aspen Plus V11 simulation platform, they assessed the economic viability of hydrogen generation through the MSR process. The SE-CLSR model was developed with NiO as the oxygen transfer material (OTM). Simulations were performed to analyze the impact of different operating conditions, such as temperature, steam-to-methanol (S/M) ratio, and catalyst weight methanol molar ratio, on methanol conversion, hydrogen yield, and CO selectivity. Sensitivity analysis of the models was conducted to identify optimal operating conditions. The estimated hydrogen production costs were $2.66/kg and $2.79/kg for CISR and SE-CLSR processes, respectively.

Peng et al. (2023) introduced a novel method called CLC-SECLR$_{HC}$ for the co-production of hydrogen (H_2) and carbon monoxide (CO) through natural gas reforming. The process combines chemical looping combustion (CLC) and sorption-enhanced reforming (SE-CLR$_{HC}$) in two separate streams. CLC provides CO_2 and energy to SE-CLR$_{HC}$, which generates H_2 and CO with higher purity. A techno-economic assessment was conducted to determine the optimal operating conditions, including reactant ratios, temperatures, and heat integration. Under the optimal conditions, the process achieved high H_2 and CO production efficiency, with an exergy efficiency of 70.28%. The economic analysis demonstrated the viability of the proposed process, with a payback period of 6.2 years and an internal rate of return of 11.5%. These findings suggest that CLC-SECLR$_{HC}$ is a promising approach for efficient and cost-effective H_2 and CO production from natural gas.

3.2 Reverse Water Gas Shift Chemical Looping

This topic presents the state-of-the-art of RWGS-CL process, demonstrating its advantages and disadvantages.

Daza et al. (2014) used perovskites as oxygen-carrying material for RWGS-CL. They studied strontium-doped lanthanum cobaltites ($La_{1-x}Sr_xCoO_{3-\delta}$), with x equal to 0, 0.25, 0.5, 0.75 and 1. The work indicated that $La_{0.75}Sr_{0.25}CoO_{3-\delta}$ (X=0.25) can be used as oxygen carrier material in the RWGS-CL, however the temperature difference between the oxidation and reduction reactions is a disadvantage regarding the process energy efficiency.

Daza et al. (2015) tested a new oxygen-carrying material to solve energy efficiency related issues. The chosen material was $La_{0.75}Sr_{0.25}Co_{(1-Y)}Fe_YO_3$ with Y = 0, 0.5, 0.75 and 1. Y=1 showed the best results. The perovskite crystal structure remained stable during the redox cycle. Also, the temperature was the same (550ºC) for both reactions, solving the problem found previously by the authors. They observed that the CO formation rates increased during the first cycles and stabilized in the third cycle due to the increase in the accumulated amount of oxygen vacancies on the perovskite surface, which corroborated the results of the density functional theory that directly correlate the CO_2 binding strength to the amount of oxygen vacancy.

To find higher yields than those found in RWGS-CL works using perovskites, Wenzel et al. (2017) tested a modified iron oxide (80 wt% Fe_2O_3-$Ce_{0.5}Zr_{0.5}O_2$) as a new oxygen-carrying material. The oxidation and reduction reactions were favored by high temperatures and the material showed gradual deactivation, decreasing the CO yield during the first 100 redox cycles. Thereafter, a steady-state CO yield was achieved for the next 400 cycles. Kinetics of the oxidation and reduction reactions were obtained from the experimental data.

Wenzel (2018) analyzed the storage capacity of different metal oxides (Fe_3O_4, FeO, NiO, CoO, ZnO, SnO, Cu_2O, Mn_3O_4 and CeO_2). Among the various oxides tested, magnetite was the material with the highest CO yield in the redox cycle. To increase the stability of the magnetite during such cycles, the author used a mixture of 80 wt% Fe_2O_3 and 20 wt% $Ce_{0.5}Zr_{0.5}O_2$.

Wenzel et al. (2018) evaluated the performance of fixed-bed and fluidized-bed reactors for the RWGS-CL, through simulation in the MATLAB software, using two performance indicators: the average concentration of CO and which oxygen-carrying material would be the best for the reactions. The fixed bed reactor proved to be advantageous for the RWGS-CL process due to larger degrees of freedom of operation in relation to the fluidized bed reactor, although the configuration of this reactor can minimize problems associated with the sintering of the material.

Kuhn et al. (2018) hold the patent for supported perovskite oxide composites for the conversion of CO_2 to CO. The patent disclosed a catalyst containing a perovskite oxide and an oxide support, their preparation methods, and their application for conversion of CO_2 by a reverse water gas shift chemical looping.

Hare et. al (2019) used $La_{0.75}Sr_{0.25}FeO_3$ (LSF) supported on SiO_2, 25% of mass, for the RWGS-CL. The carbon monoxide yields were 150% larger when compared to unsupported

perovskite after reduction at 600 °C. Although the CO yield higher than for unsupported perovskite, it was lower in relation to the aforementioned works.

Lee et al. (2020) tested four metal oxide core-shell (CeO_2, NiO, Co_3O_4 and Co_3O_4-NiO). The perovskite $La_{0.75}Sr_{0.25}FeO_3$ encapsulated with Co_3O_4-NiO showed to be the most promise oxygen carrier material for RWGS-CL, because it showed larger CO generation and exhibited long-term stability. It was also observed an increase in CO yield until the second redox cycle, and further, the CO yield decreased and stabilized.

An article on SciTech (2020) daily cited that Japanese scientists set a record for the highest conversion rate of carbon dioxide at low temperatures with copper-modified indium oxide ($Cu_2In_2O_5$) for the RWGS-CL.

Castellanos-Beltran et al (2021) evaluated the use of nickel iron oxide ($NiFe_2O_4$) as oxygen carrier material in a self-controlled heating medium induced by magnetic heating. The CO yield found was 1.37 ± 0.07 μmol / g of $NiFe_2O_4$, lower yield among the aforementioned works. The studied material showed good stability, retaining its activity for several cycles, however its stability was slowly reduced with exposure to H_2.

Makiura et al. (2022) studied the conversion of CO_2 to CO by reverse water-gas shift using chemical looping and tested Co-In_2O_3 as an oxygen storage material. The authors obtained conversions from CO_2 to CO at lower temperatures (723–823 K) than the traditional reaction without the catalyst, and in addition the redox cycle showed a durability of 10 cycles.

Iwama et al. (2022) aimed to convert CO_2 to CO through the RWGS-CL reaction to promote resource recycling. Composite pellets of metal oxide/perovskite and silica were developed, optimizing the experimental conditions using machine learning and Bayesian optimization. Transfer learning was applied to improve the accuracy of mathematical models. Based on the best combinations of variables, CO_2 conversion was enhanced by considering electronic and structural information of the metal oxides, while H_2 conversion depended on the experimental conditions. The mathematical models were able to predict CO_2 and H_2 conversions, allowing the identification of promising candidates for future experiments. The use of transfer learning was highlighted as a challenge to be explored in future studies involving samples from different experimental systems.

Shi et al. (2023) focused on the development of perovskite/silica composite pellets for the low-temperature reverse water-gas shift chemical looping (RWGS-CL) for conversion of CO_2 to CO. The pellets, consisting of 25% $La_{0.5}Ba_{0.5}FeO_3$ (LBF) by weight, were prepared using extrusion and compression methods to ensure sufficient crushing strength. X-ray

fluorescence (XRF) and X-ray diffraction (XRD) analyses confirmed that the resulting material had a composition of 26.6% LBF in SiO_2, exhibiting a combined structure of LBF and SiO_2 components. Temperature-programmed reduction (TPR) and oxidation (TPO) experiments revealed that the LBF/SiO_2 pellets achieved CO_2 to CO conversion at 550°C, surpassing the performance of LBF by 50°C. The material's high stability was demonstrated through long-term RWGL-CL experiments, combined with XRD and XPS analyses. The CO_2 to CO yields were 2.21, 2.41, and 2.35 mmol/g_{LBF} for 10 mm pellets, 6 mm pellets, and extruded pellets, respectively. Deactivated pellets could be regenerated through thermal treatment in air atmosphere after intentional reduction. All pellets exhibited stable redox properties over 50 cycles of semi-batch reactor experiments, indicating the potential of LBF/SiO_2 granules for further scale-up evaluation.

Flores-Granobles and Saeys (2023) conducted a study on the dynamic pressure-swing chemical looping process for the recovery of CO from blast furnace gas. They validated the proposed model by simulating both the conventional RWGS and RWGS-CL processes. The conventional RWGS process operated with a nickel-based catalyst and produced an equilibrium mixture of CO_2-CO-H_2-H_2O. In contrast, the RWGS-CL process divided the reaction into two subreactions using an iron-based solid intermediate. In the oxidizing regime, CO_2 was fed into the reactor and oxidized Fe to FeO, resulting in a CO-rich gas mixture. When the reducing regime started, CO_2 feed was stopped and H_2 was introduced, reducing FeO to Fe and producing a H_2-rich gas mixture. The RWGS-CL process improved CO_2 and H_2 conversions while increasing the CO molar fraction in the product gas. The simulated results were compared with the conventional RWGS process, demonstrating promising outcomes consistent with the findings of Wenzel (2018), regarding the production of a CO-rich stream through the RWGS-CL process.

Based on the literature review conducted, it can be observed that the RWGS-CL technology has attracted significant interest in the scientific community due to its potential for efficient CO recovery from various sources. However, despite considerable advancements in understanding and applying this technology, there are still gaps to be filled in the literature.

One of the main identified gaps is the focus of studies on laboratory or pilot-scale simulations and experiments, with a greater emphasis on determining suitable oxygen carrier materials. It is essential that more efforts be directed towards scale up the RWGS-CL process to industrial levels, considering the complexities associated with large-scale operation, such as energy efficiency, integration with other processes, and economic feasibility.

Another important aspect is the lack of studies on economic viability and environmental assessments of the RWGS-CL process compared to other CO_2 conversion technologies. Determining capital and operational costs, as well as analyzing the environmental impact associated with the process, are crucial for assessing the technical and economic feasibility of commercial implementation of RWGS-CL.

Therefore, to address these gaps, further experimental studies and simulations at different scales are needed, optimizing operational conditions, evaluating economic viability, and environmental assessment. These additional studies will contribute to advancing the knowledge of RWGS-CL and its practical application in the efficient recovery of CO from various sources, driving the development of more sustainable and low-carbon technologies.

The difference in this work is to present a comprehensive and robust model, which takes into account mass balance, energy and pressure loss. This model was developed in modeling software to evaluate the performance of a multitubular fixed bed reactor for RWGS-CL. The analysis covers the behavior of the reactor under different flow rates, aiming for industrial applicability. Furthermore, we seek to carry out a technical and environmental assessment of the application of RWGS-CL, considering not only the efficiency of the process, but also its environmental impacts and technical feasibility for possible implementations.

4 METHODS

4.1. Thermodynamic Analysis

In this work, simulations were carried out in Aspen Plus® process simulator, using the Peng-Robinson thermodynamic package (PR EoS). Thermodynamic analyses were carried out to evaluate the effects of temperature and feed molar ratio on RWGS-CL conversion and yields. The operating pressure of the oxidation and reduction reactors was set at 22 bar due to further integration to the Fischer-Tropsch synthesis, which operates at such pressure.

A Gibbs reactor model was employed, considering CO as the product of the oxidation reaction and unconverted CO_2, while water and unconverted hydrogen were considered for the reduction reaction. This reactor model is based on the Gibbs energy minimization principle, which assumes that a system at its minimum Gibbs energy value is a thermodynamically favorable system.

For a given system, the total Gibbs energy G^{tot} can be defined as the sum of the chemical potential of all components, as shown in Equation 5.

$$G^{tot} = \sum_{i=1}^{N} n_i \mu_i \tag{5}$$

Where n_i is the number of moles of component i, μ_i is the chemical potential, and N is the total number of components in the system.

Equation 6 describes the definition of the chemical potential of species i.

$$\mu_i = {\Delta G_{fi}}^0 + RTln(x_i \varphi_i \frac{P}{P_0}) \tag{6}$$

Where ${\Delta G_{fi}}^0$ is the standard Gibbs energy of formation of species i, R is the molar gas constant, T is the absolute temperature, x_i is the molar fraction of species i, φ_i is the fugacity coefficient calculated using the PR EoS, P is the operating pressure, and P_0 is standard pressure.

By replacing Equation 6 in Equation 5, gives:

$$G^{tot} = \sum_{i=1}^{N} n_i \Delta G_{fi}{}^{0} + n_i RT ln\left(x_i \varphi_i \frac{P}{P_0}\right) \quad (7)$$

Due to the minimization of Equation 5 (carried out by Equation 7), at a given temperature, pressure and feed molar ratio, the thermodynamic equilibrium composition of each species in the reactor is provided. Therefore, only the input stream characteristics must be specified, since compositions do not depend on the reaction kinetics (ÖZKARA-AYDINOĞLU, 2010).

For evaluation of the results, CO_2 and H_2 conversions were calculated according to equations 8 and 9.

$$X_{CO2} = \frac{F_{CO2,in} - F_{CO2,out}}{F_{CO2,in}} * 100\% \quad (8)$$

$$X_{H2} = \frac{F_{H2,in} - F_{H2,out}}{F_{H2,in}} * 100\% \quad (9)$$

Where X_i is the molar conversion of species i, $F_{i,in}$ is the molar inflow of species i, and $F_{i,out}$ is the molar outflow of species i.

4.2 Determination of reaction kinetics

Kinetics is the study of the rate of a reaction and the factors that influence it, looking for ways to control the reaction rate. Such rate can be represented by the consumption of a reactant and generation of a product.

The kinetics presented in the present work were developed for the oxidation and reduction reactions, based on equations 10 and 11, respectively.

Oxidation $$3Fe + 4CO_2 \leftrightarrow Fe_3O_4 + 4CO \quad (10)$$

Reduction $$Fe_3O_4 + 4H_2 \leftrightarrow 3Fe + 4H_2O \quad (11)$$

In this work, the kinetics presented by Wenzel (2018) was used. When comparing the kinetics obtained with the kinetic functions, it was noted that for oxidation, the kinetic model that best describes this reaction is the reaction order (Fn) described by Equation 12.

$$f(\xi) = (1-\xi)^n \tag{12}$$

Where ξ is the reaction extent and *n* is the order of the reaction.

The reduction reaction is similar to the geometric contraction model, which is described by Equation 13:

$$f(\xi) = (1-\xi)^{1/2} \tag{13}$$

Thus, the kinetic rate equation is described by Equations 14 and 15, for the oxidation and reduction reactions, respectively.

$$r_{ox} = k_{ox}^{0} \exp\left(-\frac{E_{A,ox}}{RT}\right)(1 - x_{Feo_{\frac{4}{3}}})^{n_{ox}} x_{CO_2}^{m_{ox}} \tag{14}$$

$$r_{red} = k_{red}^{0} \exp\left(-\frac{E_{A,red}}{RT}\right)(1 - x_{Fe})^{n_{red}} x_{H_2}^{m_{red}} \tag{15}$$

Where k^0 is the Arrhenius pre-exponential factor, E_A is the activation energy, R is the universal gas constant, T is the temperature, x is the mole fraction, $and\ m$ is the order of the gas phase reaction, *red* is the reduction reaction, *oxi* is the oxidation and n is the order of the solid phase reaction.

To calculate the reaction rate from Equations 14 and 15, the kinetic data for the redox reaction using magnetite are shown in Table 1 (WENZEL, 2018).

Table 1 - Magnetite kinetic data for the redox reaction.

Estimated parameter	Oxidation	Reduction
m	1.002	0.724
n	0.618	0.461
k^0(mol/Kg$_{OSM}$/s)	18199	1140
E_a(kJ/mol)	111.6	80.7
R (kJ/kmol/K)	8.314	8.314
T (K)	1073.15	1073.15

Wenzel (2018) estimated the kinetic data of RWGS-CL through nonlinear least-squares regression analysis. The procedure involved fitting kinetic models to the experimental data using the *nlinfit* function in MATLAB. This function allowed for the estimation of kinetic parameters by finding values that minimize the difference between the model-predicted values and the experimental data.

Additionally, confidence intervals for the parameters were calculated using the *nlparci* function. These intervals provide a measure of uncertainty associated with the estimates of the kinetic parameters.

The coefficient of determination, R^2, was computed to assess the quality of the model fit to the experimental data. It provides a measure of the proportion of data variability explained by the model. Values closer to 1 indicate a better fit of the model to the experimental data.

4.3 Mathematical Model

To carry out the simulation of the reactor, mass balance equations were developed for the gas phase and for the liquid phase. In this section, the modeling of these equations will be presented. The model presented in this section was developed in the commercial software Aspen Custom Modeler.

4.3.1 Fixed bed reactor modeling

In this study, it was necessary to develop a mathematical model for plug flow fixed-bed reactors in order to describe the process. Fixed-bed reactors are the primary type of catalytic reactors used in large-scale chemical synthesis. The process involves different gaseous

chemical species reacting on the catalyst surface, which is positioned in a fixed location within the reactor (PEREIRA, 2022).

The mathematical modeling of the fixed-bed reactor was conducted by considering microscopic mass and energy balances. Figure 2 illustrates the proposed scheme for the conceptual chemical looping.

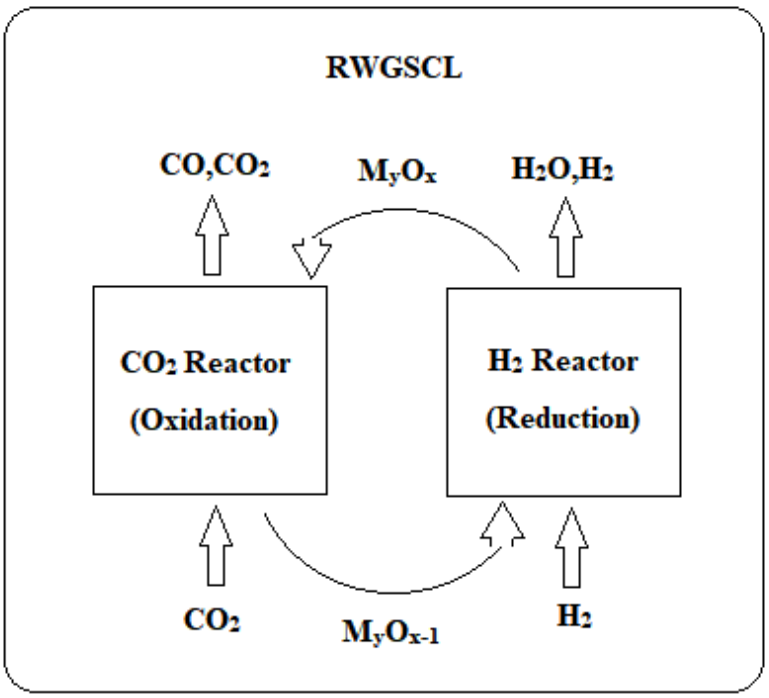

Figure 2 – Conceptual scheme of de RWGS-CL.
Source: adapted from WENZEL (2018).

4.3.1.1 Gas-phase mass balance

For the mass balance, the continuity equation was considered (Equation 16).

$$\frac{\partial \rho}{\partial t} + \frac{1}{r}\frac{\partial}{\partial r}(\rho r v_r) + \frac{1}{r}\frac{\partial}{\partial \theta}(\rho v_\theta) + \frac{\partial}{\partial z}(\rho v_z) = 0 \tag{16}$$

The microscopic mass balance was defined considering only one spatial direction as shown in Equation 17.

$$\frac{\partial \rho_\alpha}{\partial t} = -\frac{\partial}{\partial z}\left(\rho_\alpha^{(g)} v^{(g)} + j_\alpha^{(g)}\right) + \sigma_\alpha^M \tag{17}$$

Where, $\rho_{\alpha}^{(g)}$ is the specific mass, $v^{(g)}$ is the gas phase superficial velocity, $j_{\alpha}^{(g)}$is the diffusive flux, σ_{α}^{M} is the specific source term, t is the time, α is gas component index and z is the axial spatial coordinate.

Then, the diffusive term was neglected due to the high velocity of the gas (Equation 18).

$$\frac{\partial \rho_{\alpha}}{\partial t} = -\frac{\partial}{\partial z}\left(\rho_{\alpha}^{(g)} v^{(g)}\right) + \sigma_{\alpha}^{M} \tag{18}$$

Since $\rho_{\alpha}^{(g)}$ is given by Equation 19, the balance can be rewritten as Equation 20.

$$\rho_{\alpha}^{(g)} = c_{t}^{(g)} M_{\alpha} x_{\alpha}^{(g)} \varepsilon \tag{19}$$

Where $c_{t}^{(g)}$ is the molar concentration in the gas phase, M_{α} is the molar mass, $x_{\alpha}^{(g)}$ is the mole fraction, $and\ \varepsilon$ is the fixed bed void fraction. Substituting $\rho_{\alpha}^{(g)}$ into the mass balance equation (Equation 18), gives Equation 20

$$\frac{\partial (c_{t}^{(g)} M_{\alpha} x_{\alpha}^{(g)} \varepsilon)}{\partial t} = -\frac{\partial}{\partial z}\left(c_{t}^{(g)} M_{\alpha} x_{\alpha}^{(g)} \varepsilon v^{(g)}\right) + \sigma_{\alpha}^{M} \tag{20}$$

The term σ_{α}^{M} for the gas phase is defined as shown by Equation 21.

$$\sigma_{\alpha}^{M} = M_{\alpha} \sum_{j}^{N_R} \nu_{\alpha,j} r_{j,eff.} \tag{21}$$

Where, $\nu_{\alpha,j}$ is the stoichiometric coefficient; $r_{j,eff.}$ is the corresponding effective reaction rate.

Substituting Equation 21 into the mass balance, gives Equation 22.

$$\frac{\partial x_{\alpha}^{(g)}}{\partial t} = -\frac{\partial (x_{\alpha}^{(g)} v^{(g)})}{\partial z} + \frac{1}{\varepsilon c_{t}^{(g)}} \sum_{j}^{N_R} \nu_{\alpha,j} r_{j,eff.} \tag{22}$$

To convert between the rate expressions, the solid phase density $\rho^{(s)}$ and the fixed bed void fraction can be used according to

$$r_{j,eff} = (1-\varepsilon)\rho_{\alpha}^{(s)} r_{j,eff.}^{M} \tag{23}$$

Where, $r_{j,eff.}^{M}$ is the reaction rate in terms of moles.

The effectiveness factor is introduced to consider the mass transfer resistances in the pores of the oxygen storage material and the resulting decrease in reactivity (Equation 24).

$$r_{j,eff}^{M} = \eta_{eff} r_{j}^{M} \tag{24}$$

Where, η_{eff} is the effectiveness factor of the reaction rate, r_j^M is the reaction rate.

Rearranging the equations, the mass balance for the gas phase is given by Equation 25.

$$\frac{\partial x_{\alpha}^{(g)}}{\partial t} = -\frac{\partial (x_{\alpha}^{(g)} v^{(g)})}{\partial z} + \frac{(1-\varepsilon)\rho_{\alpha}^{(s)}}{\varepsilon c_t^{(g)}} \eta_{eff} \sum_{j}^{N_R} \nu_{\alpha,j}\, r_j^M \tag{25}$$

Since the Equation 25 is nonlinear and to facilitate the resolution of the equations, for the simulation of the fixed bed reactor, the reactor was divided into perfectly homogeneous segments, with constant pressure, temperature, and concentration, as shown in Figure 3.

Figure 4 depicts the scheme of the two fixed-bed reactors within the Aspen Custom Modeler software. The generic scheme presented in Figure 3 is incorporated into the reactors shown in Figure 4.

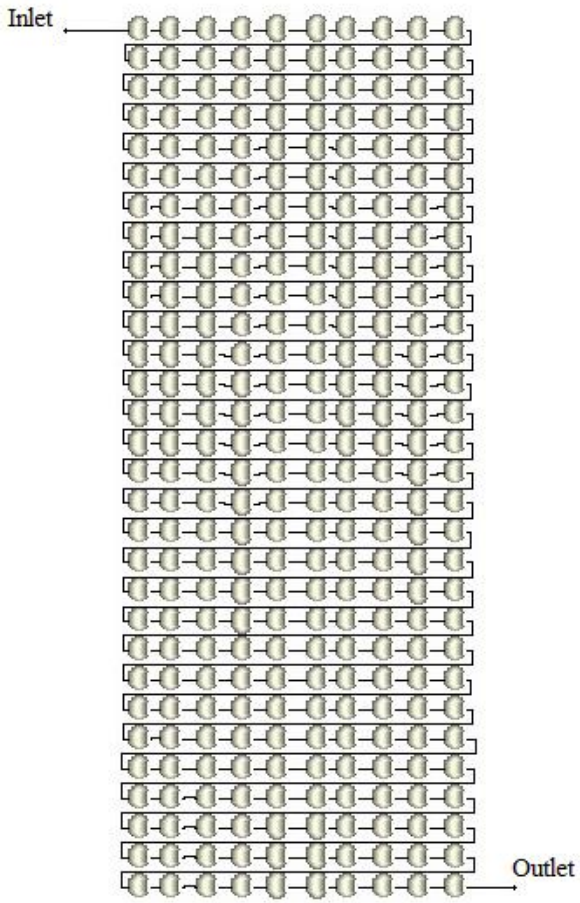

Figure 3 – Generic schematic of a fixed bed reactor divided into parts.

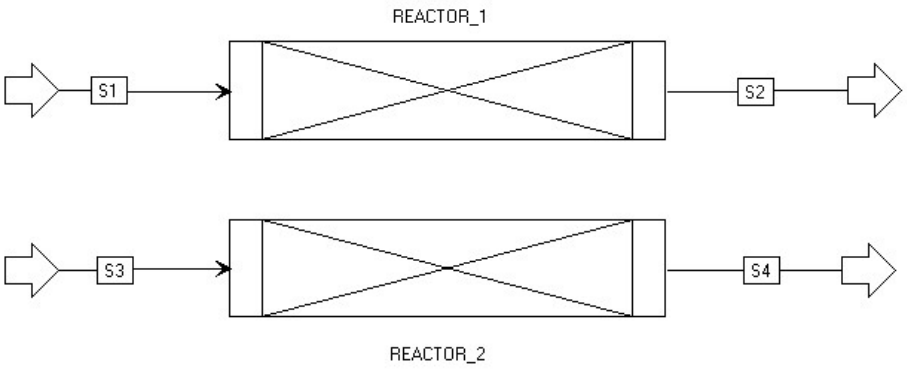

Figure 4 – Schematic of the fixed bed reactors inside the Aspen Custom Modeler.

Figure 3 presents a generic simulation model of the fixed bed reactor divided into segments modeled by Equation 26:

$$\frac{dx_{\alpha\,out}}{dt} = \dot{n}\frac{(x_{\alpha\,int} - x_{\alpha out})}{(V_t \varepsilon c_t^{(g)})} + \frac{(1-\varepsilon)\rho_\alpha^{(s)}}{\varepsilon c_t^{(g)}}\eta_{eff}\sum_j^{N_R} \nu_{\alpha,j}\, r_j^M \tag{26}$$

$$\forall_\propto = (H_2, H_2O, CO_2, CO)$$

Where $x_{\alpha int}$ is the inlet mole fraction of species i, $x_{\alpha out}$ is the outlet mole fraction of species i, $\dot{n}$ is molar flow, and V_t is the volume of the segment.

4.3.1.2 Solid-phase mass balance

For the solid phase, the model is analogous to the gas phase model, also considering a single spatial direction, and it is given by Equation 27.

$$\frac{\partial \rho_\beta^{(s)}}{\partial t} = -\frac{\partial}{\partial z}\left(\rho_\beta^{(s)} v^{(s)} + j_\beta^{(s)}\right) + \sigma_\beta^M \tag{27}$$

Since the catalyst is placed in a fixed position inside the reactor at $v^{(s)} = 0$, the solid phase diffusion term is also neglected (Equation 28).

$$\frac{\partial \rho_\beta^{(s)}}{\partial t} = \sigma_\beta^M \tag{28}$$

Since $\rho_\beta^{(s)}$ is described by Equation 29, the balance can be rewritten as in Equation 30.

$$\rho_\beta^{(s)} = c_t^{(s)} M_\beta x_\beta^{(s)} (1-\varepsilon) \tag{29}$$

$$\frac{\partial}{\partial t}(c_t^{(s)} M_\beta x_\beta^{(s)} (1-\varepsilon)) = \sigma_\beta^M \tag{30}$$

Where M_β, $c_t^{(s)}$ and ε are constants. The term σ_β^M for the solid phase is defined as shown in Equation 31.

$$\sigma_\beta^M = M_\beta \sum_j^{N_R} \nu_{\beta,j}\, r_{j,eff} \tag{31}$$

Rearranging the equation, it gives the mass balance equation for the solid phase (Equation 32).

$$\frac{\partial x_{\beta}^{(s)}}{\partial t} = \frac{(1-\varepsilon)\rho_{\beta}^{(s)}}{(1-\varepsilon)c_t^{(s)}}\eta_{eff}\sum_{j}^{N_R} \nu_{\beta,j} r_j^M = M^{(s)}\eta_{eff}\sum_{j}^{N_R} \nu_{\beta,j}\, r_{j,eff} \qquad (32)$$

$$\forall_{\beta} = (Fe, FeO, FeO_{4/3})$$

Where, $\rho_{\beta}^{(s)}$ is the specific mass, $c_t^{(s)}$ is the molar concentration in the solid phase, β is solid component index and $\nu_{\alpha,j}$ is the stoichiometric coefficient.

4.3.2 Energy balance

The energy balance model was defined using the same approach as a reactor divided into perfectly homogeneous segments with constant concentrations. Thus, the macroscopic energy balance, which applies the concept of energy conservation and considers that the variation of energy within the system is equal to the net exchange of heat and work with the surroundings, added to the net energy transported by the mass flow into the system, is shown in Equation 33.

$$\frac{d(U + E_p + E_c)}{dt} = \dot{n}_{int}\left(U_{int} + E_{p_{int}} + E_{c_{int}}\right) - \dot{n}_{out}\left(U_{out} + E_{p_{out}} + E_{c_{out}}\right) + \dot{Q} + \dot{W} \qquad (33)$$

Where, U is the internal energy, E_p is the potential energy, E_c is the kinetic energy, $\dot{n}$ is the molar flow, $\dot{Q}$ is the heat, $\dot{W}$ is the work, $_{int}$ is the inlet and $_{out}$ is the outlet.

The work in a system, as described by Equation 34, is the sum of two essential components: flow work and shaft work. The flow work is associated with the interactions that occur due to the movement of fluid in and out of the system. This work component reflects the contributions of fluid pressures at the inlet and outlet of the system, as well as the volume involved in this flow. On the other hand, shaft work is related to the interactions of rotating systems such as pumps, compressors and motors. These two working components are essential

to understanding the energy entering or leaving a system and are fundamental in analyzing the energy balance of open systems.

$$\dot{W} = \dot{W}_s + \dot{W}_f \tag{34}$$

Where, $\dot{W}_s$ is the shaft work and $\dot{W}_f$ is the flow work.

The work flow is described by Equation 35:

$$\dot{W}_f = (P_{int}\dot{V}_{int}) - (P_{out}\dot{V}_{out}) = P_{int}V_{int}\dot{n}_{int} - P_{out}V_{out}\dot{n}_{out} \tag{35}$$

Where, P is the pressure and V is the control volume.

Substituting the flow work in Equation 33:

$$\frac{d(U + E_p + E_c)}{dt} = \dot{n}_{int}(U_{int} + E_{p_{int}} + E_{c_{int}}) - \dot{n}_{out}(U_{out} + E + E_{c_{out}}) + \dot{Q} + (\dot{W}_s + P_{int}V_{int}\dot{n}_{int} - P_{out}V_{out}\dot{n}_{out}) \tag{36}$$

Rearranging Equation 36 with Equation 37 one can rewrite it as follows:

$$H = U + PV \tag{37}$$

$$\frac{d(U + E_p + E_c)}{dt} = \dot{n}_{int}(H_{int} + E_{p_{int}} + E_{c_{int}}) - \dot{n}_{out}(H_{out} + E_{p_{out}} + E_{c_{out}}) + \dot{Q} + \dot{W}_s \tag{38}$$

Where, H_{int} and H_{out} are the specific enthalpy entering and leaving the system.

It was considered that the thermal energy is significantly greater than the mechanical energy in the system. Therefore, potential and kinetic energies were disregarded in the analysis. Furthermore, shaft work was excluded from the equation due to the absence of agitation in the reactor. Therefore, the equation can be simplified to give the Equation 39.

$$\frac{dU}{dt} = \sum H\,\dot{n}_{int} - \sum H_{out}\,\dot{n}_{out} + \dot{Q} \tag{39}$$

The total heat in the system is the sum of the heat released or absorbed by the chemical reaction, known as reaction heat, and the heat supplied to heat the reactor. This relationship is represented by Equation 40.

$$\dot{Q} = \dot{Q}_h + \dot{Q}_{rc} \tag{40}$$

Where, $\dot{Q}_h$ is the heat from reactor heating and $\dot{Q}_{rc}$ is the heat of reaction.

The heat of reaction is described by Equation 41.

$$\dot{Q}_{rc} = \Delta H_r n_s r_{j,eff} \tag{41}$$

Where, ΔH_r is the enthalpy of reaction and n_s is the number of moles of solid phase.

When rewriting Equation 39 and substituting the reaction heat in Equation 41, one can further simplify the calculation. Furthermore, by considering that the mass of the solid is significantly greater than the mass of the gas, we can focus our analysis primarily on the solid phase. Therefore, one can replace Equation 42 in Equation 39, mainly taking into account the interactions and transformations that occur within the solid, thus simplifying the assessment of the energy balance in the system.

$$dH = nC_p dT \tag{42}$$

Where, C_p is the heat capacity of metal.

This way we have Equation 43:

$$\sum n_s \dot{C}_p \frac{dT}{dt} = \sum H_{int}\,\dot{n}_{int} - \sum H_{out}\,\dot{n}_{out} + \Delta H_r n_s r_{j,eff} + \dot{Q}_h \tag{43}$$

The enthalpy of formation of the gas phase is an implicit component in the entry and exit enthalpy calculations in the Aspen Plus software, which calculates the enthalpies of streams based on the enthalpy of formation at 25°C and 1 atm. Subsequently, it makes temperature corrections and, after this step, makes additional corrections to the operating pressure by applying the enthalpy departure calculated by an appropriate equation of state.

4.3.3 Pressure drop

Pressure drops through packed beds are the result of frictional losses and inertia characterized by the linear and quadratic dependence of the flow velocity. Thus, for evaluating the head loss in fixed bed reactors, the Ergun equation (Equation 44) was used (ÇARPINLIOĞLU AND ÖZAHI, 2008).

To perform the calculation of Equation 44, the convenience of using the Ergun equation in terms of dimensionless groups was taken into account. Additionally, the assumption of spherical particles in the packed bed was made. These simplifications were implemented for simplicity of the calculations associated with pressure drop analysis.

$$\frac{\Delta P \bar{\rho}_f}{(G)^2}\frac{D_P}{L}\frac{\varepsilon^3}{(1-\varepsilon)} = \frac{150}{Re_{sup}} + 1{,}75 \tag{44}$$

Where, ΔP is the pressure drop in the bed, L is the length of the bed, ε is the void fraction of the bed, D_P is the particle diameter,G is gas flow rate, $\bar{\rho}_f$ is gas density and Re_{sup} is the Superficial Reynolds number.

To calculate the gas flow rate and Superficial Reynolds number, equations 45 and 46 were utilized.

$$G = \bar{\rho}_f \bar{v} = \frac{\dot{m}}{A} \tag{45}$$

Where, $\dot{m}$ mass flow rate of the fluid and A is flow area.

$$Re_{sup} = \frac{D_p G}{(1-\varepsilon)\mu} \tag{46}$$

Where, μ is fluid viscosity.

To perform the calculation using the Ergun equation, an iterative method was employed to calculate the average fluid density, which is a function of the average pressure. This iterative method allowed for obtaining a more accurate estimate of the average fluid density, taking into account the variations in pressure along the packed bed. With the average density determined, it was possible to proceed with the calculation of the pressure drop using the Ergun equation and obtain more reliable results for the system analysis.

To solve the reactor model, it was necessary to employ an integration method for solving DAEs (Differential Algebraic Equations) and an algebraic equation solver. The default approach of the software, a combination of implicit Euler method along with mixed Newton iteration, was selected for this purpose.

4.4 Environmental assessment

Indirect CO_2 emissions from the use of utilities were considered to assess the global warming potential (GWP) of the proposed RWGS-CL plant. The utilities considered were electricity, natural gas, and cooling water. Complete details can be seen in Table 1.

Table 2. Details of the utilities used in the simulation.

Utility	Cost ($/GJ)	Ref	CO_2-eq emission (kg/GJ)	Ref.
Usual electricity	14.22	(ANEEL, 2022)	11.83	(MCTI, 2022)
Natural gas	2.08	(EIA, 2022)	55.93	(ANP, 2022)
Cooling water	0.78	(TURTON et al., 2018)	-	

The Global Warming Potential (GWP) is a metric that quantifies the overall effect of a process on the atmosphere's heat radiation absorption due to emissions of greenhouse gases from the network. The GWP is given by Equation 47.

$$GWL = \frac{CO_{2-eq}}{SG} * 100\% \quad (47)$$

Where $CO_{2\text{-}eq}$ is the direct and indirect emissions of CO_2 equivalent (kg), and SG is the synthesis gas produced (kg).

Direct and indirect CO_2 emissions in chemical processes have distinct meanings. Direct emissions refer to the direct release of carbon dioxide into the atmosphere as a result of the chemical reactions that occur in the process. This occurs when CO_2 is produced as a byproduct of the intrinsic chemical reactions inherent to the operation of the process, often in an unavoidable manner.

On the other hand, indirect CO_2 emissions are those that are not directly linked to chemical reactions but are a consequence of operations associated with the process, such as the use of energy for heating, cooling, or material handling. This includes the combustion of fossil fuels to provide thermal or electrical energy for the process, resulting in the release of CO_2 into the atmosphere as an indirect byproduct.

Therefore, direct emissions are related to intrinsic chemical reactions, while indirect emissions are linked to operations and the consumption of energy required for the operation of the chemical process. Both forms of emissions are important considerations in terms of assessing and reducing the carbon footprints associated with chemical processes.

4.5 Economic assessment

To evaluate the profitability of the process and perform a cash flow analysis, the methodology described in Turton et al. (2018) was used. The evaluation required data on several economic indicators, such as fixed capital investment (FCI) represented by Equation 48, cost of manufacturing (COM) presented in Equation 49, revenue from sales, raw material expenses, working capital, depreciation, discount rates, taxes, and operating expenses. The equipment sizing was based on the Aspen Process Economic Analyzer (APEA).

$$FCI = 1.18 \sum_{i=1}^{n} C_{BM,i} + 0.5 \sum_{i=1}^{n} C^{0}{}_{BM,i} \quad (48)$$

$$COM = f_1 FCI + f_2 C_{OL} + f_3 (C_{UT} + C_{WT} + C_{RM}) \quad (49)$$

where $C_{BM,i}$ is the base module cost for equipment i, $C^0_{BM,i}$ is the base price of equipment i; C_{OL} is the cost of operating labor; C_{UT} is the cost of utilities; C_{WT} is the cost of waste treatment; C_{RM} is the cost of raw materials; and f_1, f_2, and f_3 are multiplicative factors.

Turton et al. (2018) stated that the multiplicative factors for f_1, f_2, and f_3 are 0.18, 2.27, and 1.23, respectively. However, due to the high capital intensity associated with the processes being considered, there is a concern that the calculated operating cost using Equation 49 might be overestimated. Therefore, new multiplicative factors of 0.03, 0, and 1 were applied to f_1, f_2, and f_3, respectively. This revised approach considers operational costs, such as labor, supervision, maintenance, materials, taxes, among others, as a fraction of the fixed investment. This approach is common in the literature and helps refine operational cost estimates, taking into account the capital-intensive nature of these processes (CHRISTENSEN, 2020). This revised approach assigns the first term of Equation 49, f_1FCI, to represent operational costs such as operating labor, direct supervisory and clerical labor, maintenance and repairs, operating supplies, laboratory expenses, patents and royalties, local taxes and insurance, plant overhead costs, administration costs, distribution and selling costs, and research and development. Similar methodologies have been documented in the literature, where operating costs are determined as a fraction of fixed investment plus costs associated with utilities, raw materials, and waste treatment (CHRISTENSEN, 2020).

This study focused on the RWGS-CL process. However, it should be noted that the cost of CO_2 as a raw material was not taken into account in this research. The prices of all other raw materials and products involved in the process are presented in Table 2.

Table 3. Price for raw materials and products.

Component	Cost	Classification	Ref.
Carbon dioxide	-	Raw material	-
Water	0.177 $/tonne	Product	(TURTON et al., 2018)
Hydrogen	3.7 $/kg	Raw material	(MORGAN, 2023)
Carbon monoxide	0.06 $/kg	Product	(JIAO; LUC AND JOUNY, 2018)

For the RWGS-CL plant, a cash flow analysis was conducted after collecting all the relevant data, using the CAPCOST v.2017 software (TURTON et al., 2018). The capital cost was adjusted using the cost indices for 2022 (CHEMENGONLINE, 2023) and accounting for the plant being built in Brazil with a factor of 1.4 (GRACIANO et al., 2018). The cash flow after taxes was calculated for a project life of 15 years after startup. The fixed capital investment (FCI) was distributed over a construction period of 2 years using distribution factors of 60% and 40%, respectively. The Brazilian tax rate and annual interest rate used were 34% and 10%, respectively. The capital depreciation was calculated using the straight-line method with a period of 10 years.

The relevant economic indicators selected were the net present value (NPV) and return on investment (ROI), shown in Equations 50 and 51. NPV represents the sum of annual cash flows adjusted by the discount rate, brought to time zero. A positive NPV indicates a profitable project. ROI, on the other hand, represents the annual rate of return on invested capital. It is the rate that adjusts the annual cash flow to zero its sum. An ROI greater than the cost of capital (discount rate) indicates a profitable project.

$$NPV = \frac{Cash\ flow}{(1+i)^t} \tag{50}$$

$$ROI = \frac{Total\ benefits - Total\ costs}{Total\ costs} \tag{51}$$

Where i is the required return or discount rate; and t is the number of periods.

5 RESULTS AND DISCUSSIONS

5.1 THERMODYNAMIC ANALYSIS

Nine different metal oxides were chosen from the literature as potential oxygen carriers, Fe_3O_4, FeO, NiO, CoO, ZnO, SnO, Cu_2O, Mn_3O_4 and CeO_2, for evaluation by thermodynamic analysis in order to find out which one provides the greatest CO_2 conversion (WENZEL, 2018). In the Appendix A it is possible to see the thermodynamic analysis of all the metals evaluated.

Figure 5 presents the thermodynamic analysis of magnetite (chosen metal) in the oxidation reaction using magnetite. Note that the feed molar ratio does not interfere with the CO_2 conversion (%). It is observed that with increasing temperature the tendency of CO_2 conversion (%) is to increase, reaching its highest conversion at 55%.

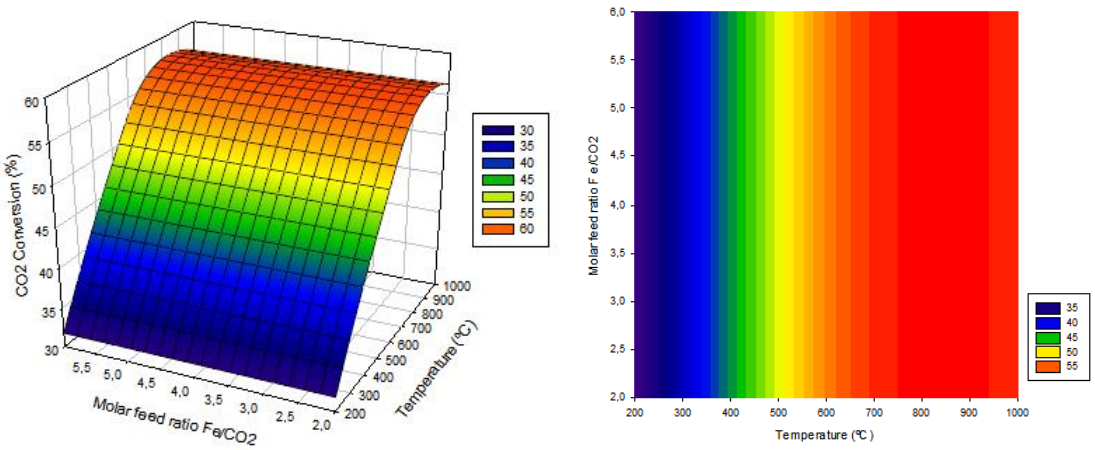

Figure 5- Thermodynamic analysis of the oxidation reaction using Fe_3O_4.

Figure 6 shows that only the increase in temperature influences the increase in the conversion of hydrogen gas (H_2) in the reduction reaction, reaching its highest conversion at 60%. From Figures 5 and 6, it was possible to observe that the temperatures that present the best conversion of the gases, for the oxidation reactions, are 700°C and 1000°C, respectively.

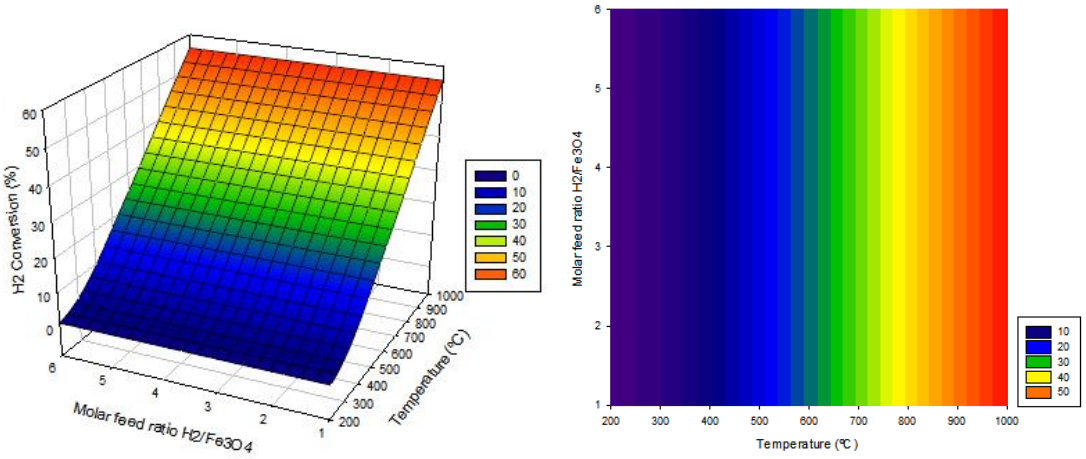

Figure 6- Thermodynamic analysis of the reduction reaction using Fe_3O_4.

Wenzel (2018) evaluated the same metals of this work, but his analysis only considered the influence of temperature and Gibbs energy of the reaction on the conversion of CO_2 and H_2. In his analysis, a minimum value of 20% conversion of both reagents was arbitrated, i.e., for a metal to be considered suitable for RWGS-CL, it would have to have at least 20% conversion in each reaction. From literature review, iron oxides are shown as best metals due to their high conversions, which is a positive result from the economical point of view, since Brazil has many sources of iron, and it has an attractive cost.

The maximum conversion for each metal evaluated in this work has not been reported in the literature. Additionally, there is no reported investigation on how the feed molar ratio and temperature affect the conversions of CO_2 and H_2. Such an analysis is important from the industrial point of view, since later other process steps will be integrated into the reactor to produce synthesis gas, such as, for example, the integration of oxidation and reduction reactors, the product separation steps and the Fischer-Tropsch synthesis, which need to operate under similar conditions for the energy efficiency of the process.

5.2 FIXED BED REACTOR MODELING AND SIMULATION

5.2.1 Testing and evaluating the model

As previously explained, to easily handle the model in ASPEN Custom Modeler, a simple discretization of the mass balance equation was considered (see Equations 26 and 32), where the multitubular reactor was divided into segments. Each segment along the reactor length is uniform where pressure, temperature and concentration are considered constant.

Initially, the oxidation and reduction reactor tubes were divided into 300 segments of 0.04 m, corresponding to 12m of reactor, and each one was described by the model given in Equation 26 for the gas phase and in Equation 32 for the solid phase. In this study, simulations were carried out considering three different inlet flow rates of reagents, in the fixed bed reactors, for the RWGS-CL reaction. These flows represent low residence times, a condition that favors higher conversions. The evaluated flow rates were 0.5 kmol/h, 1 kmol/h, and 1.5 kmol/h, for both the oxidation and reduction stages.

During the investigation, it became evident that the increase in residence time had a positive impact on the reaction efficiency, resulting in higher product yields. Based on this finding, it was decided to employ a reactor length of 12 meters and 4 inch diameter, which would provide a greater extended residence time for the reactants and, consequently, optimize the conversion to the desired products. Additionally, the choice of relatively low flow rates aimed to promote a more effective interaction of the reactants with the oxygen carrier material, aiming to enhance the overall performance of the process. The obtained results were of great relevance for understanding the kinetic behavior and for the improvement of RWGS-CL as a potential route for carbon monoxide production.

Figures 7, 8 and 9 provide a representation of the behavior of the conversion of reactants into products over time, at the end of 12 meters of reactor.

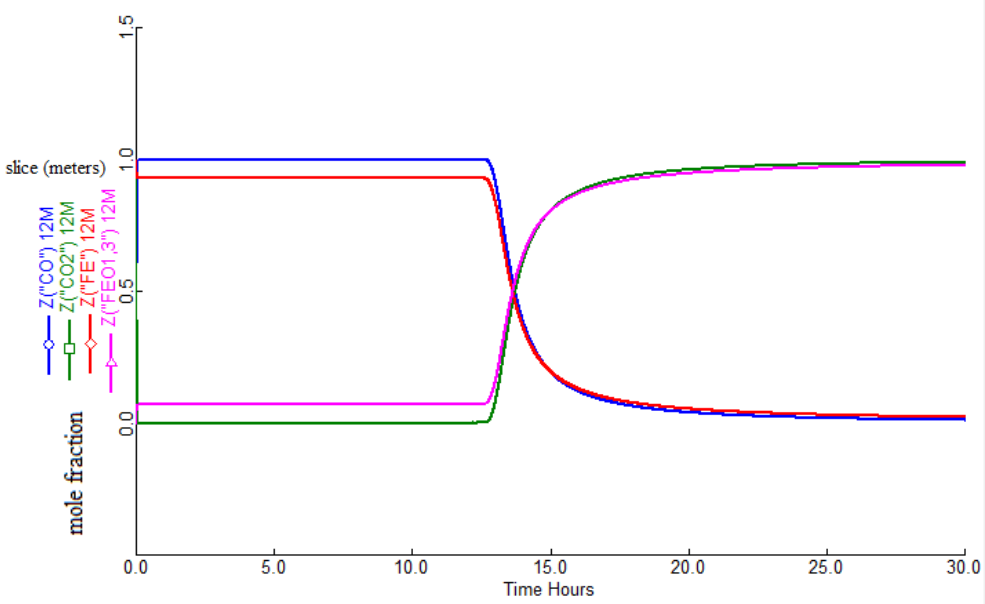

Figure 7 - Conversion of CO_2 to CO and Fe to magnetite at the end of 12 meters of reactor with a feed flow rate of 0.5 kmol/h (oxidation step).

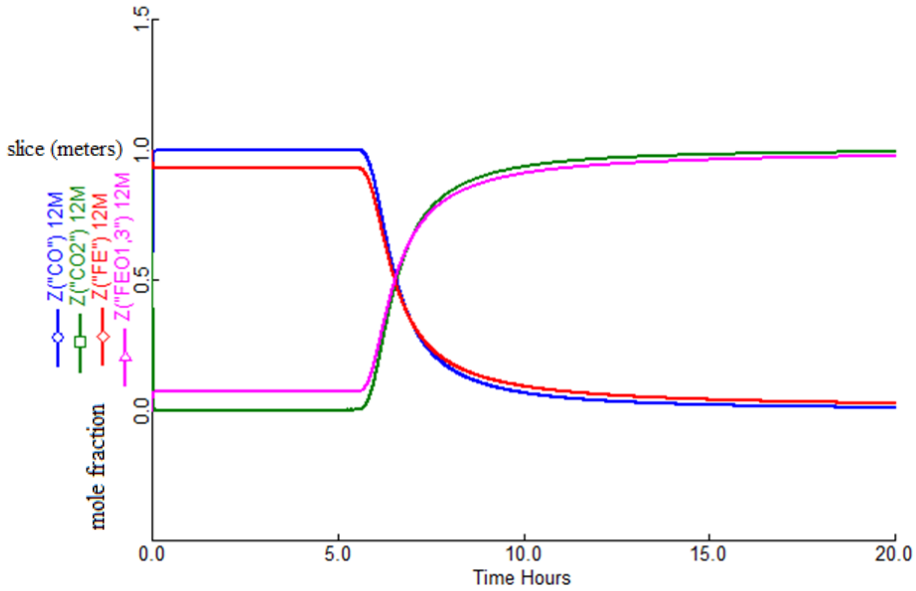

Figure 8 - Conversion of CO_2 to CO and Fe to magnetite at the end of 12 meters of reactor with a feed flow rate of 1 kmol/h (oxidation step).

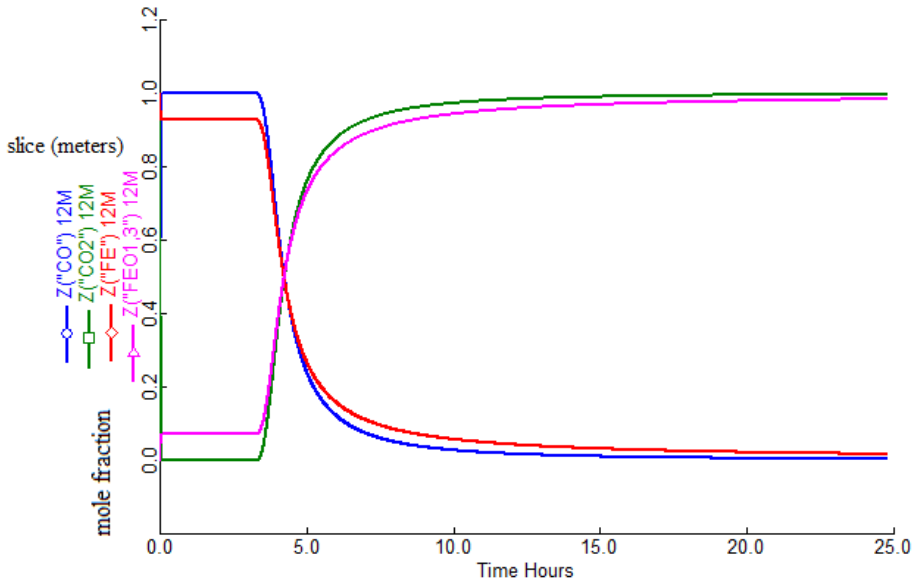

Figure 9 - Conversion of CO_2 to CO and Fe to magnetite at the end of 12 meters of reactor with a feed flow rate of 1.5 kmol/h (oxidation step).

Based on figures 7, 8, and 9, it is evident that the lower the inlet flow rate of CO_2 into the reactor, the higher the percentage of CO completely converted at the reactor outlet.

Additionally, it can be seen that there is less iron converted into magnetite at the end of the reactor, as most of the CO_2 reacts with the iron along the reactor length. Iron is only

converted to 100% magnetite at the end of the reactor after it has been completely converted in the previous segments of the reactor.

Figures 10 and 11 depict the reaction behavior between the gas and the solid along the length of the reactor.

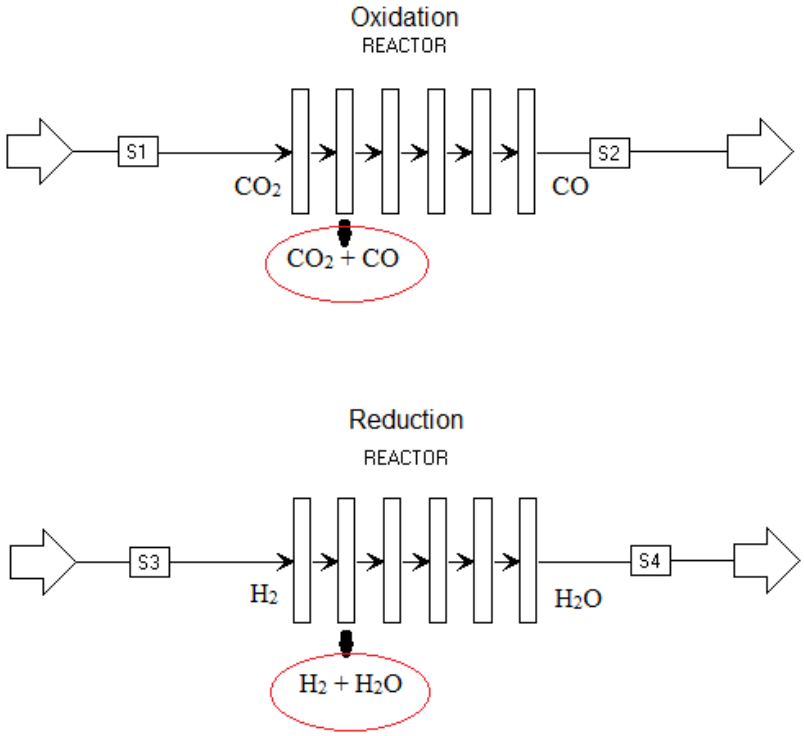

Figure 10 - Behavior of the gases in each segment of the reactor

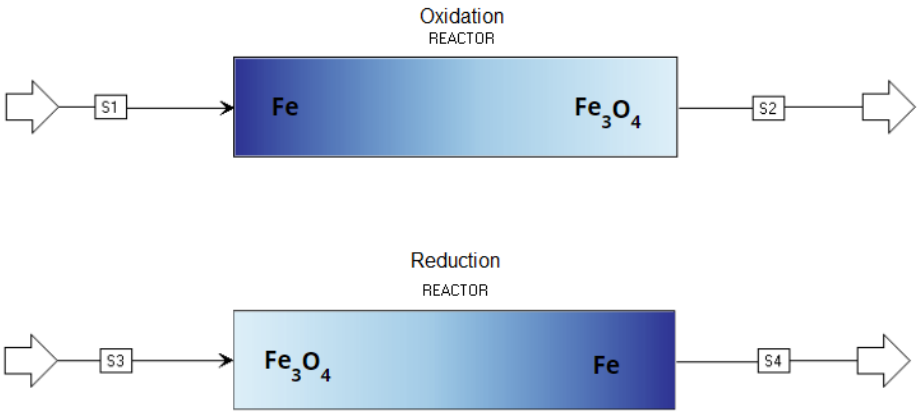

Figure 11 - Solid behavior along the length of the reactor

Figure 10 shows that as the reactor is fed with reactants, less CO_2 is carried from one reactor slice to the next, resulting in a gradual decrease in CO_2 concentration along each reactor

slice. Consequently, each section of the reactor contains a lower amount of available CO_2 to react with iron, leading to a reduction in CO_2 input in each slice and, consequently, an increase in the amount of CO present along the reactor length, reaching 100% CO at 12 meters. Therefore, along the reactor length, less iron will be converted into magnetite, as shown in Figure 11, highlighting the influence of the reaction profile on the conversion of reactants throughout the reactor bed.

This behavior significantly influences the reaction temperature because the oxidation reaction is endothermic and requires heat to occur (WENZEL, 2018). To initiate the reaction, the reactor needs to be heated to a temperature of 1073K. As the reactants pass through the reactor and interact with the solid, the temperature decreases in each slice as the reaction proceeds. This temperature drop pattern is more pronounced at lower feed rates, as illustrated in Figures 12, 13, and 14. It can be observed that at higher feed rates, the residence time in the reactor is reduced, resulting in a faster decrease in temperature along the length of the reactor.

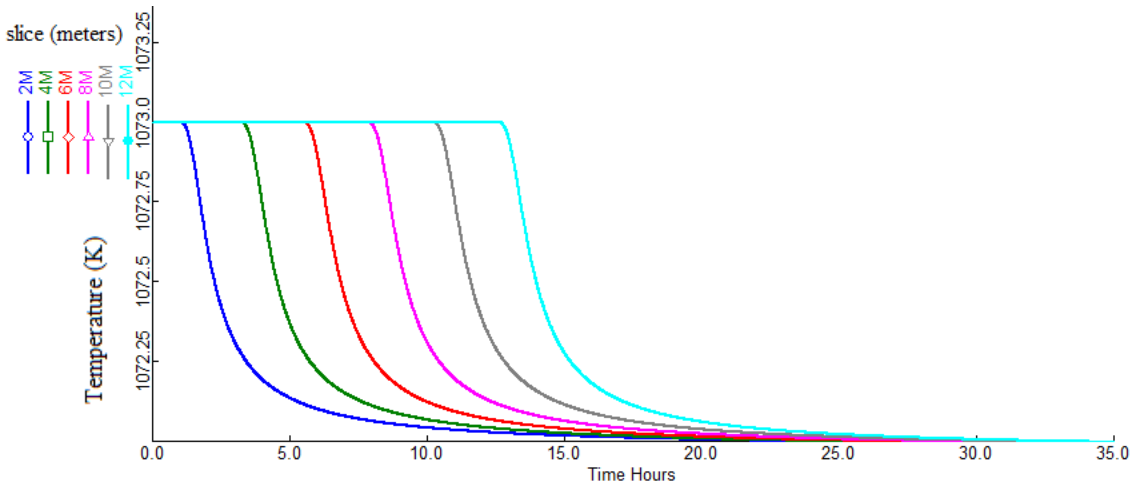

Figure 12 - Temperature profile of the reactor in slices of 2, 4, 6, 8, 10 and 12 meters for a feed flow rate of 0.5 kmol/h (oxidation step).

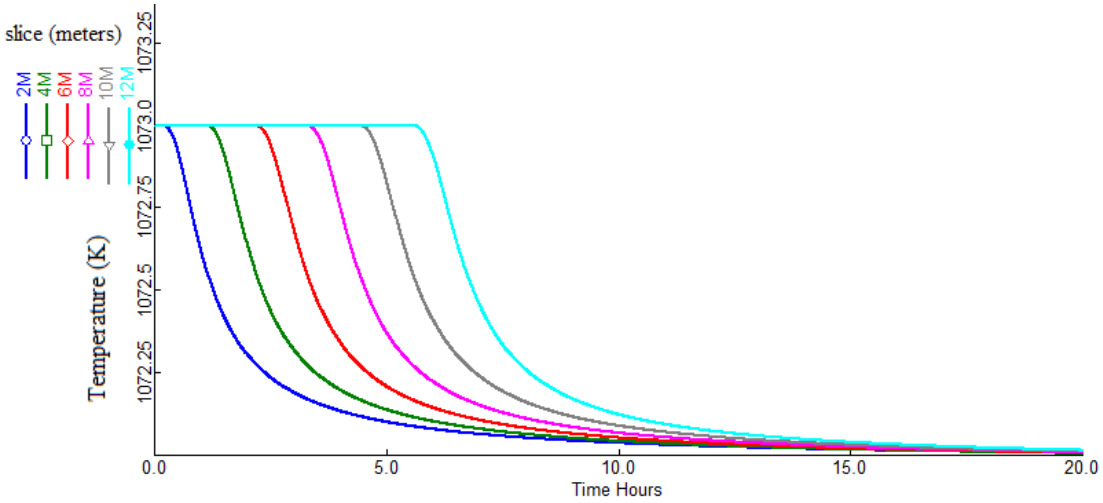

Figure 13 - Temperature profile of the reactor in slices of 2, 4, 6, 8, 10 and 12 meters for a feed flow rate of 1 kmol/h (oxidation step).

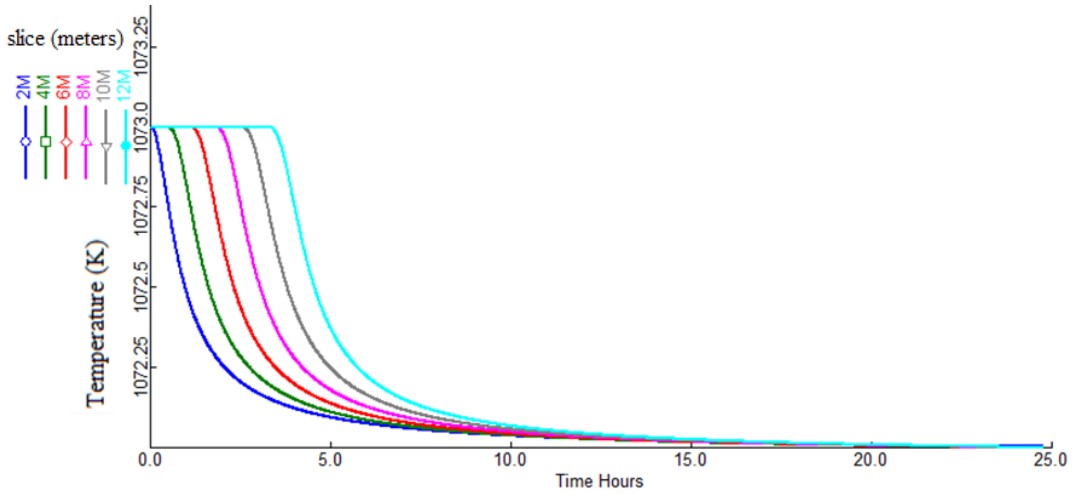

Figure 14 - Temperature profile of the reactor in slices of 2, 4, 6, 8, 10 and 12 meters for a feed flow rate of 1.5 kmol/h (oxidation step).

For all three evaluated flow rates, the reactor was preheated to a temperature of 1073K. A common method to achieve this temperature is the bed heating approach, using nitrogen as the medium. After the heating process, the oxidation step is initiated. This strategy is widely employed in the industry for heating catalytic reactors due to its effectiveness and precise temperature control.

Figures 15, 16, and 17 play a pivotal role in comprehending the pressure drop profile across each segment of the reactor over time, for flow rates of 0.5 kmol/h, 1 kmol/h and 1.5 kmol/h, respectively. These figures provide invaluable insights into the behavior of pressure

drop under low-flow conditions. It is noteworthy that, owing to diminished flow rates, the pressure drop does not exhibit significant changes. Nevertheless, along the reactor length and increasing feed flow rate, the pressure drop exhibits a gradual and anticipated increment. This observed trend aligns harmoniously with theoretical expectations and contributes substantively to understand the fluid-dynamic dynamics within the reactor.

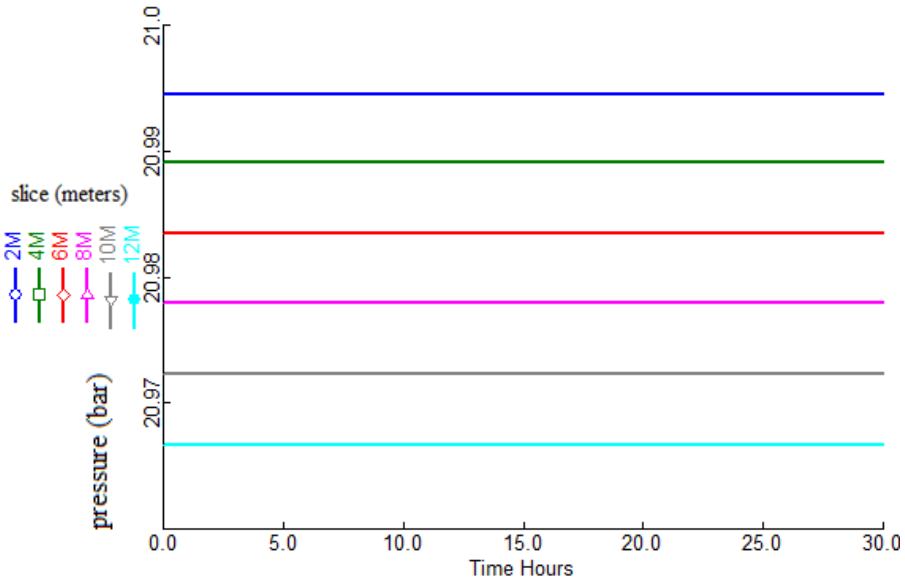

Figure 15 - Pressure (bar) over 12 meters of reactor in 30 hours for a feed of 0.5 kmol/h (oxidation step).

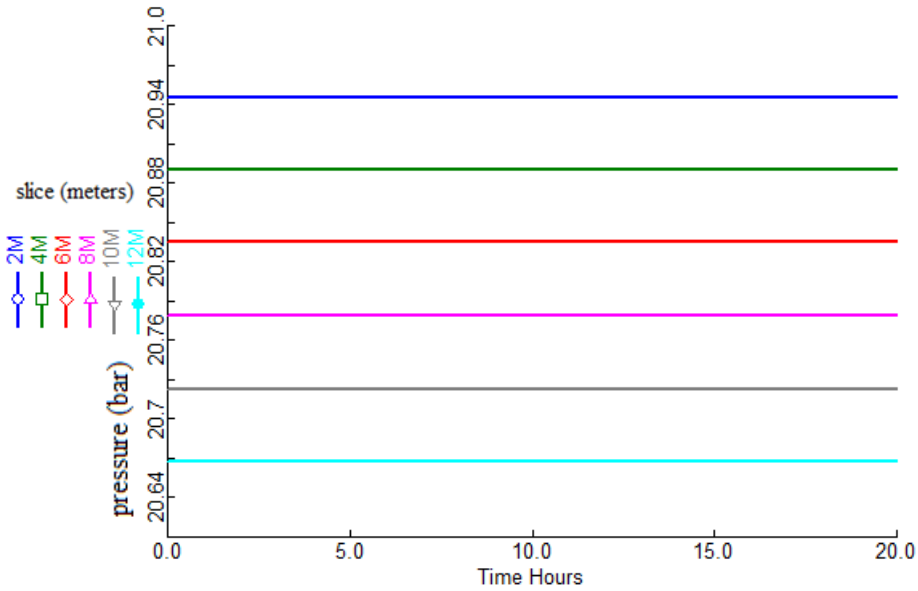

Figure 16 - Pressure (bar) over 12 meters of reactor in 20 hours for a feed of 1 kmol/h (oxidation step).

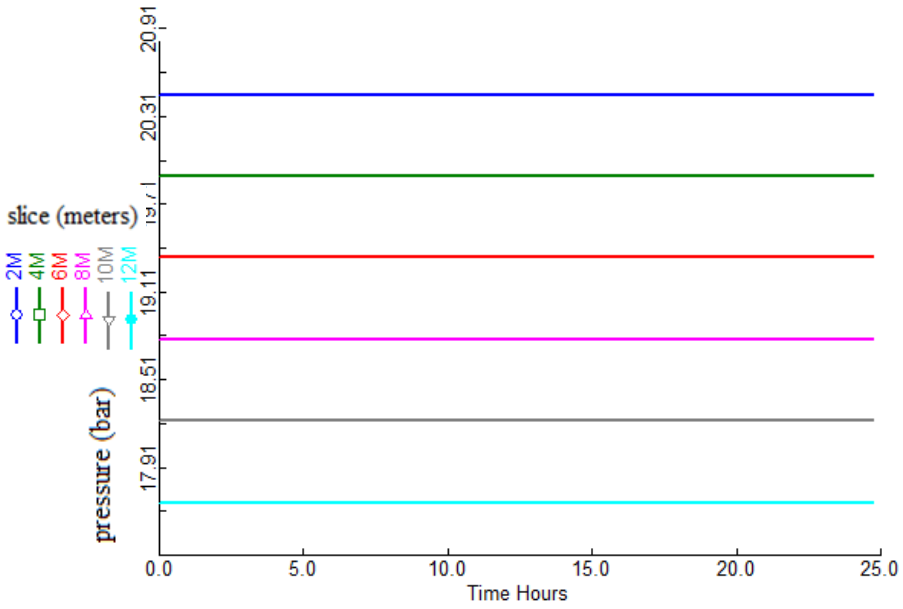

Figure 17 - Pressure (bar) over 12 meters of reactor in 20 hours for a feed of 1.5 kmol/h (oxidation step).

From Figure 10, it is evident that during the reduction step, similar to oxidation, the reaction occurs in such a way that, as the reactor is filled with reactants, there is a decrease in the transport of H_2 from one segment of the reactor to the next, resulting in a gradual decline in H_2 concentration in each segment of the reactor. Consequently, each reactor section has a smaller amount of H_2 available to interact with magnetite, leading to a reduction in H_2 input per slice, thereby resulting in an elevation in the quantity of H_2O present along the reactor's length, reaching 100% H_2O at 12 meters as depicted in Figures 18, 19, and 20. Consequently, along the reactor's length, lesser magnetite undergoes conversion to iron, highlighting the influence of the reaction profile on reactant conversion along the reactor bed.

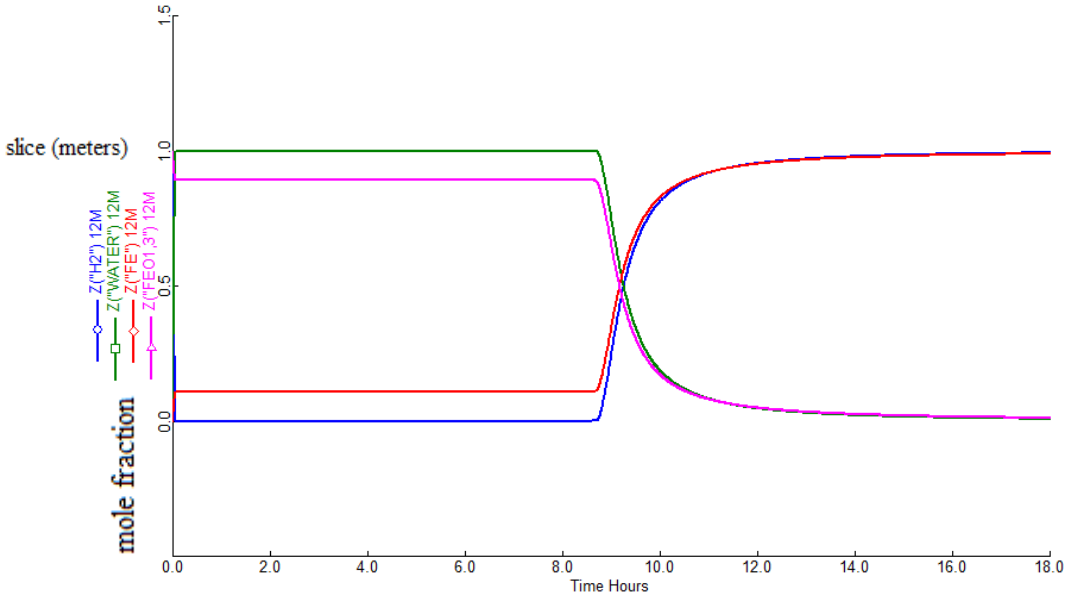

Figure 18 - Conversion of H_2 to H_2O and magnetite to Fe at the end of 12 meters of reactor with a feed flow rate of 0.5 kmol/h (reduction step).

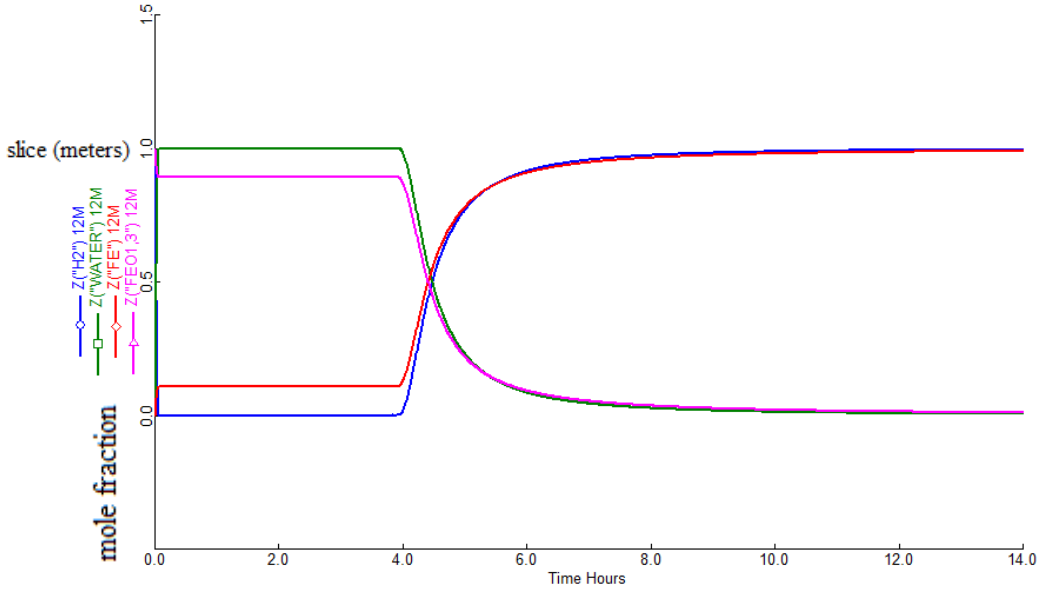

Figure 19 - Conversion of H_2 to H_2O and magnetite to Fe at the end of 12 meters of reactor with a feed flow rate of 1 kmol/h (reduction step).

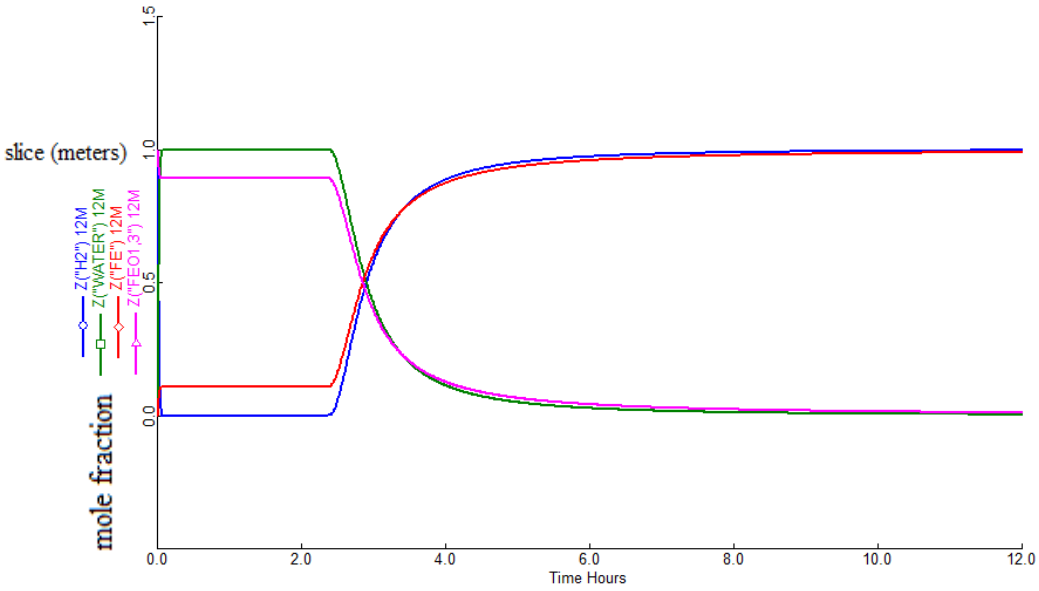

Figure 20 - Conversion of H_2 to H_2O and magnetite to Fe at the end of 12 meters of reactor with a feed flow rate of 1.5 kmol/h (reduction step).

Figures 21, 22, and 23 depict the temperature profile for the reduction reaction at flow rates of 0.5 kmol/h, 1 kmol/h, and 1.5 kmol/h, respectively. To initiate the reaction, the reactor must be heated to a temperature of 1073K. As the reactants pass through the reactor and interact with the solid, the temperature rises in each section as the reaction progresses. This pattern of temperature increase is more pronounced at lower feed rates. It is observed that at higher feed rates, the residence time in the reactor is reduced, resulting in a more rapid temperature increase along the reactor's length. Based on the obtained results, it is evident that the reduction reaction releases a relatively small amount of energy, leading to a modest temperature increase in the reactor. For reactor heating, the same approach suggested for the oxidation reaction can be employed, which involves bed heating through the use of nitrogen. This strategy is commonly employed in the industry for heating catalytic reactors.

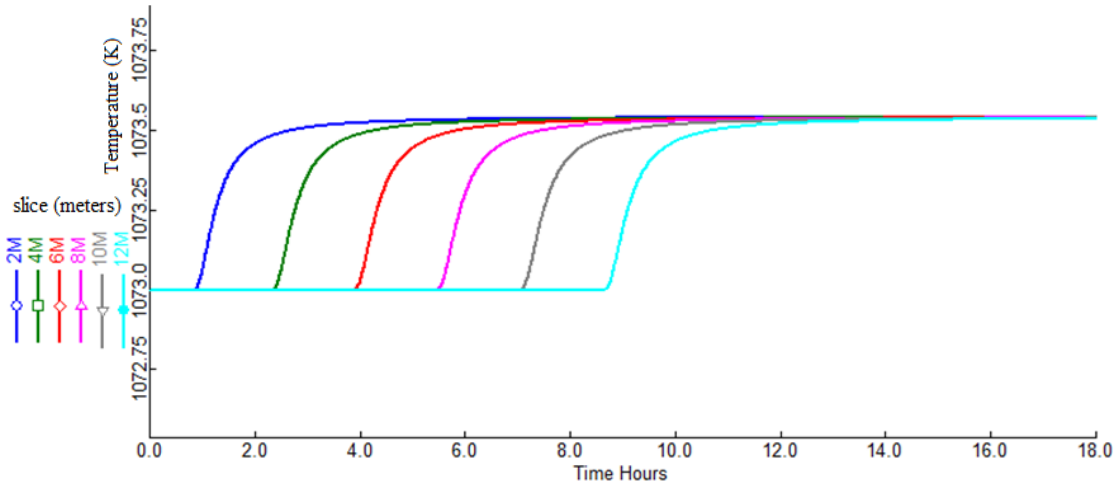

Figure 21 - Temperature profile of the reactor in slices of 2, 4, 6, 8, 10 and 12 meters for a feed flow rate of 0.5 kmol/h (reduction step).

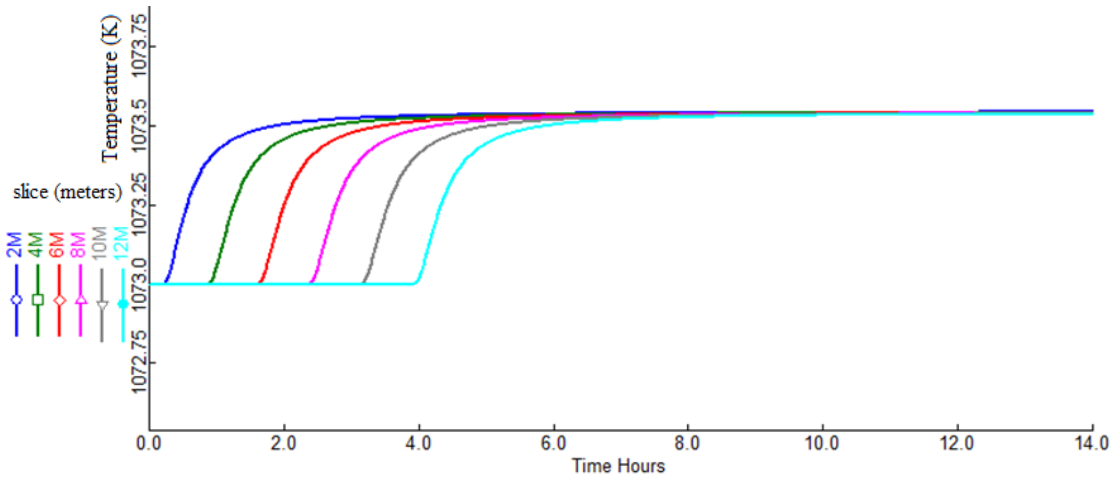

Figure 22 - Temperature profile of the reactor in slices of 2, 4, 6, 8, 10 and 12 meters for a feed flow rate of 1 kmol/h (reduction step).

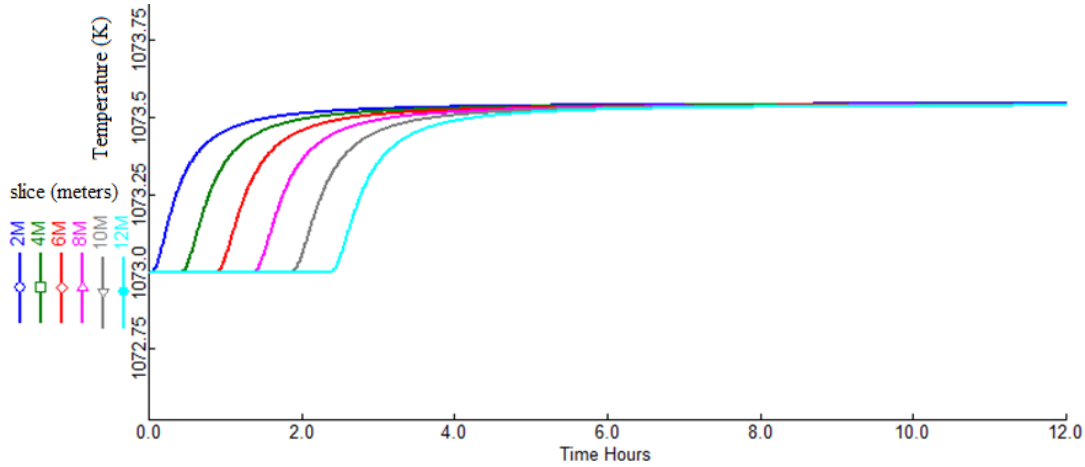

Figure 23 - Temperature profile of the reactor in slices of 2, 4, 6, 8, 10 and 12 meters for a feed flow rate of 1.5 kmol/h (reduction step).

Figures 24, 25, and 26 play a pivotal role in comprehending the pressure drop profile across each segment of the reactor over time, for flow rates of 0.5 kmol/h, 1 kmol/h and 1.5 kmol/h, respectively. These figures provide invaluable insights into the pressure drop behavior in the reduction reaction, indicating the pressure at the reactor outlet.

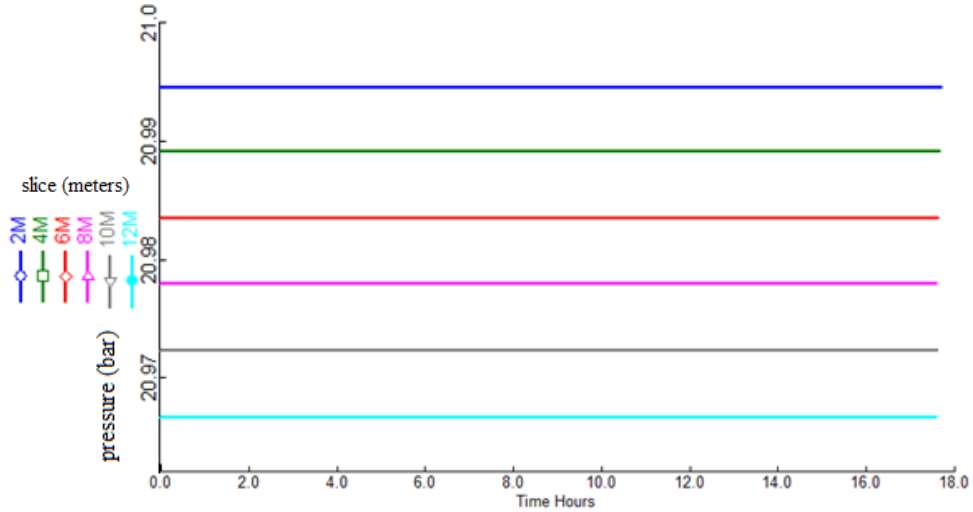

Figure 24 - Pressure (bar) over 12 meters of reactor in 18 hours for a feed of 0.5 kmol/h (reduction step).

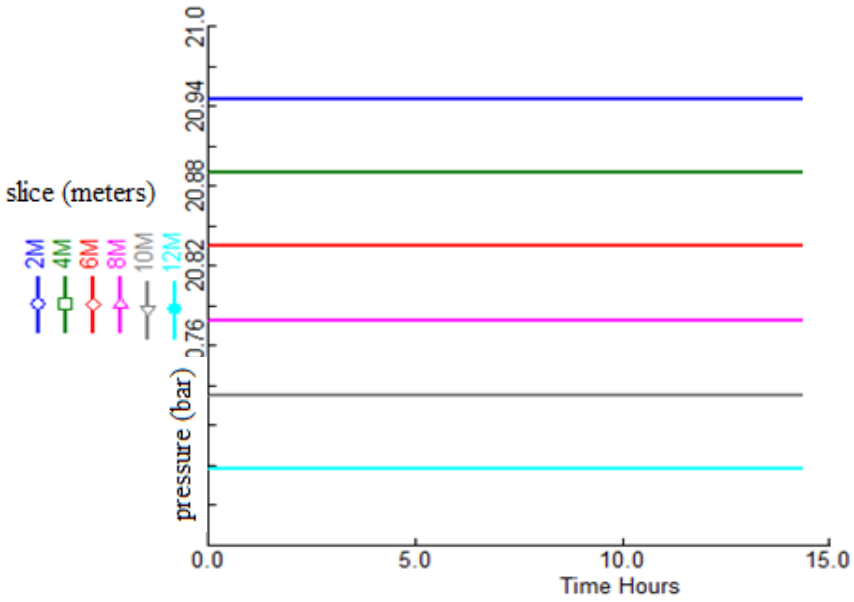

Figure 25 - Pressure (bar) over 12 meters of reactor in 15 hours for a feed of 1 kmol/h (reduction step).

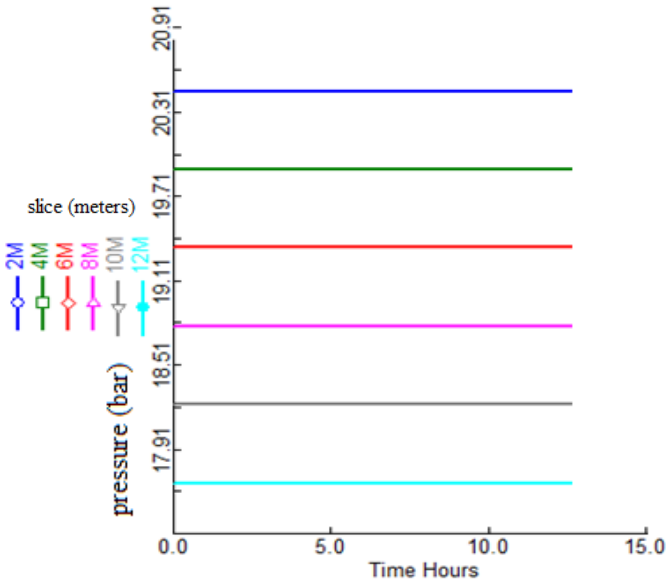

Figure 26 - Pressure (bar) over 12 meters of reactor in 12 hours for a feed of 1.5 kmol/h (reduction step).

In conclusion, when analyzing the numbers related to oxidation and reduction reactions, it becomes evident that achieving 100% conversion at the product output requires a slightly longer residence time for the reduction reaction compared to the oxidation. The temperature variations along the reactor are relatively small. However, it is important to note that while the oxidation reaction absorbs a small amount of heat, the reduction reaction, on the other hand, releases a small amount of heat. These pivotal insights into the reaction characteristics hold

utmost importance in determining the entry conditions into the reactors, particularly when operating within a chemical looping system. Understanding these patterns of behavior is fundamental to optimize and effectively control the reaction processes, ensuring an ideal and efficient performance of the reactors in semi-continuous operation.

5.2.2 Simulating Chemical Looping

To carry out the looping process effectively, it is crucial that both reactions occur simultaneously. Therefore, the optimal feed flow rate for the oxidation and reduction reactions was determined. Building upon the assessment conducted in the previous section, it was noted that a feed flow rate of 0.5 kmol/h (per tube) maintained a 100% conversion of CO_2 to CO for an extended period. Considering the objective of CO production, the feed flow rate for the reduction reactor was adjusted to ensure a simultaneous 100% conversion of H_2 to H_2O, aligned with the occurrence of the oxidation reaction. With this, the feed flow of H_2 was adjusted to 0.4 kmol/h (per tube).

Figures 27, 28, and 29 depict the outcomes of these considerations for the oxidation reaction. It is noteworthy that the reaction occurs over a span of 11-hours, showcasing a consistent 100% product yield.

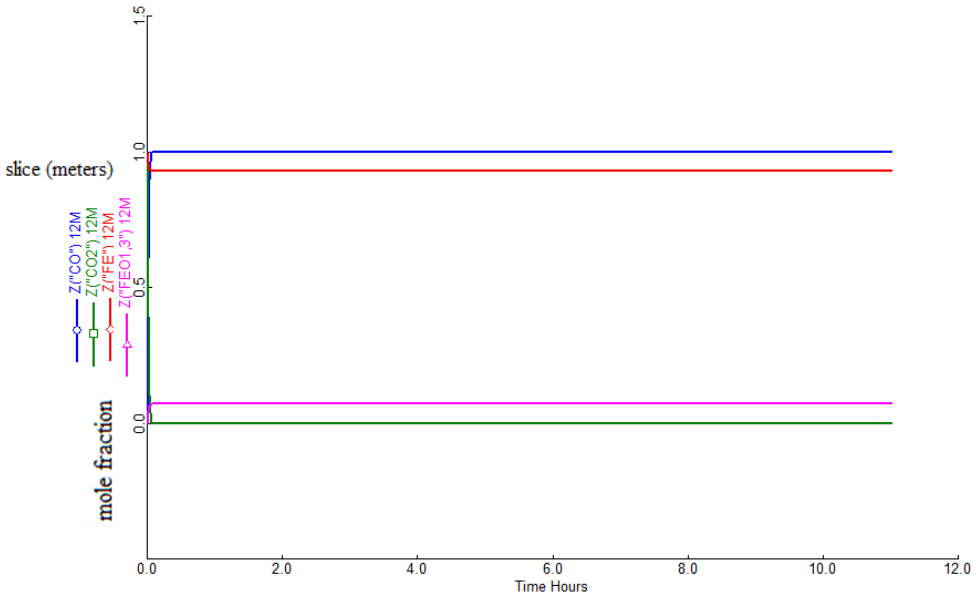

Figure 27 - Conversion of CO_2 to CO and Fe to magnetite at the end of 12 meters of reactor with a feed flow rate of 0.5 kmol/h (oxidation step).

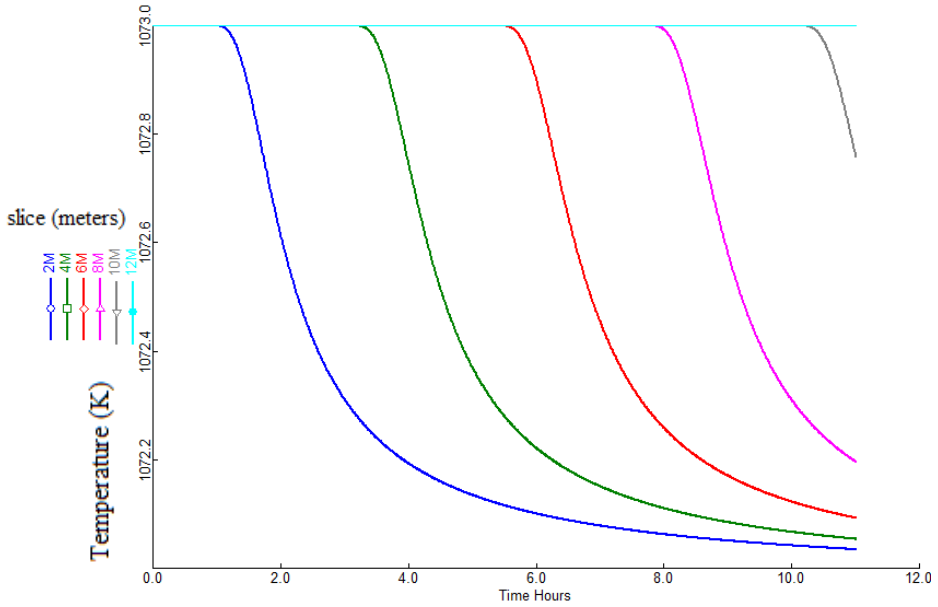

Figure 28 - Temperature profile of the reactor in slices of 2, 4, 6, 8, 10 and 12 meters for a feed flow rate of 0.5 kmol/h (oxidation step).

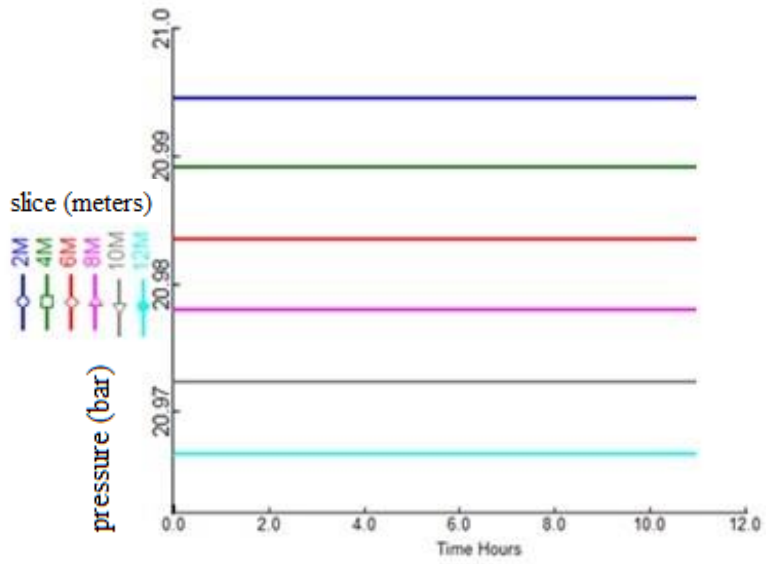

Figure 29 - Pressure (bar) over 12 meters of reactor in 11 hours for a feed of 0.5 kmol/h (oxidation step).

Figure 27 shows that, up to 11 hours of reaction, there is complete conversion of reactants into products. However, the same figure shows that, in the last 12 meters of the reactor, the conversion of iron into magnetite is low. Figure 28 illustrates a slight decline in the reactor's temperature as the reaction progresses in each section. In this figure, it is observed that, at the end of the 11-hour reaction, the reactor maintains a temperature of 1072 K at 2 meters and 1073

K at 12 meters. This is due to the low conversion of solids at the end of the reactor. Lastly, Figure 29 depicts the pressure drop in the reactor, which is minimal, indicating that the 21 bar gas inlet is sufficient for reactor feed.

Figures 30, 31, and 32 show the outcomes of the considerations for the reduction reaction. It is observed that the reaction takes place over a 11-hour duration, demonstrating a consistent 100% product yield.

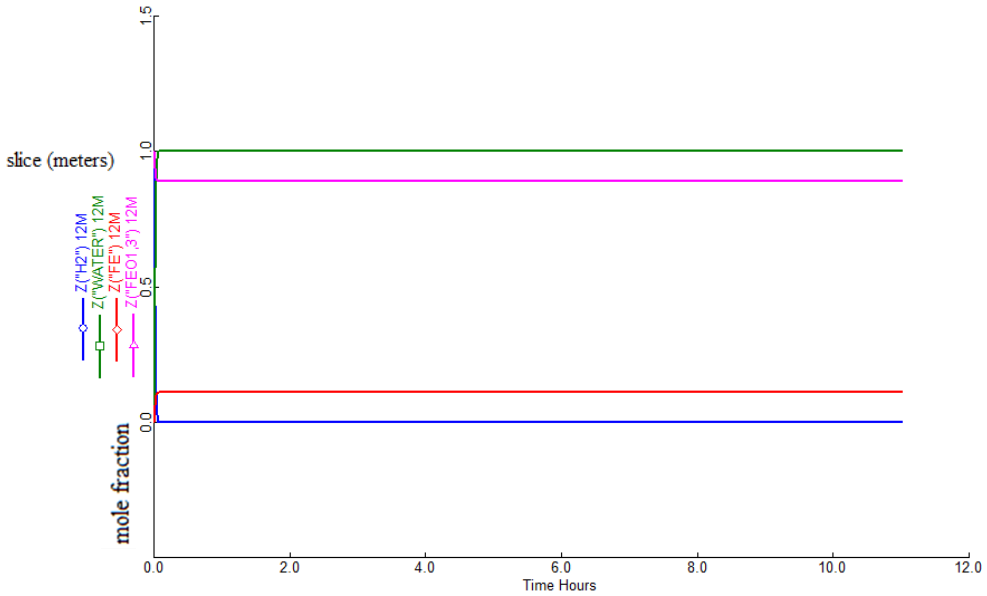

Figure 30 - Conversion of H_2 to H_2O and magnetite to Fe at the end of 12 meters of reactor with a feed flow rate of 0.4 kmol/h (reduction step).

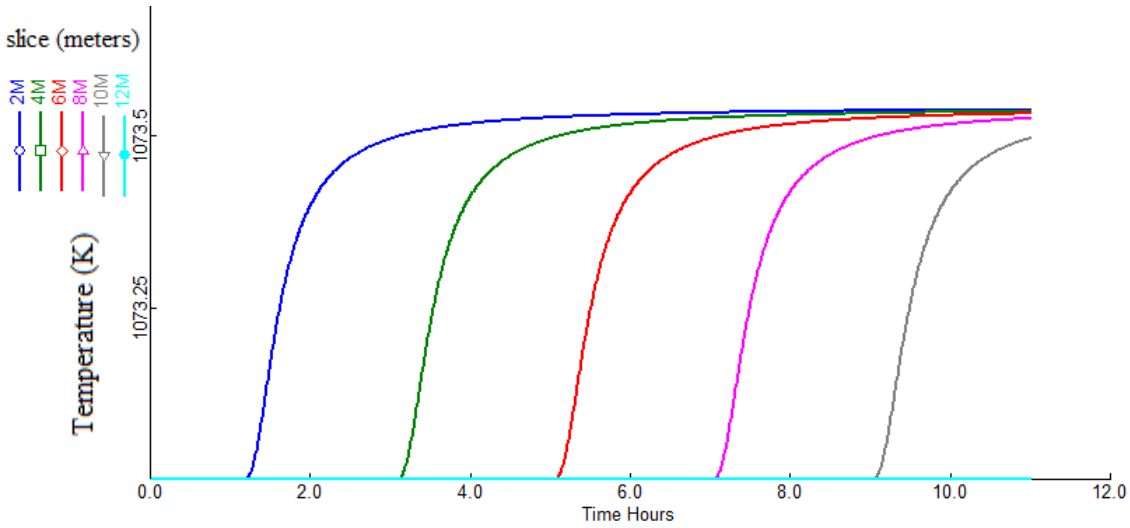

Figure 31 - Temperature profile of the reactor in slices of 2, 4, 6, 8, 10 and 12 meters for a feed flow rate of 0.4 kmol/h (reduction step).

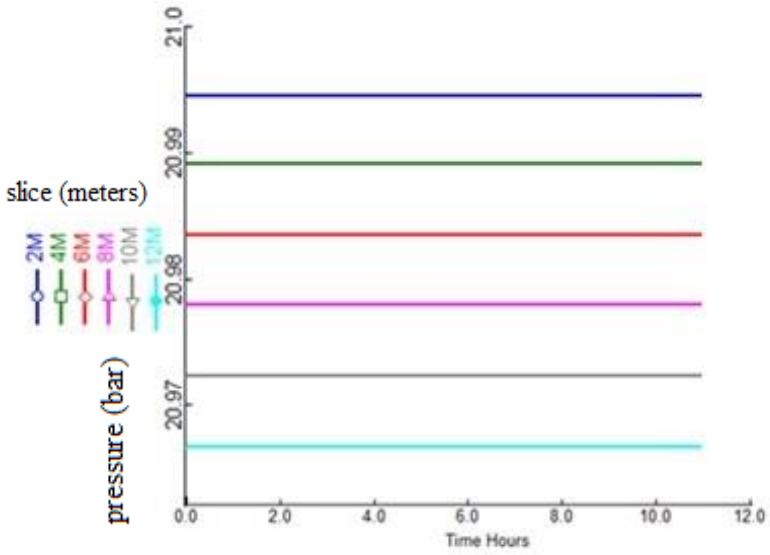

Figure 32 - Pressure (bar) over 12 meters of reactor in 11 hours for a feed of 0.4 kmol/h (reduction step).

Figure 30 shows that, within 11 hours of reaction, there is a complete conversion of products into reactants. However, in the last 12 meters of the reactor, there is a low conversion of magnetite to iron. Figure 31 shows a slight increase in the reactor temperature as the reaction progresses through each section. At the end of the 11 hours of reaction, the reactor maintains a temperature of 1073 K at 2 meters and 1073.5 K at 12 meters. This occurs due to low solids conversion at the end of the reactor. Finally, Figure 32 illustrates the pressure drop in the reactor, and the pressure loss is minimal, which indicates that the gas input at 21 bar is sufficient at the reactor inlet. It is worth noting that the flow rate changes, from 0.5 kmol/h of H_2 to 0.4 kmol/h, do not present significant changes in the pressure drop.

After a period of four hours of reaction, the first cycle of chemical looping is concluded. At this stage, the reactor responsible for the oxidation reaction is converted to the reduction reaction, while the reactor that performed reduction in the previous cycle is transformed for oxidation in the second cycle. It is noteworthy that, during this time interval, the reactors have not yet reached saturation, resulting in a solid distribution profile along the reactor as illustrated in Figures 33 and 34.

Figure 33 presents relevant information about the behavior of the conversion of iron to magnetite after the oxidation reaction. In this context, most of the conversion of iron to magnetite occurs in the first 8 meters of the reactor. This profile represents the distribution of solids that will serve as a reference for the reduction stage in the second cycle of the chemical

looping process. This highlights the importance of this specific phase of the reaction and its impact on the distribution of the solid throughout the reactor.

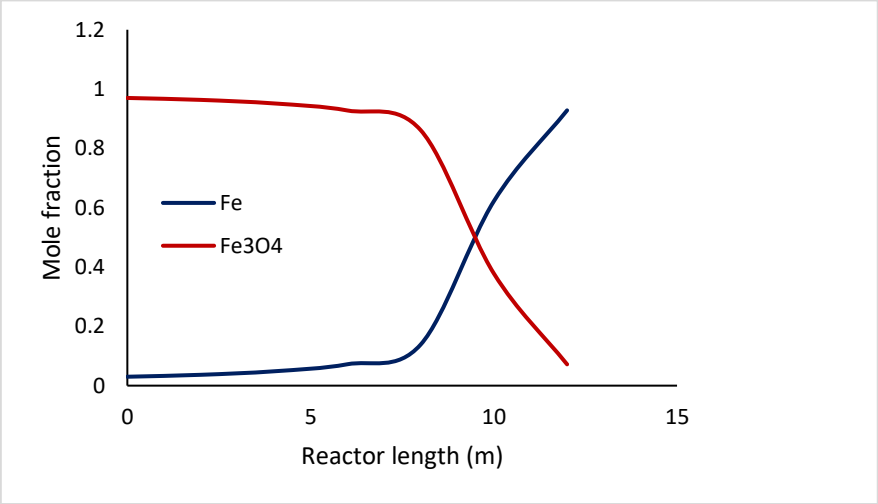

Figure 33 - Solid distribution profile along the oxidation reactor at the end of 11 hours (oxidation step).

Figure 34 provides valuable insights into the behavior of magnetite conversion to iron after the reduction reaction. Significantly, most of the magnetite conversion to iron occurs within the first 10 meters of the reactor. This conversion profile reflects the distribution of the solid that will serve as the basis for the oxidation stage in the second cycle of the chemical looping process.

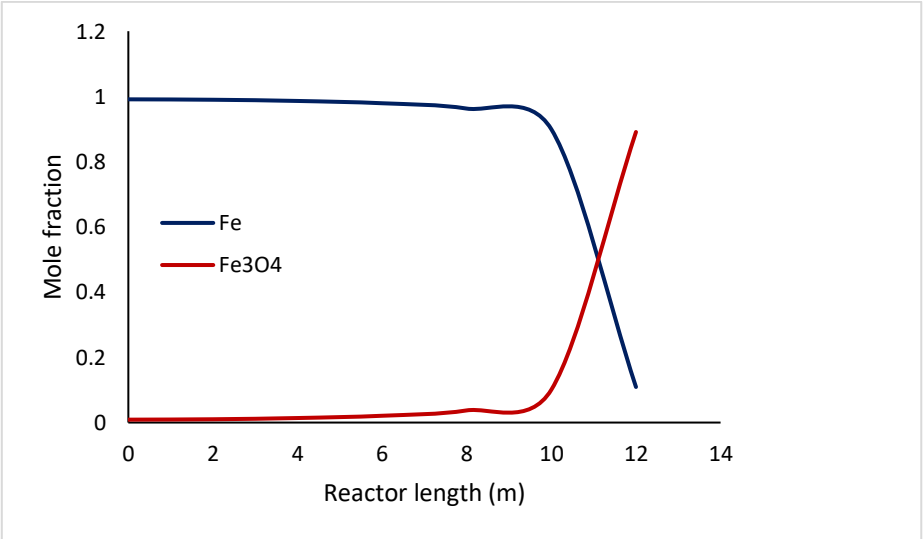

Figure 34 - Solid distribution profile along the reduction reactor at the end of 11 hours (reduction step).

Figures 35, 36, and 37 depict the results of the chemical looping in the second reaction cycle for the oxidation reaction. These illustrations provide a representation of the changes and performance of the chemical process throughout this specific oxidation cycle, offering valuable insights for the analysis and improvement of the oxidation reaction in question.

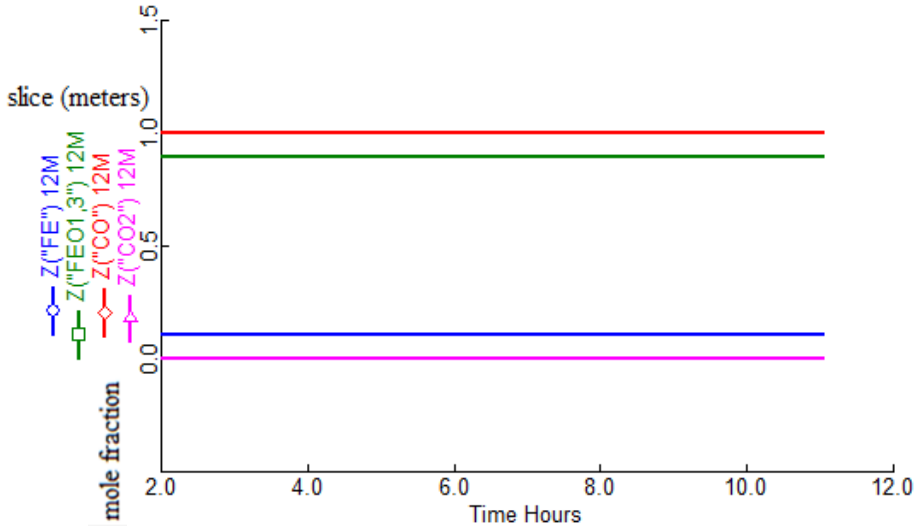

Figure 35 - Conversion of CO_2 to CO and Fe to magnetite at the end of 12 meters of reactor with a feed flow rate of 0.5 kmol/h (oxidation step).

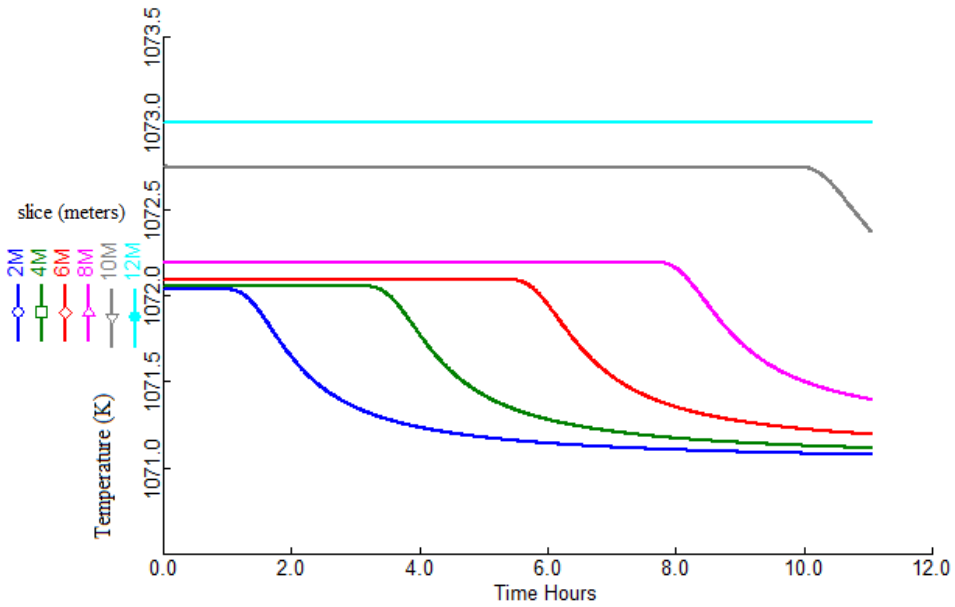

Figure 36 - Temperature profile of the reactor in slices of 2, 4, 6, 8, 10 and 12 meters for a feed flow rate of 0.5 kmol/h (oxidation step).

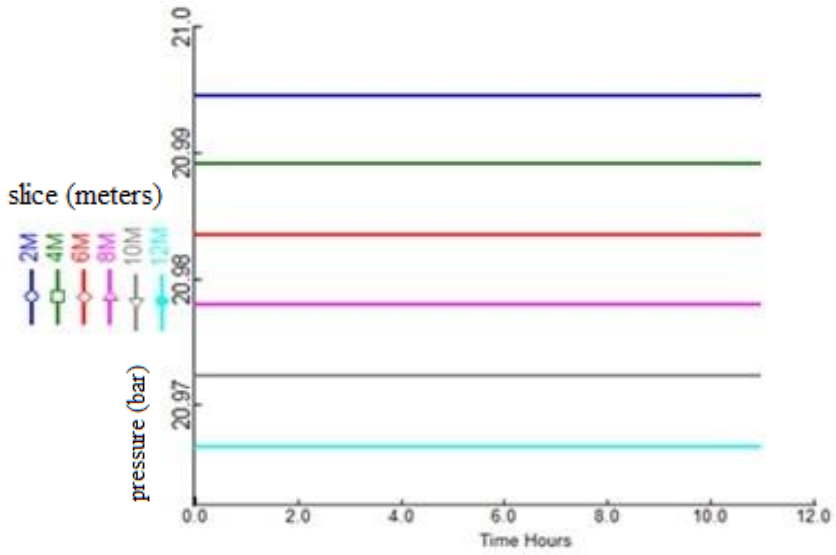

Figure 37 - Pressure (bar) over 12 meters of reactor in 11 hours for a feed of 0.5 kmol/h (oxidation step).

As shown in Figure 35, concerning the oxidation of the second cycle, the conversion of iron to magnetite is more significant in the last 12 meters of the reactor. Even after 11 hours of operation, there is still 100% conversion of reactants to products. Figure 36 shows a variation in the temperature curve compared to the first cycle. This change occurs due to the initial temperature of the reactor, as the oxidation reactor of the second cycle previously operated as a reduction reactor in the first cycle. This means that the second-cycle reactor starts with the temperature curve of the first reduction cycle. The temperature decreases slightly as the reaction progresses in each section. Figure 37 demonstrates that the pressure drop remains similar to that of the first reduction cycle, requiring no changes to the reactor's inlet pressure.

Figures 38, 39, and 40 show the outcomes of the chemical looping in the second reaction cycle, specifically for the reduction reaction. These figures offer insights into the changes and performance of the chemical process during this particular reduction cycle, providing valuable information for the analysis and refinement of the reduction reaction at hand.

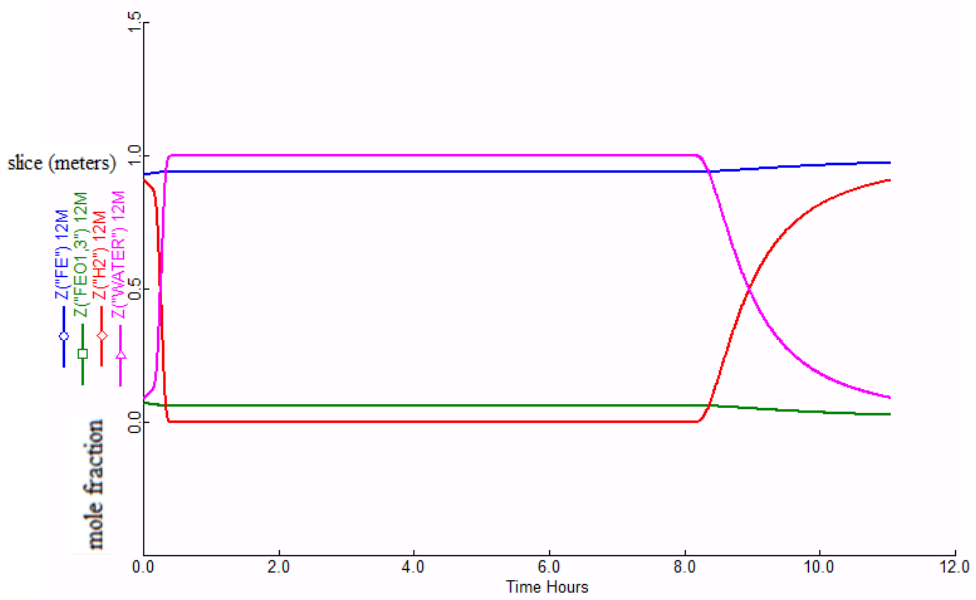

Figure 38 - Conversion of H_2 to H_2O and magnetite to Fe at the end of 12 meters of reactor with a feed flow rate of 0.4 kmol/h (reduction step).

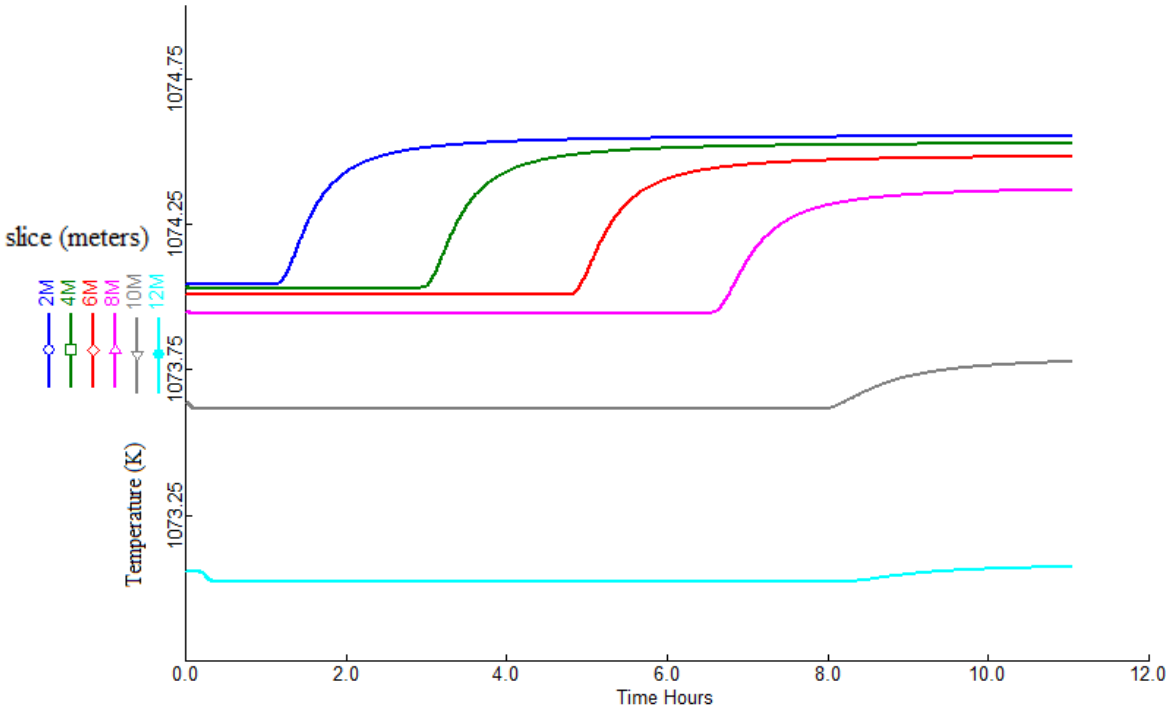

Figure 39 - Temperature profile of the reactor in slices of 2, 4, 6, 8, 10 and 12 meters for a feed flow rate of 0.4 kmol/h (reduction step).

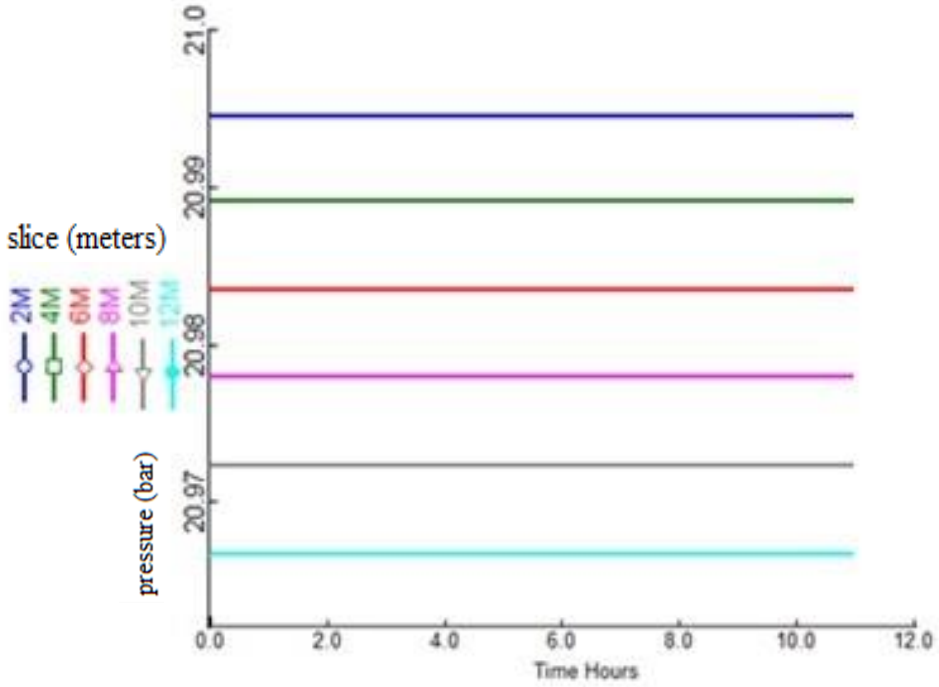

Figure 40 - Pressure (bar) over 12 meters of reactor in 11 hours for a feed of 0.4 kmol/h (reduction step).

In Figure 38, referring to the reduction of the second cycle, a small conversion of magnetite to iron is observed in the last 12 meters of the reactor. Unlike the first cycle, after 11 hours of operation, there is no longer 100% conversion of reactants into products. In this second cycle, the distribution of solids in the reactor does not favor the complete reaction, which is not necessarily problematic, since the objective of the reaction is to produce 100% CO in the reduction stage. To deal with the mixing of H_2 and water at the outlet of the reduction reactor, considerations such as evaluating a recycle to obtain a higher concentration of water at the outlet, adding a subsequent separation step, or reducing the H_2 inlet flow rate to increase residence time can be explored in further work.

Figure 39 shows a variation in the temperature curve in relation to the first cycle due to the initial temperature of the reactor, since the reactor in the second reduction cycle previously operated as an oxidation reactor in the first cycle, inheriting the temperature curve. The temperature increases slightly as the reaction progresses through each section. Figure 40 demonstrates that the pressure drop remains similar to that of the first reduction cycle, not requiring any change in pressure at the reactor inlet.

Figures 41 and 42 depict the solid profile throughout the reactor after the second chemical looping cycle.

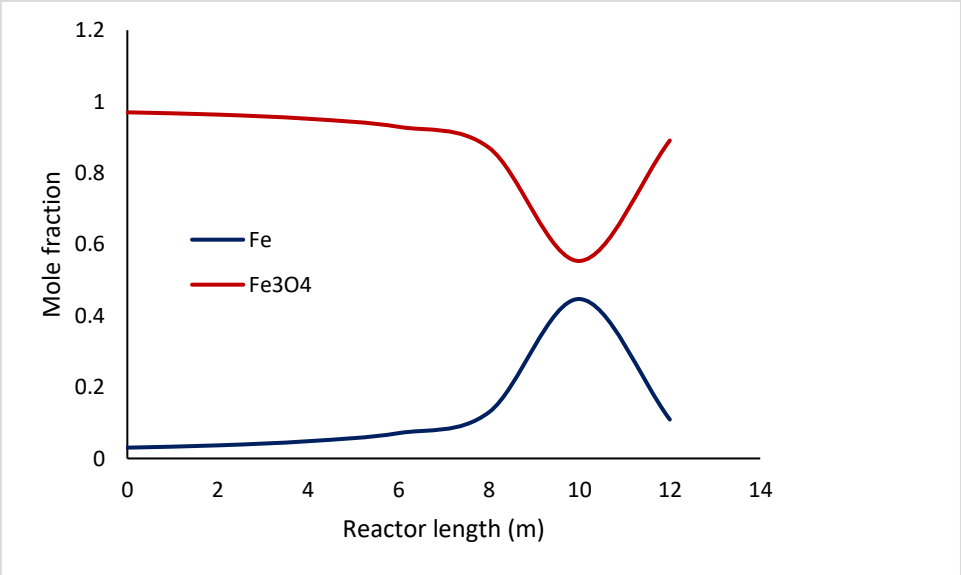

Figure 41 - Solid distribution profile along the reduction reactor at the end of 11 hours (second oxidation step).

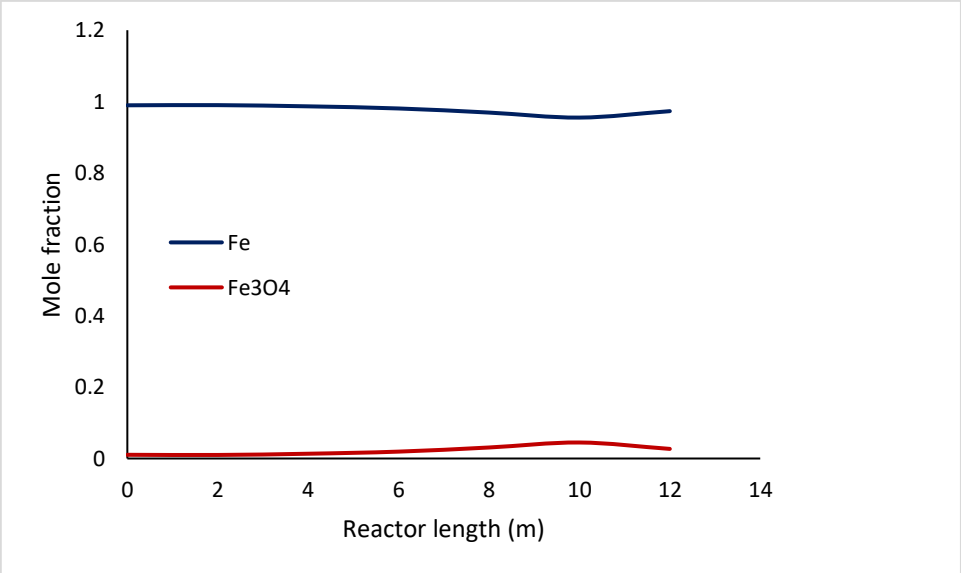

Figure 42 - Solid distribution profile along the reduction reactor at the end of 11 hours (second reduction step).

Figures 41 and 42 show the solid distribution in the second cycle of the process. The conversion in the oxidation stage remains similar to that in the second stage, as well as the conversion in the reduction stage. After the third cycle, the distribution of solids throughout the reactors is the same as the distribution after the first cycle. In this way, the process enters a repetitive cycle, presenting results similar to those already discussed in this work.

5.3 ENVIRONMENTAL AND ECONOMIC ASSESSMENT

In order to conduct the environmental and economic analyses, several considerations were meticulously incorporated to assess the potential of the chemical looping process for CO production. In this context, the conditions of the initial looping cycle were taken into account, assuming 100% conversion of reactants into products, thus obviating the need for subsequent separation steps. This information was subsequently implemented into stoichiometric reactors within the Aspen Plus software, integrated with heat exchangers for energy integration, and compressors for reagent inlet pressure adjustment, as depicted in Figure 43.

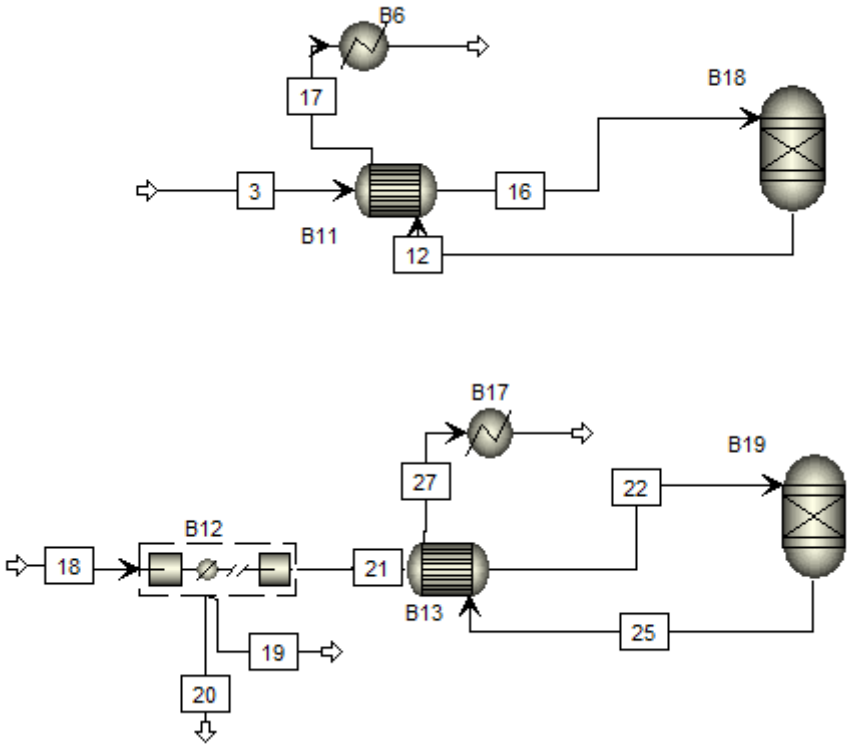

Figure 43 - Conceptual design of processes RWGS-CL.

For the environmental and economic analyzes a multitubular reactor was considered with a total feed flow of 50 tons per hour of CO_2, this flow was determined by the project as the desired feed flow. To process this flow, 2,273 tubes were used, highlighting that the evaluations presented previously considered only a single tube.

For chemical looping to occur, the reactor must play a dual role, operating alternately as a reduction reactor and an oxidation reactor. It is essential that the same number of tubes are

available in both reactors to ensure process continuity and consistent production of the desired CO.

It is worth noting that these are preliminary economic and environmental analyzes since the process can be optimized and integrated into a previous stage of hydrogen production and a subsequent stage of Fischer–Tropsch synthesis, thus requiring a new evaluation.

5.3.1 Environmental assessment

The RWGS-CL process utilizes CO_2 as a feedstock, converting it into CO without direct CO_2 emissions. However, the operation of the process requires the use of electrical energy and natural gas burning to heat the reactors, resulting in an indirect emission of 2.7 tonne of CO_2-eq/h. This corresponds to 8.4% of the CO_2 captured by the process. Therefore, it can be stated that, despite the indirect CO_2 emission, the process has a positive environmental balance of CO_2 by chemical capture, since it consumes more CO_2 than it emits.

5.3.2 Economic assessment

Regarding costs, the FCI (Fixed Capital Investment) of the RWGS-CL proposal is approximately 20.6 MMUS$, while the operational cost is around 12.5 MMUS$/year, consisting of 22% utilities, 21% operational labor, and 57% raw materials. Additionally, the revenue generated by the sale of products (CO and H_2O) accounts to 15.9 MMU$/year.

The cash flow over the 17 years of construction and operation is depicted in Figure 44. The Net Present Value (NPV) is also 46.53 MMUS$, and the return on investment (ROI) cannot be determined (NA). The cash flow becomes positive after 17 years of operation.

These results indicate that under such conditions, even if there are no subsequent separation steps, RWGS-CL is not financially viable and investing in this approach would result in capital losses.

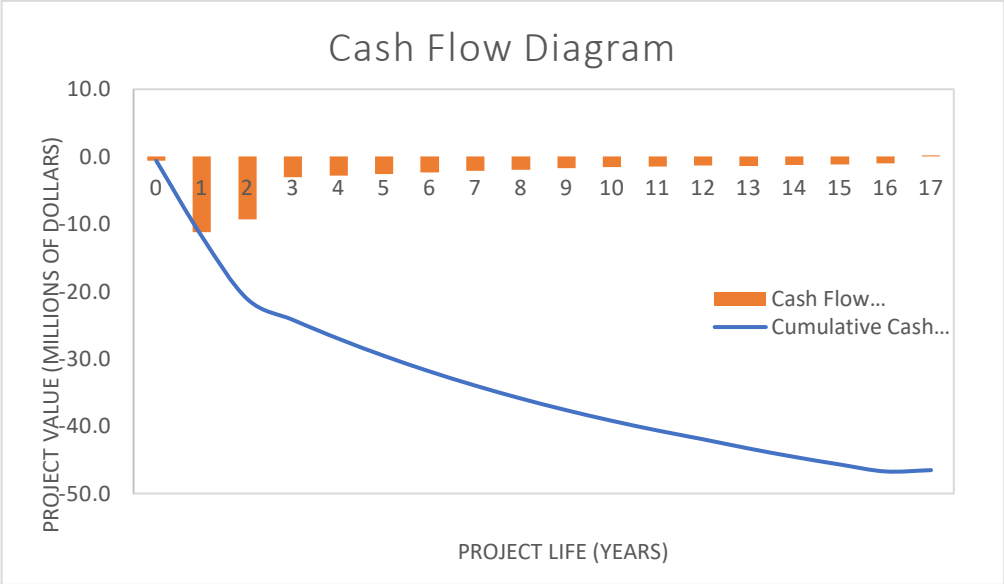

Figure 44 - Cash flow diagram for RWGS-CL in the Brazilian scenario.

6 CONCLUSIONS

In this study, the RWGS-CL process was detailed explored. The complex dynamics of the reactions involved in the process was investigated, with special focus on the interactions between the oxidation and reduction stages. With the help of numerical simulations, valuable information about the behavior of the system over time and across the reactor were obtained. These simulations provided fundamental insights into how varying parameters such as feed rate can affect process efficiency.

In this study, it was observed that reduction and oxidation reactions are favored by longer residence times, leading to the evaluation of lower flow rates. Three different flow rates were analyzed for one tube: 0.5 kmol/h, 1 kmol/h, and 1.5 kmol/h. The flow rate of 0.5 kmol/h was chosen as it provided a 100% conversion of CO_2 to CO for a more extended period (11 hours). To ensure the appropriate reaction time between reduction and oxidation reactions, the H_2 flow rate was adjusted to 0.4 kmol/h in the reduction stage. It was highlighted that in the second looping cycle, there is not a 100% conversion of H_2 to H_2O in the reduction reaction, indicating the need for optimization in future work to enhance this conversion. Additionally, it was noted that when the reactor starts heated at 1073K, there is no significant temperature variation in both reactors. Regarding pressure, the pressure drop along the reactor length is considered negligible. To process 50t/h of CO_2, as defined in the project to which this work contributed, 2273 tubes were required for both reactors, as reduction and oxidation reactions alternate between them.

Furthermore, the environmental analysis showed a promising potential of CO_2 capture in this context, highlighting the important role this process can play in mitigating carbon dioxide emissions. However, the economic analysis revealed significant challenges regarding the viability of RWGS-CL under the conditions considered.

Therefore, this study not only expands our understanding of the chemical reactions underlying RWGS-CL, but also highlights the complexities and challenges involved in its practical implementation on an industrial scale. As we move toward cleaner, alternative energy sources, the findings of this study provide crucial information for future research and development efforts in this field. Simulation has played a central role in exploring these complex processes, helping to guide our discoveries and direct next steps in the research and development of RWGS-CL technology.

7 SUGGESTIONS FOR FUTURE WORK

This chapter provides a set of suggestions to guide future research in the field of syngas production using RWGS-CL. The suggestions range from process optimization to its integration into a broader industrial context.

- **Evaluation of Recycle for the Reduction Stage:** Another significant suggestion is to evaluate the recycle in the second stage of the loop for the reduction stage. In this case, the goal would also be to optimize hydrogen utilization. By recycling a portion of the products obtained in the reduction stage, it would be feasible to reduce the amount of H_2 required for the reaction. This wouldn't just optimize hydrogen use but could also have positive impacts on overall process efficiency and performance.

- **Integration of the Complete Syngas and Fuels Production Processes:** Another relevant suggestion is the comprehensive integration of the entire syngas production process through RWGS-CL, considering all necessary steps and equipment. This scope would encompass the RWGS-CL reactor to the hydrogen production Fischer-Tropsch synthesis steps. Investigating the integration of these steps would allow for assessing the technical and economic feasibility of the production process, considering it as a complete system. This approach would also provide a deeper understanding of interactions among the different process steps.

- **Economic and Environmental Analyses of the Optimized Process:** Once the optimized process, including potential recycles and full step integration, has been outlined, conducting a thorough economic and environmental analysis is crucial. This would involve detailed assessment of operational and investment costs associated with the optimized process, as well as quantification of environmental benefits, such as CO_2 emissions reduction. Economic and environmental analyses are pivotal to verify the industrial viability of process, identifying its strengths and challenges in a practical context.

The suggestions outlined in this chapter lay out a range of promising directions for future investigations in the realm of syngas production using RWGS-CL. From process refinement to

the assessment of its economic and environmental feasibility, these suggestions pave the way for research that can significantly contribute to advancing syngas production technology and its industrial application.

REFERENCES[1]

ADANEZ, J., ABAD, A., GARCIA-LABIANO, F., GAYAN, P., DIEGO, F. L. Progress in chemical-looping combustion and reforming technologies. **Progress in Energy and Combustion Science.** v. 38, n. 2, p. 215-282, Apr. 2012.

AGÊNCIA NACIONAL DE ENERGIA ELÉTRICA. **REH - Resolução homologatória 3053/2022.** Disponível em: <https://biblioteca.aneel.gov.br/acervo/detalhe/224785 #:~:text=Homologa%20o%20resultado%20do%20reajuste,Distribui%C3%A7%C3%A3o%20S%C3%A3o%20Paulo%20%2D%20Enel%20SP.>. Acesso em: 1 abr. 2023.

AGÊNCIA NACIONAL DO PETRÓLEO, G. N. E B. (ANP). **Anuário estatístico brasileiro do petróleo, gás natural e biocombustíveis 2022.** Disponível em: <https://www.gov.br/anp/pt-br/centrais-de-conteudo/publicacoes/anuario-estatistico/arquivos-anuario-estatistico-2022/anuario-2022.pdf>. Acesso em: 21 mar. 2023.

AHMEDA, M. M, UPADHYAYB, R. K., TIWARIA. P. CO_2 techno economic comparison of combustor integrated steam reforming and sorption enhanced chemical looping steam reforming of methanol. **Chemical Engineering Research and Design.** v. 192, n. 23, p. 299-309, Apr. 2023.

AL-MAMOORI, A., KRISHNAMURTHY, A., ROWNAGHI, A. A., REZAEI, F. Carbon capture and utilization update. **Energy Technology**. v. 5, n. 6, p. 834-849, Jun. 2017.

ALMEIDA, I. C., GONÇALVES, S. B., MACHADO, F. Simulação do processo de produção de etanol de arroz brs ag usando aspen plus. **VI Encontro de Pesquisa e Inovação da Embrapa Agroenergia: Anais.** v. 1, n. 20, p. 173-180, 2020.

ANDREONI, L., BARONCINI, M., GROPPI, J., SILVI, S., TATICCHI, C., CREDI, A. Photochemical energy conversion with artificial molecular machines. **Energy and Fuels.** v. 35, n. 23, p. 18900-18914, Oct. 2021.

BABU, P., LINGA, P., KUMAR, R., ENGLEZOS, P. A review of the hydrate based gas separation (HBGS) process for carbon dioxide pre-combustion capture. **Energy.** v. 85, n. 70, p. 261-279, Jun. 2015.

CASTELLANOS-BELTRAN, I. J., PERREAULT, L. S., BRAIDY, N. Application of ni−spinel in the chemical-looping conversion of co_2 to co via induction-generated oxygen vacancies. **The Journal of Physical Chemistry C.** v. 125, n. 13, p. 7213-7226, Mar. 2021.

[1] According to the Associação Brasileira de Normas Técnicas (ABNT NBR 6023)

CHAO, C., DENG, Y., DEWIL, R., BAEYENS, J., FAN, X. Post-combustion carbon capture. **Renewable and Sustainable Energy Reviews.** v. 138, n. 1, p. 110490, Mar. 2021.

CHEMENGONLINE. **Chemical engineering essential for the CPI professional 2023.** Disponível em: <https://www.chemeengonline.com/issues/2023-09>. Acesso em: 11 ago. 2023.

CHEMENGGUY. **What is Aspen Plus?.** Disponível em: <https://www.chemicalengineering guy.com/the-blog/process-simulation/what-is-aspen-plus/>. Acesso em: 10 ago. 2023.

CHRISTENSEN, A. 2020. **Assessment of hydrogen production costs from electrolysis: United States and Europe.** Disponível em: <https://theicct.org/publication/assessment-of-hydr ogen-production-costs-from-electrolysis-united-states-and-europe/>. Acesso em: 1 de jun. 2023.

DAZA, Y.A.; KENT, R.A.; YUNG, M.M.; KUHN, J.N. Carbon dioxide conversion by reverse water–gas shift chemical looping on perovskite-type oxides. **Industrial and Engineering Chemistry Research** v. 53, n. 14, p. 5828–5837, Mar. 2014.

DAZA, Y. A., MAITI, D., KENT, R. A., BHETHANABOTLA, V. R., KUHN, J. N. Isothermal reverse water gas shift chemical looping on $La_{0.75}Sr_{0.25}Co_{(1-Y)}Fe_YO_3$ perovskite-type oxides. **Catalysis Today.** v. 258, n. 2, p. 691-698, Dec. 2015.

EVDOU, A., ZASPALIS, V., NALBANDIAN, L Ferrites as redox catalysts for chemical looping processes. **Fuel.** v. 165, n. 3, p. 367-378, Feb. 2016.

FLORES-GRANOBLES, M., SAEYS, M. Dynamic pressure-swing chemical looping process for the recovery of CO from blast furnace gas. **Energy Conversion and Management.** v. 258, n. 22, p. 115520, Apr. 2022.

FURTER, W. F. 2020. **Chemical conversion.** Disponível em:<https://www.accesssci ence.com/content/article/a126700>. Acesso em: 3 ago. 2023.

GRACIANO, J. E. A.; CHACHUAT, B.; ALVES, R. M. B. Conversion of co_2 -rich natural gas to liquid transportation fuels via trireforming and fischer–tropsch synthesis: model-based assessment. **Industrial & Engineering Chemistry Research.** v. 57, n. 30, p. 9964–9976, Apr. 2018.

HARE, B. J., MAITI, D., RAMANI, S., RAMOS, A. E., BHETHANABOTLA, V. R., KUHN, J. N. Thermochemical conversion of carbon dioxide by reverse water-gas shift chemical looping using supported perovskite oxides. **Catalysis Today.** v. 323, n. 19, p. 225-232, Jun. 2019.

HU, Q., WANG, C. Insight into the Fe_2O_3/CaO-based chemical looping process for biomass conversion. **Bioresource Technology.** v. 310, n. 20, p. 123384, Aug. 2020.

HUNPINYOA, P., NARATARUKSA, P., TUNGKAMANI, S., PANA-SUPPAMASSADUA, K., CHOLLACOOP, N. Evaluation of techno-economic feasibility biomass-to-energy by using aspen plus®: a case study of thailand. **The Mediterranean Green Energy Forum.** v. 42, n. 13, p. 640-649, 2013.

IWAMA, R., TAKIZAWA, K., SHINMEI, K., BABA, E., YAGIHASHI, N., KANEKO, H. Design and analysis of metal oxides for co_2 reduction using machine learning, transfer learning, and bayesian optimization. **ACS Omega.** v. 593, n. 7, p. 10709-10717, Mar. 2022.

INTERNATIONAL ENERGY AGENCY. **The future of hydrogen: seizing today's opportunities.** Disponível em: <https://www.iea.org/events/the-future-of-hydrogen-seizing-todays-opportunities>. Acesso em: 1 abr. 2023.

INTERNATIONAL ENERGY AGENCY. **Electrolysers.** [s.l: s.n.]. Disponível em: <https://www.iea.org/reports/electrolysers>. Acesso em: 1 abr. 2023.

JIN, R., EASA, J., O`BRIEN, P. C. Highly active cuo_x/sio_2 dot core/rod shell catalysts with enhanced stability for the reverse water gas shift reaction. **ACS Applied Materials and Interfaces.** v. 13, n. 32, p. 38213-38220, Aug. 2021.

KIM, S. S., LEE, H. H., HONG, C. S. A study on the effect of support's reducibility on the reverse water-gas shift reaction over Pt catalysts. **Applied Catalysis A: General.** v. 423-424, n. 12, p. 100-107, May. 2012.

KIRSCH, H., SOMMER, U., PFEIFER, P., DITTMEYER, R. Power-to-fuel conversion based on reverse water-gas-shift, fischer-tropsch synthesis and hydrocracking: mathematical modeling and simulation in matlab/simulink. **Chemical Engineering Science.** v. 227, n. 3, p. 115930, Jun. 2020.

KOBOS, P. H., DRENNEN, T. E., OUTKIN, A., WEBB, E. K., PAAP S. M., WIRYADINATA, S. **Techno-economic analysis: best practices and assessment tools.** Sandia Report. p. 1-189, 2020.

KUHN, J., HARE, B., MAITI, D., DAZA, Y., BHETHANABOTLA, V. **Supported perovskite-oxide composites for enhanced low temperature thermochemical conversion of CO_2 to CO.** 2018. Disponível em: <https://patentscope. wipo.int/search/en/detail.jsf?doc Id=US29 4405486 & _fid=WO2018222749>. Acesso em: 20 de set. de 2021.

KUO, Y., HSU, W., CHIU, P., TSENG, Y., KU, Y. Assessment of redox behavior of nickel ferrite as oxygen carriers for chemical looping process. **Ceramics International.** v. 39, n. 5, p. 5459-5465, Jul. 2013.

LEE, M., KIM, Y., LIM, H. S., JO, A., KANG, D., LEE, J. W. Reverse water–gas shift chemical looping using a core–shell structured perovskite oxygen carrier. **Energies.** v. 13, n. 20, p. 1-12, Oct. 2020.

LE SACHE, E., PASTOR-PÉREZ, L., HAYCOCK, B. J., VILLORA-PICO, J. J., SEPULVEDA-ESCRIBANO, A., REINA, T. R. Switchable catalysts for chemical co_2 recycling: a step forward in the methanation and reverse water−gas shift reactions. **ACS Sustainable Chemistry Engineering.** v. 8, n. 11, p. 4614-4622, Mar. 2020.

LOILAND, A. J., WULFERS, J. M., MARINKOVIC, S. N., LOBO, F. R. Fe/γ-Al_2O_3 and Fe–K/γ-Al_2O_3 as reverse water-gas shift catalysts. **Catalysis, Science and Technology.** v. 6, n. 14, p. 5227-5758, Jan. 2016.

LYNGFELT, A., BRINK, A., LANGØRGEN, Ø., MATTISSON, T., RYDÉN, M., LINDERHOLM, C. 11,000 h of chemical-looping combustion operation—where are we and where do we want to go?. **International Journal of Greenhouse Gas Control.** v. 88, n. 19, p. 38-56, Sep. 2019.

MAKIURA, J., KAKIHARA, S., HIGO, T., ITO, N., HIRANO, Y., SEKINE, Y. Efficient co_2 conversion to CO using chemical looping over Co–In oxide. **Chemical Communications.** v. 58, n. 31, p. 4803-4920, Mar. 2022.

MCLAUGHLIN, H., LITTLEFIELD, A. A., MENEFEE, M., KINZER, A., HULL, T., SOVACOOL, B. K., BAZILIAN, M. D., KIM, J., STEVEN GRIFFITHS, S. Carbon capture utilization and storage in review: sociotechnical implications for a carbon reliant world. **Renewable and Sustainable Energy Reviews.** v. 177, n. 23, p. 113215, May. 2023.

MINBEOM LEE, M., KIM, Y., LIM, H. S., JO, A., KANG, D., LEE, J. W. Reverse water–gas shift chemical looping using a core–shell structured perovskite oxygen carrier. **Energies.** v. 13, n. 20, p. 5324, Oct. 2020.

MEHRPOOYA, M., SHARIFZADEH, M. M. M., RAJABI, M., AGHBASHLO, M., TABATABAI, M., HOSSEINPOUR, S., RAMAKRISHNA, S. Design of an integrated process for simultaneous chemical looping hydrogen production and electricity generation with CO_2 capture. **Science Direct.** v. 42, n. 12, p. 8486-8496, Jan. 2017.

MEIRELLES, F. S. **Biodiesel**. Serviço nacional de aprendizado rural. Brasília, 2003.

M. Ö. ÇARPINLIOĞLU AND E. ÖZAHI. A simplified correlation for fixed bed pressure drop. **Powder Technol**. v. 187, n. 1, p. 94–101, Oct. 2008.

MENG, X. W., BANERJEE, S., ZHANG, X., AGARWAL, K. R. Process simulation of multi-stage chemical-looping combustion using Aspen Plus. **Energy.** v. 90, n. 2, p. 1869-1877, Oct. 2016.

MU, D., XIN, C., ZHOU, W. Life cycle assessment and techno-economic analysis of algal biofuel production. **Microalgae cultivation for biofuels production.** v. 18, n. 20, p. 281-292, 2020.

NITYASHREE, N., PRICE, H. A. C., PASTOR-PEREZ, L., MANOHARA, V. G., GARCIA, S., MAROTO-VALER, M. M., REINA, R. T. Carbon stabilised saponite supported transition metal-alloy catalysts for chemical CO_2 utilization via reverse water-gas shift reaction. **Applied Catalysis B: Environmental.** v. 261, n. 20, p. 118241, Sep. 2020.

OSHIMA, K., SHINAGAWA, T., NOGAMI, Y., MANABE, R., OGO, S., SEKINE, Y. Low temperature catalytic reverse water gas shift reaction assisted by an electric field. **Catalysis Today.** v. 232, n. 14, p. 27-32, Sep. 2014.

OUYANGA, X., LAI, D. Y. F., MARCHAND, C., S., LEE, S. Y. **Chapter 1 - introduction. carbon mineralization in coastal wetlands.** p. 1-24, 2022.

OVERA, S., KO, B. H., ZHAO, Y., JIAO, F. Electrochemical approaches for co_2 conversion to chemicals: a journey toward practical applications. **Accounts of Chemical Research.** v. 55, n. 5, p. 638-648, Jan. 2022.

ÖZKARA-AYDINOĞLU, Ş. Thermodynamic equilibrium analysis of combined carbon dioxide reforming with steam reforming of methane to syntheses gas. **International Journal of Hydrogen Energy.** v. 35, n. 23, p.12821-12828, Dec. 2010.

PALA, L. P. R., WANG, Q., KOLB, G., HESSEL. Steam gasification of biomass with subsequent syngas adjustment using shift reaction for syngas production: an Aspen Plus model. **Renewable Energy.** v. 101, n. 17, p. 484-492, Feb. 2017.

PANWAR, N. L., KAUSHIK S.C, KOTHARI, S. Role of renewable energy sources in environmental protection: a review. **Renewable and Sustainable Energy Reviews.** v. 15, n. 3, p. 1513-1524, Apr. 2011.

PASTOR-PÉREZ, L., BAIBARS, F., LE SACHE, E., ARELLANO-GARCÍA, H., GU, S., REINA, T. R. CO_2 valorisation via reverse water-gas shift reaction using advanced Cs doped Fe-Cu/Al_2O_3 catalysts. **Journal of CO_2 Utilization.** v. 21, n. 17, p. 423-428, Oct. 2017.

PEREIRA, M. **Fixed bed reactor. Marco eng.** Disponível em:<website:http://www.marco .eng.br/reatores/reatorleitofixo.html#:~:text=É também referido como reator,que os outros reatores tubulares >. Acesso em: 22 de mar. de 2022.

PENG, D.-Y.; ROBINSON, D. B. A new two-constant equation of state. **Industrial & Engineering Chemistry Fundamentals.** v. 15, n. 1, p. 59–64, Feb. 1976.

PETROBRAS. **Tudo o que você precisa saber sobre os preços dos combustíveis.** Disponível em: < https://precos.petrobras.com.br/>. Acesso em: 1 jun. 2023.

PENG, H., DI, Z., GONG, P., YANG, F., CHENG, F. Techno-economic assessment of a chemical looping splitting system for H_2 and CO Co-generation. **Green Energy & Environment.** v. 8, n. 1, p. 338-350, Feb. 2023.

PRICE, H. A. C., PASTOR-PEREZ, L., REINA, R. T., LIU, J. Yolk-Shell structured NiCo@SiO_2 nanoreactor for CO_2 upgrading via reverse water-gas shift reaction. **Catalysis Today.** v. 383, n. 22, p. 358-367, Jan. 2022.

RAHMAN, F. A., AZIZ, M. M. A., SAIDUR, R., BAKARD, W. A. W A. B., HAININ, M. R., PUTRAJAYA, R., HASSANA, N. A. Pollution to solution: capture and sequestration of carbon dioxide (co_2) and its utilization as a renewable energy source for a sustainable future. **Renewable and Sustainable Energy Reviews.** v. 71, n. 3, p. 112-126, May. 2017.

ROLFE, S. L., SCHUTTE E. J., WHITE, J. H. **Cyclic catalytic upgrading of chemical species using metal oxide materials.** 2008. Disponível em: < https://worldwide.espacenet.com/patent/search/family/039201314/publication/US2011024687A1?q=RWGS%20for%20chemical%20looping>. Acesso em: 20 de set. de 2021

SAM, A., BARIK, D. **Chapter 2 - toxic waste from municipality.** Woodhead Publishing Series in Energy. p. 7-16, 2019.

SANDVIK, P. **High-pressure natural gas to syngas chemical looping: thermodynamic modeling, gas-to-liquid plant integration, and variable reducer-combustor operating pressure.** 2019. 84 p. Degree Master of Science Thesis - Graduate School of The Ohio State University, Ohio, 2019.

SCITECHDAILY, 2021. **A faster, cooler way to reduce our carbon footprint: copper-indium oxide.** 2020. Disponível em: <https://scitechdaily.com/a-faster-cooler-way-to-reduce-our-carbon-footprint-copper-indium-oxide/>. Acesso em: 20 de set. de 2021.

SHI, H., BHETHANABOTLA, V. R., KUHN, J. N. Pelletized SiO_2-supported La0.5Ba0.5FeO3 for conversion of CO_2 to CO by a reverse water-gas shift chemical looping process. **Journal of Industrial and Engineering Chemistry.** v. 118, n. 23, p. 44-52, Feb. 2023.

SILVA, S. H. L. **Estudo da reação water gás-shift reversa em microrreator capilar-proposta de escalonamento do processo.** 2015. 83 p. Dissertação de Mestrado - Universidade Federal de Pernambuco, Recife, 2015.

SUN, F., YAN, C., WANG, Z., GUO, C., HUANG, S. Ni/Ce-Zr-O catalyst for high CO_2 conversion during reverse water gas shift reaction (RWGS). **International Journal of Hydrogen Energy.** v. 40, n. 46, p. 15985-15993, Dec. 2015.

TURTON, R., BAILIE, R. C., WHITING, W. B., SHAEIWITZ, J. A., BHATTACHARYYA, D. **Analysis, synthesis, and design of chemical Process.** 5. ed. [s.l.] Prentice Hall, 2018.

UDOMSIRICHAKORN, J., SALAM, A. P. Review of hydrogen-enriched gas production from steam gasification of biomass: The prospect of CaO-based chemical looping gasification. **Renewable and Sustainable Energy Reviews.** v. 30, n. 14, p. 565-579, Feb. 2014.

UNITED NATIONS. **Theme report on energy transition.** p. 1-48, 2021.

WANG, J., LIU, C., SENFTLE, P. T., ZHU, J., ZHANG, G., GUO, X., SONG, C. Variation in the in_2o_3 crystal phase alters catalytic performance toward the reverse water gas shift reaction. **ACS Catalysis.** v. 10, n. 5, p. 3264-3273, Dec. 2020.

WEI, G., ZHAO, W., MENG, J., FENG, J., LI, W., HE, F., HUANG, Z., YI, Q., DU, Z., ZHAO, K., ZHAO, Z., LI, H. Hydrogen production from vegetable oil via a chemical looping process with hematite oxygen carriers. **Journal of Cleaner Production.** v. 200, n. 18, p. 588-597, Nov. 2018.

WENZEL, M. **Reverse water-gas shift chemical looping for syngas production from CO_2.** 2018. 149 p. Doctoral thesis - Faculty of Process and Systems Engineering at Otto von Guericke University Magdeburg, Saxônia-Anhalt, 2018.

WENZEL, M., RIHKO-STRUCKMANNA, L., SUNDMACHERA, K. Continuous production of CO from CO_2 by RWGS chemical looping in fixed and fluidized bed reactors. **Chemical Engineering Journal.** v. 336, n. 18, p. 278-296, Mar. 2018.

WENZEL, M., ADITYA DHARANIPRAGADA, N.V.R., GALVITA, V. V., POELMAN, H., MARIN, G. B., RIHKO-STRUCKMANNA, L., SUNDMACHERA, K. CO production from CO_2 via reverse water–gas shift reaction performed in a chemical looping mode: Kinetics on modified iron oxide. **Journal of CO_2 Utilization.** v. 17, n.17, p. 60-68, Jan. 2017.

WOLF, A., JESS, A., KERN, C. Syngas production via reverse water-gas shift reaction over a ni-al $_2$ o $_3$ catalyst: catalyst stability, reaction kinetics, and modeling. **Chemical Engineering and Technology.** v. 39, n. 6, p. 1040–1048, Feb. 2016.

YANG, L., PASTOR-PÉREZ, S., GU, A., SEPÚLVEDA-ESCRIBANO, A., REINA, R. T. Highly efficient Ni/CeO_2-Al_2O_3 catalysts for CO_2 upgrading via reverse water-gas shift: Effect of selected transition metal promoters. **Applied Catalysis B: Environmental.** v. 232, n. 18, p. 464-471, Sep. 2018.

YANG, L., PASTOR-PÉREZ, S., VILLORA-PICO, J. J., GU, A., SEPÚLVEDA-ESCRIBANO, A., REINA, R. T. CO_2 valorization via reverse water-gas shift reaction using promoted Fe/CeO_2-Al_2O_3 catalysts: showcasing the potential of advanced catalysts to explore new processes design. **Applied Catalysis A, General.** v. 593, n. 20, p. 117442, Mar. 2020.

ZHANG, Y., WANG, D., POTTIMURTHY, Y., KONG, F., HSIEH, T., SAKADJIAN, B., CHUNG, C., PARK, C., XU, D., BAO, J., VELAZQUEZ-VARGAS, L., GUO, M., SANDVIK, P., NADGOUDA, S., FLYNN, J. T., TONG, A., FAN, L. Coal direct chemical looping process: 250 kW pilot-scale testing for power generation and carbon capture. **Applied Energy.** v. 282, n. 1, p. 116065, Jan. 2021.

APPENDIX A

In this section the thermodynamic analyzes of the metals evaluated in this work are presented. Another metallic oxide (FeO) was analysed as shown in Figures A1 and A2. In the oxidation reaction, it is noted that only the increase of the temperature influenced the increase of the CO_2 conversion, reaching 85% at 1000°C.

In the reduction reaction, the highest conversion of H_2 was 20% at temperature of 1000°C. The result from Figure 6 is better since it presents greater conversion at the same temperature.

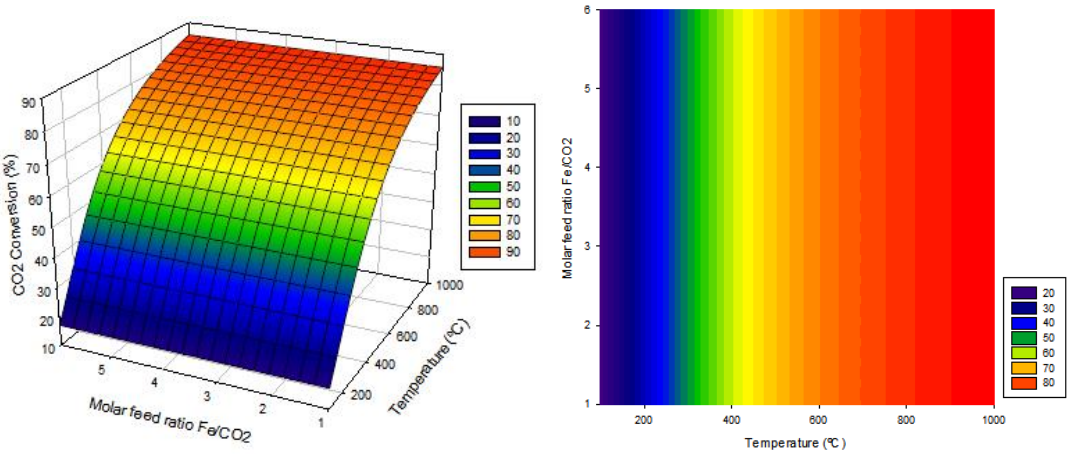

Figure A1- Thermodynamic analysis of the oxidation reaction using FeO.

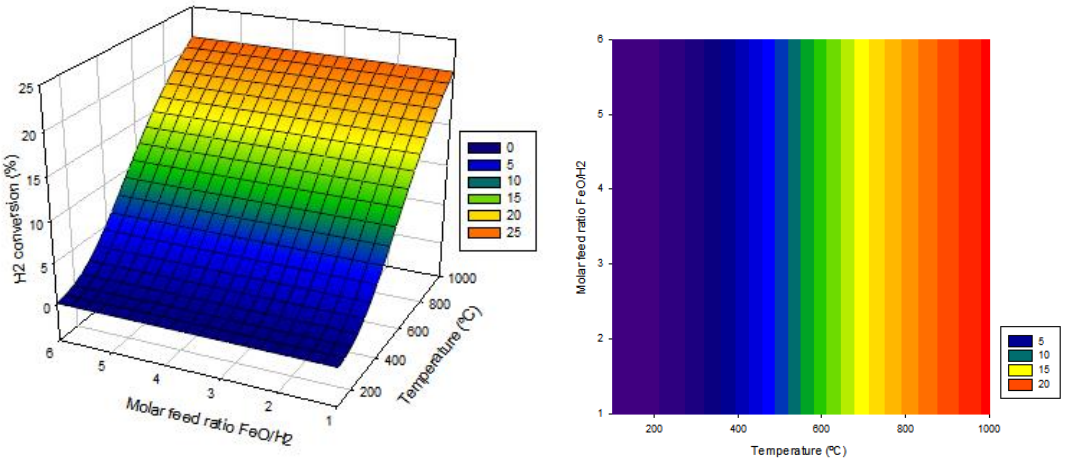

Figure A2- Thermodynamic analysis of the reduction reaction using FeO.

Nickel oxide was also evaluated as shown in Figure A3 and Figure A3. As in the previously evaluated oxides, the molar feed ratio does not influence the increase of the CO_2 conversion (%). The only influence is due to the temperature increase, although it is not expressive since the highest CO_2 conversion is 1% in the oxidation reaction.

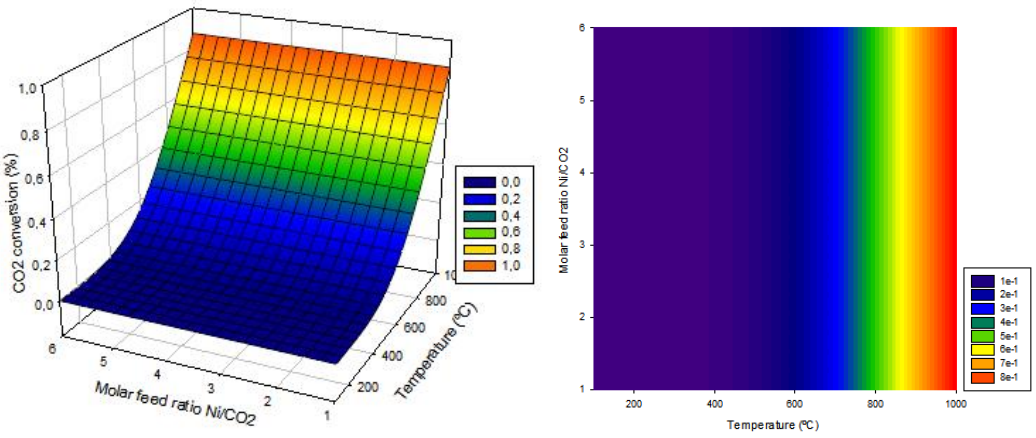

Figure A3- Thermodynamic analysis of the oxidation reaction using NiO.

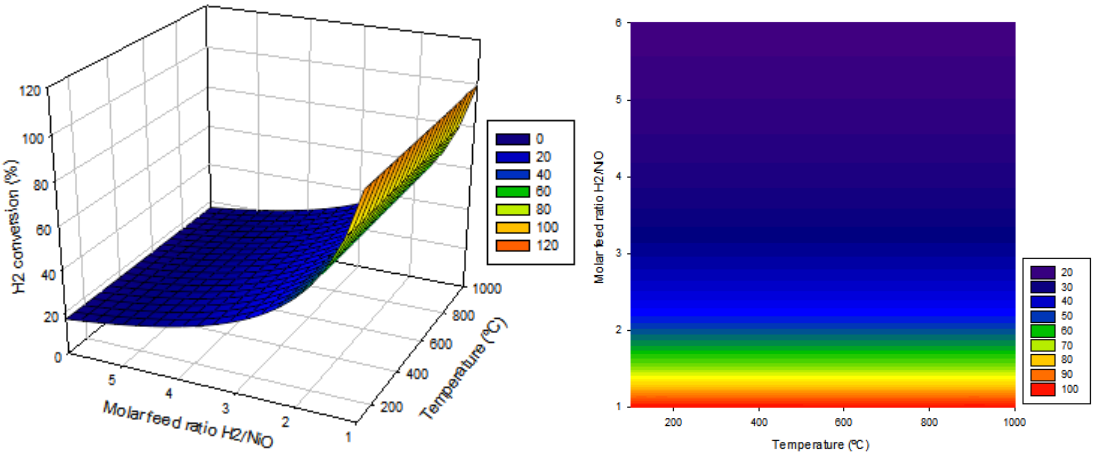

Figure A4- Thermodynamic analysis of the reduction reaction using NiO.

In the reduction reaction, the temperature does not affect the H_2 conversion (%), unlike the H_2/NiO feed molar ratio, which presents H_2 conversion of 100% for ratio equal to 1. Although the H_2 conversion was 100% in the reduction reaction, the CO_2 conversion was very low (1%), making the use of nickel oxide unfeasible.

Figures A5 and A6 present the thermodynamic analysis of cobalt oxide for the oxidation and reduction reactions, respectively. It is observed that the temperature influences the conversion of CO_2 (%) in Figure 11. As higher the temperature, higher the CO_2 conversion. In the reduction reaction, the Co/CO_2 feed molar ratio affects the increase of the H_2 conversion (%). Also, as higher the Co/CO_2 ratio, higher the conversion.

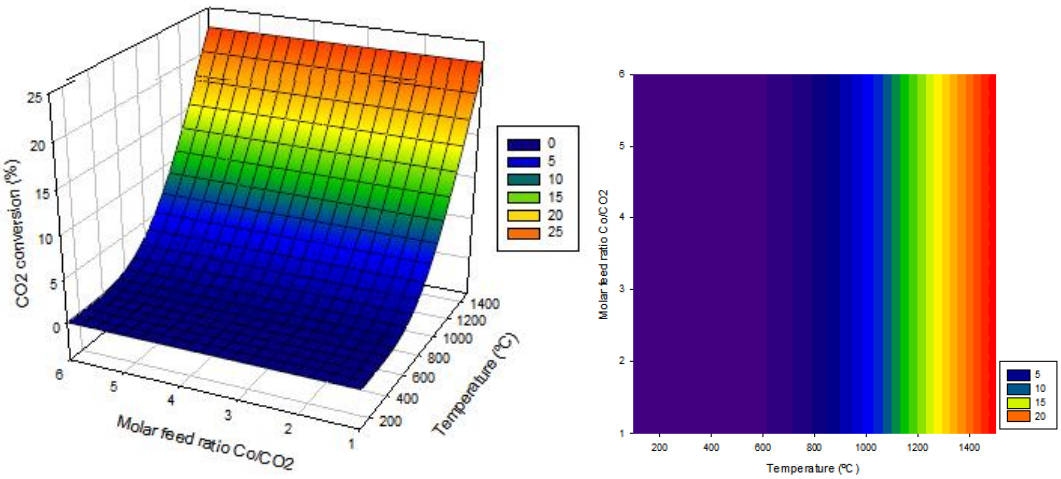

Figure A5- Thermodynamic analysis of the oxidation reaction using CoO.

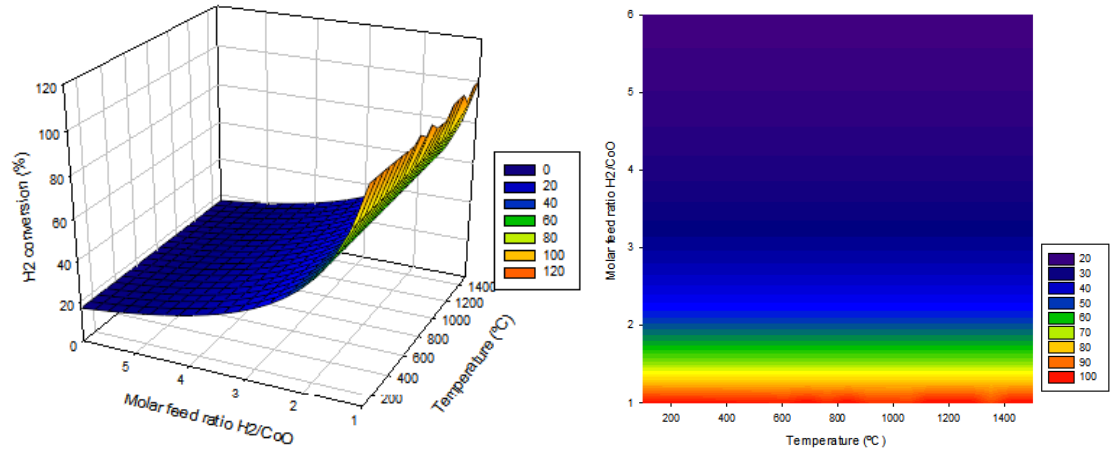

Figure A6- Thermodynamic analysis of the reduction reaction using CoO.

It is observed that even though the reduction reaction presents a H_2 conversion of 100%, the oxidation reaction takes place at very high temperature (1400ºC) for a lower conversion than that found with magnetite (about 25%).

Figures A7 and A8 present the analysis for tin oxide. From the figures it was possible to observe that only the increase in temperature affects the increase in the conversion of CO_2 and H_2, respectively.

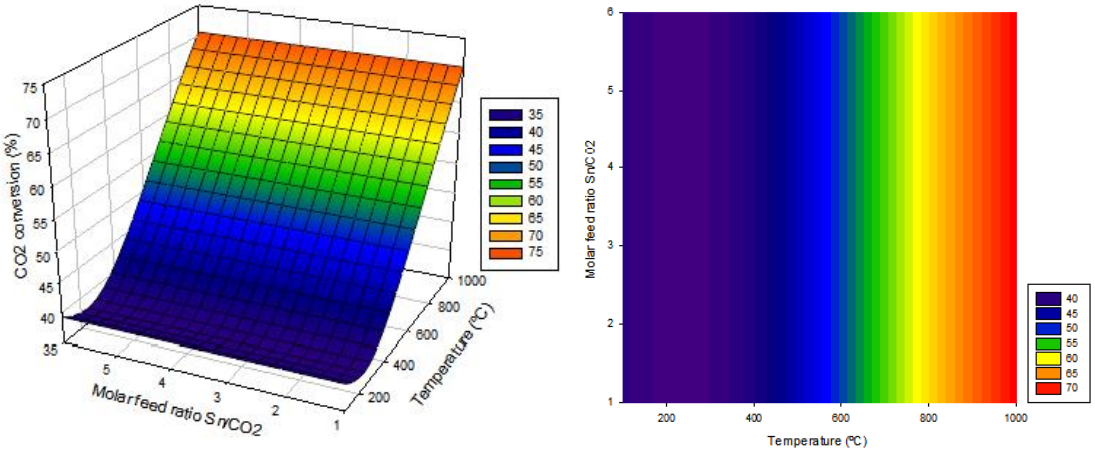

Figure A7- Thermodynamic analysis of the oxidation reaction using SnO.

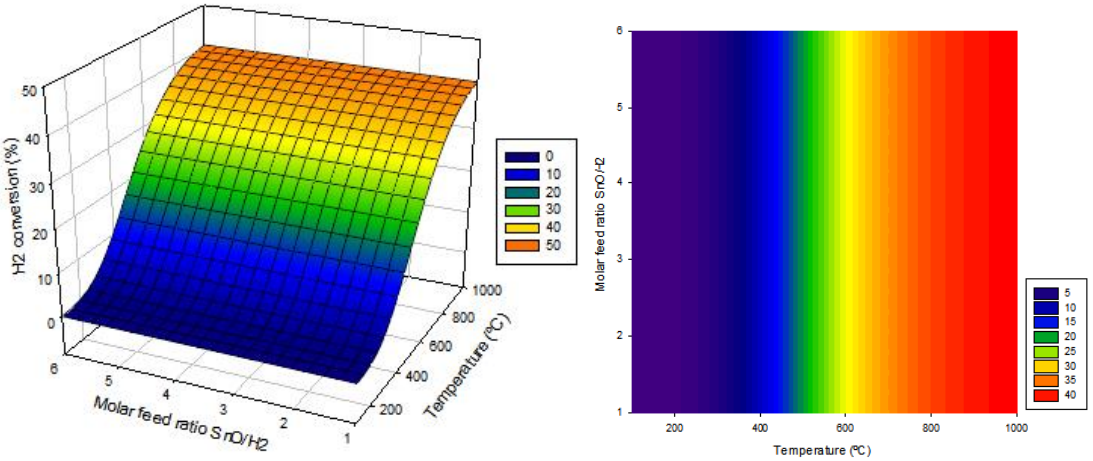

Figure A8- Thermodynamic analysis of the reduction reaction using SnO.

Although, mathematically, tin oxide showed good conversion values (70% CO_2 conversion and 40% H_2 conversion), the correspondent temperature exceeds the melting point of tin, and the molten metal could cause physical damage to the reactor, causing a series of operational problems.

For the analysis of zinc oxide (Figures A9 and A10), it is noted that the oxidation reaction occurs at lower temperatures compared to the other analyzes presenting a conversion

of 100% of CO_2. However, the zinc oxide does not show such promising results for the reduction reaction, requiring a high temperature (1000°C) for low H_2 conversion. It is noteworthy that at high temperatures (800ºC) zinc boils.

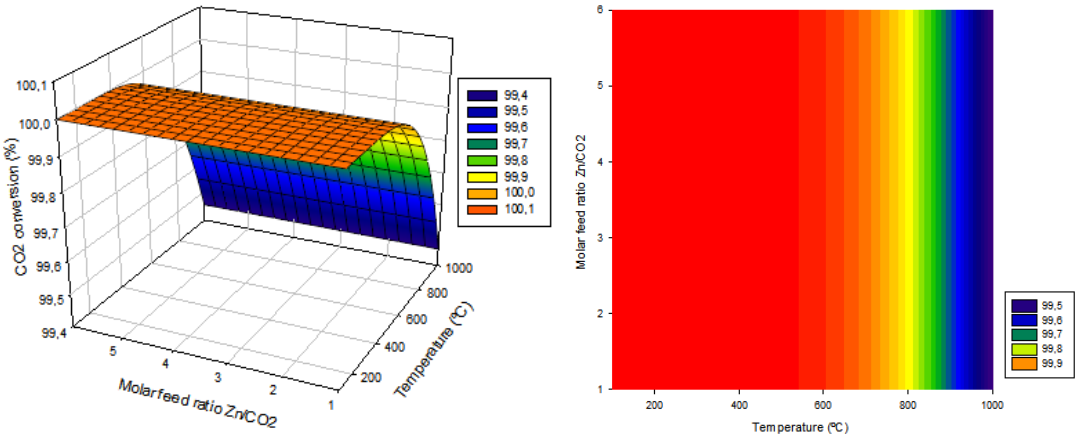

Figure A9- Thermodynamic analysis of the oxidation reaction using ZnO.

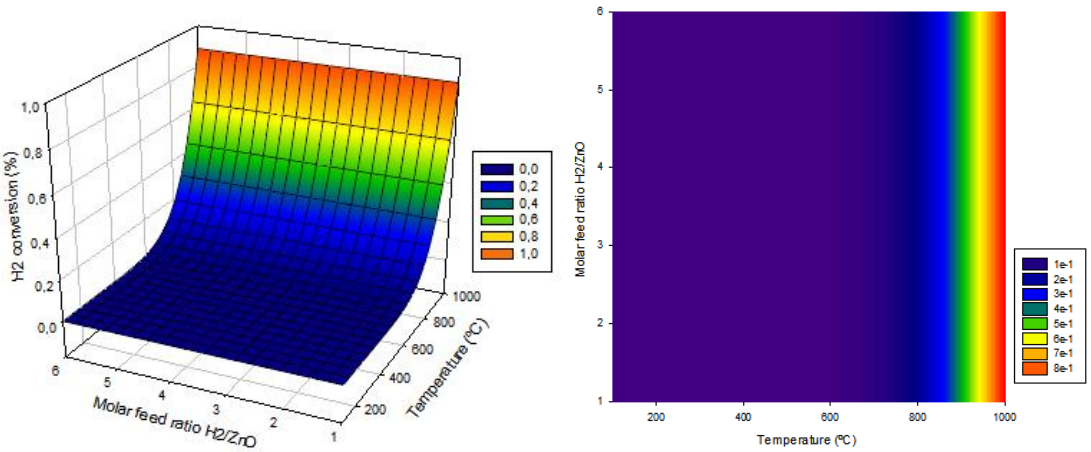

Figure A10- Thermodynamic analysis of the reduction reaction using ZnO.

Figures A11 and A12 present the thermodynamic analysis for the copper oxide. Note that for the oxidation reaction, the CO_2 conversion is insignificant.

Even with a 100% conversion of H_2 for the reduction reaction for the H_2/Cu_2O molar ratio equal to 1, the use of the oxide becomes unfeasible due to the low CO_2 conversion as shown in Figure A11.

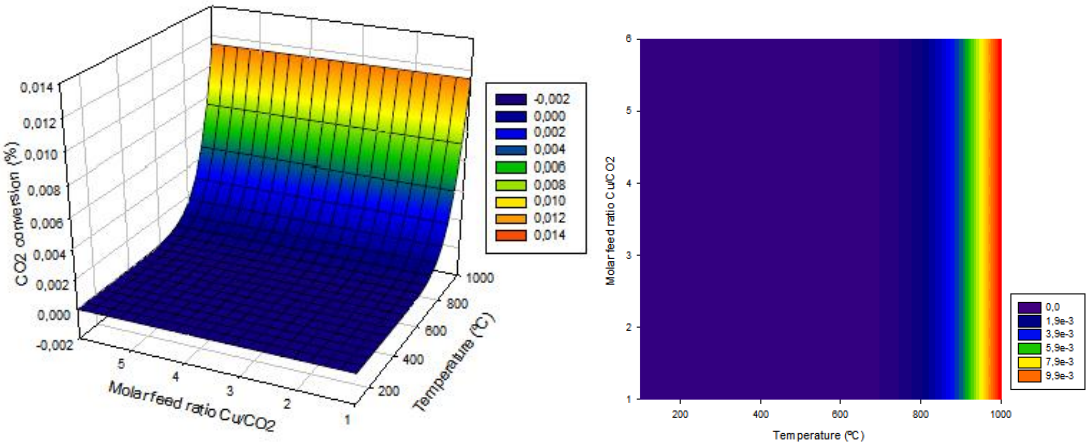

Figure A11- Thermodynamic analysis of the oxidation reaction using Cu_2O.

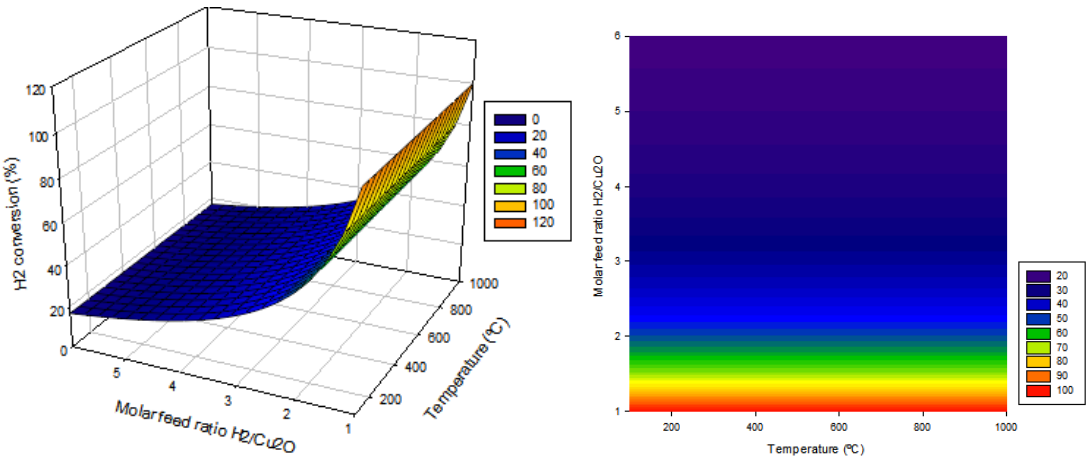

Figure A12- Thermodynamic analysis of the reduction reaction using Cu_2O.

Figures A13 and A14 show the analysis for the manganese oxide. It is observed that although the reduction reaction yields a H_2 conversion of 100%, the oxidation reaction, even increasing the temperature, the CO_2 molar conversion (%) is very low, making its use in RWGS-CL unfeasible.

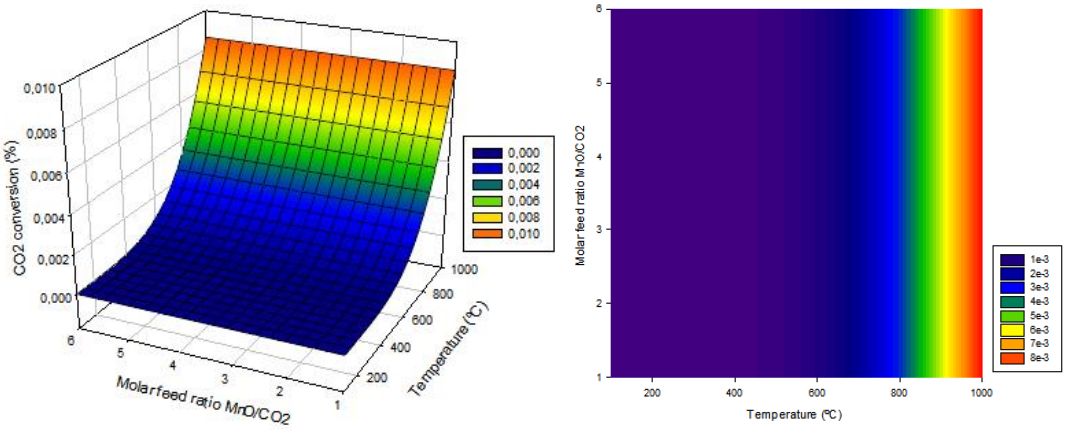

Figure A13- Thermodynamic analysis of the oxidation reaction using Mn_3O_4.

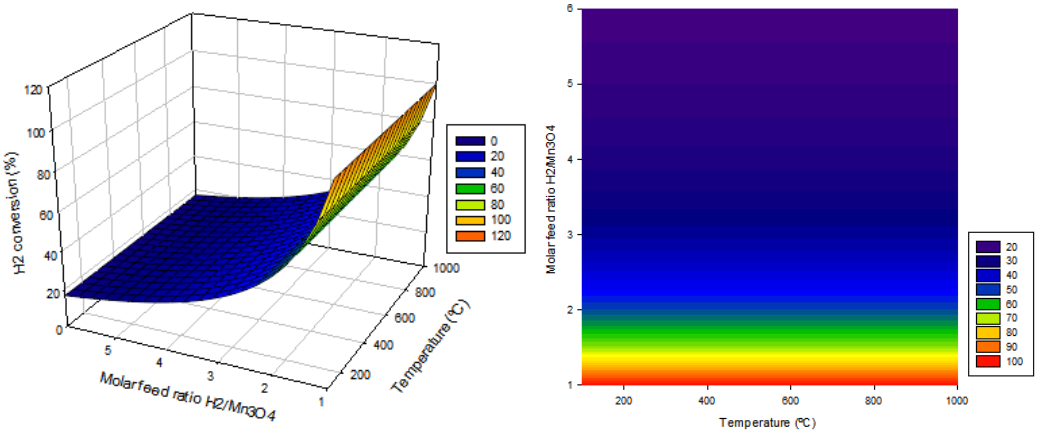

Figure A14- Thermodynamic analysis of the reduction reaction using Mn_3O_4.

Figure A15 presents the analysis for cerium oxide. It is noticed that the molar feed ratio does not influence the CO_2 conversion (%). It is also observed that the greatest CO_2 conversion occurs at temperatures from 200ºC to 700ºC. It is noteworthy that at high temperatures (800ºC) zinc melts.

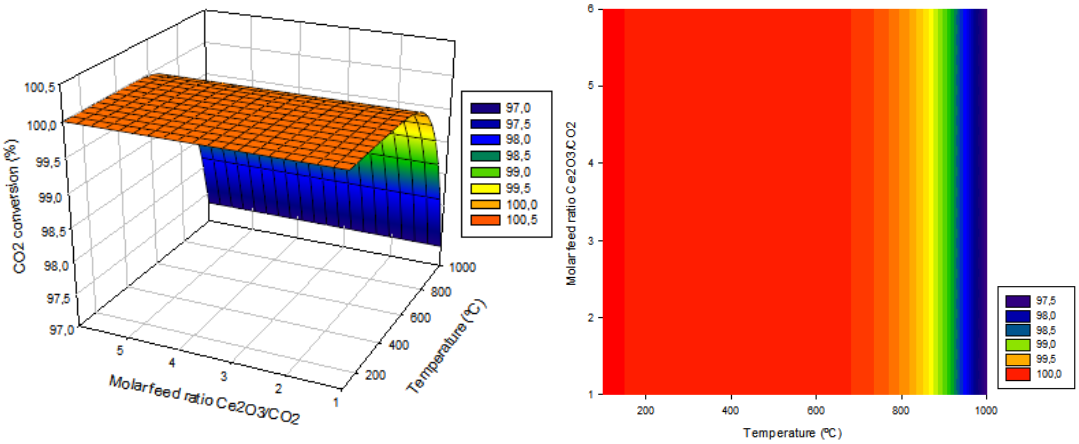

Figure A15- Thermodynamic analysis of the oxidation reaction using CeO_2.

Figure A16 shows that there is no influence of temperature and molar feed ratio on the H_2 conversion. It is also possible to observe that the conversion of H_2 is minimal, therefore cerium oxide (CeO_2) is not a good choice as oxygen-carrying material for RWGS-CL.

Thus, among the evaluated metal oxides, magnetite is the best material for the oxidation and reduction reactions, due to its conversions of CO_2 and H_2, which is corroborated by Wenzel (2018).

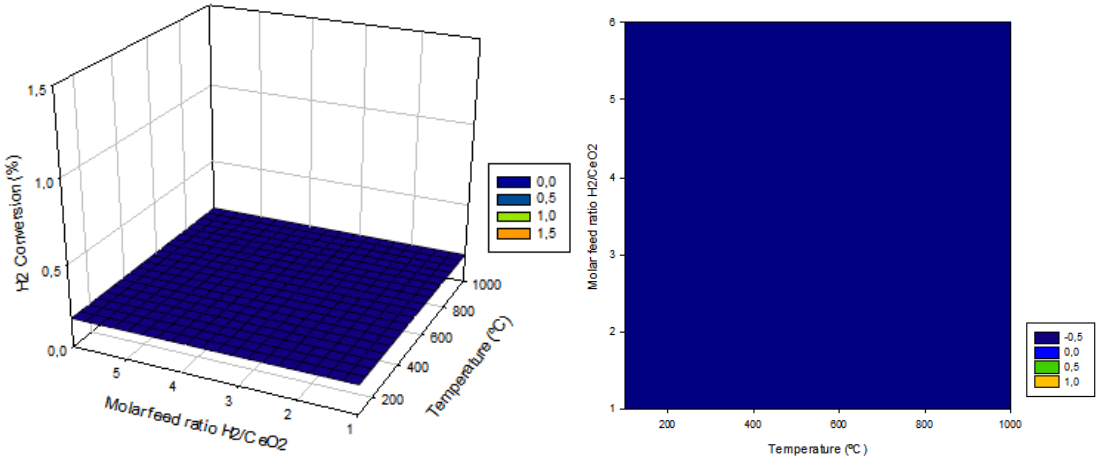

Figure A16- Thermodynamic analysis of the reduction reaction using CeO_2.